THE FRACTURE TOUGHNESS OF ULTRAFINE WC-Co ALLOYS

NATASHA SACKS

MAY 1999

Submitted to the Faculty of Engineering of the University of Cape Town in fulfilment of the requirements for the degree of Master of Science in Materials Engineering.

Department of Materials Engineering
University of Cape Town
Private Bag, Rondebosch, 7700, South Africa

ACKNOWLEDGEMENTS

My supervisor, Professor Colin Allen: Thank you for having been such a great source of encouragement from the very beginning. You always believe that I am able to succeed beyond my own expectations and I will always appreciate that immensely.

Mr. Ian Northrop: Thanks Ian for contributing so significantly to my project, not only by keeping track of all the specimens, but also for your valuable knowledge of tungsten carbide. Thanks for all your support and for making me feel like a real scientist in powder metallurgy.

Thanks to Professor Sylvana Luyckx for providing helpful bits of information and always being willing to clarify ideas on tungsten carbide.

A great THANK-YOU to the above-mentioned three people for providing so many exciting opportunities for me to explore the field of powder metallurgy, both locally and internationally.

An enormous Thank-you to Michael Logan and Ian Matheson from the Boart Longyear Research Centre in Shannon for helping to obtain data for the Terra Tek toughness testing.

I would like to thank the staff of Boart Longyear Research Centre in South Africa for providing the carbide specimen used for this work, for the use of their testing equipment and for giving me a scholarship.

Miranda from the Electron Microscope Unit at UCT – THANK-YOU for your time and assistance!!!

Julie Henry – thank-you VERY much for organising all my money matters and for helping with the tracking down of diamond indentors.

Mira – thanks so much for all your assistance with the microscopes and general laboratory equipment.

James, Bernard and Adriaan – thank-you gentlemen, especially James, for preparing the large amounts of photographs and slides I've used in presentations and in this thesis.

Doreen – thanks for providing a clean work environment.

Thank- you to all the folk in the Materials department who made my years in the department extremely enjoyable and thanks for all the lunch/tea-time chats. Special thanks to Glen, Anthea, Zheng, Vicky, Mira, Julie, Reggie, Nick T., Nick D., Ian, Lungi, Machio, Candy and Rob.

Janet – Thanks for letting me "hog" the computer to complete my write-up. I appreciated it!

Sharon and Lori – my flatmates. You two have been a wonderful source of friendship, encouragement and laughter after long days at the office. I appreciate you both immensely!!

Thanks to all my family and friends for prayers and support and steady supply of laughter throughout the great and the not so great times experienced throughout this work, especially my mom - Nora, 'Matladi, Deb, Leonie, Anna, Michelle, DJ, Belinda, Eloise, Jenny, Celia & Co. and Luke & Co.

Above all, my gratitude goes to my Lord and Saviour Jesus Christ and God. Thank-you for blessing my Masters work exceptionally beyond my expectations. I hope and pray that my work honours and glorifies You.

Auf Wiedersehen Kaapstadt!

ABSTRACT

This thesis examines the fracture toughness behaviour of a series of cemented carbides having carbide grain sizes between 0.35μm and 4μm, cobalt contents ranging from 6 to 15wt%, and vanadium carbide contents from 0 to 0.8wt%. A series of twenty-four ultrafine WC-Co alloys were sintered from powders produced through three different production routes, namely, the spray conversion process and two variations of the conventional powder production methods. A further twelve WC-Co alloys with three different carbide grain size distributions were produced through conventional powder metallurgy processes.

Two different fracture toughness test methods have been used to determine the toughness measurements, namely, the Palmqvist[1] Indentation test and the Short Rod[2] test. A Terra Tek Fractometer machine was used to automatically determine the Short Rod toughness values. The Palmqvist[1] testing was carried out on a Vickers hardness machine using indenting loads of 20, 30 and 50kg. The Palmqvist[1] crack lengths were measured by summing the individual crack lengths emanating from the corners of the hardness indentation. These crack lengths were used in a formula developed by Shetty *et al*[3], to calculate the Palmqvist[1] fracture toughness. The influence of annealing at 800°C and 900°C on the Palmqvist[1] crack lengths has also been assessed. Microstructural parameters have been determined using ASTM procedures and microscopy techniques and the influence of these parameters on the fracture toughness has also been assessed.

The results show that the data obtained from the two different fracture toughness test methods are comparable. However, the Short Rod[2] values display very high scatter in values measured for each grade. No significant difference in mechanical and microstructure properties is observed amongst the ultrafine alloys produced from the three different powder routes. The toughness of these ultrafine alloys varies between 8 to 12MNm$^{-3/2}$ over a hardness range of 1500 to 2200 Vickers. This produces a good combination of excellent hardness coupled with moderate toughness. A linear relationship between hardness and toughness is found for all grades, provided the tungsten carbide grain size is kept constant. The rate of increase in toughness with decreasing hardness is found to be higher the coarser the carbide grain size distribution becomes. The gap between low and high toughness at a given hardness is significantly greater at lower hardness values than at higher values of hardness. The high toughness of the coarse grades is attributed to the large binder mean free paths and the large carbide grains. The moderate toughness observed in the ultrafine alloys is attributed to the small binder mean free path values and the influence of the vanadium carbide.

TABLE OF CONTENTS

CHAPTER 3

CHAPTER 4

CHAPTER 5

Chapter 1

GENERAL INTRODUCTION

1.1 INTRODUCTION

Cemented carbides are very hard, wear resisting materials produced by various methods of powder metallurgy. The microstructure can be defined as being a combination of hard, brittle carbide grains cemented in tough, energy absorbing binder material[4]. Binders are normally produced from the metals cobalt, nickel and chromium and range from 3 to 25wt%. Cobalt is used more often due to its good wetting of tungsten carbide in the solid state and its adequate mechanical properties.

The amount of cobalt may vary from as little as 3 to 13wt% for grades used as cutting tools and up to 30wt% for wear parts. The average size of the tungsten carbide particles varies from less than 1μm to 5μm for machining grades and up to 10μm or more for wear parts. The materials' unique combination of high hardness and moderate toughness has made it indispensable in applications such as metal cutting, rock drilling and in fabricating parts that require a high degree of wear resistance[5-8].

Since the hard metal is used in applications that are commonly subjected to many combinations of stress state and environment, a high resistance to plastic deformation in a predominately compressive mode at both room and high temperature is essential in addition to resistance to the propagation of cracks either from mechanical or thermal fatigue. In many instances, the service capability of these cemented carbides is limited by their toughness, which can be defined as the measure of a material's ability to resist fracture.

In order to improve the mechanical properties of hard metals there has been and is currently, an increasing tendency in the hard metal industry to reduce the tungsten

carbide grain size in order to exploit the advantages that a finer grain size offers, such as increased toughness, strength, rigidity, hardness[9] and wear resistance[10]. Nanoscale powders have recently been produced which have a powder grain size between 20-50nm and sintered grain sizes of less than 0.5μm. These materials are termed ultrafine grained hard metals.

There are various ways for producing nanometer grain size powders, for example by the spray conversion process[11] or by long time ball milling[12]. Although all the processes produce nanograins in the range of 20-50nm, powders produced by different processes behave differently during sintering[13]. The possible reason is that the various manufacturing processes introduce distinct internal stresses, defects and alloy distributions in the powders, which in turn may effect their sintering kinetics and even the mechanical properties of the finished products.

It has been found[14] that the sintered tungsten carbide grain size depends on the initial powder grain-size and since grain growth occurs during the sintering process much effort has been directed into limiting grain growth during sintering thus promoting the production of ultrafine alloys. Successful grain refinement has been achieved by the addition of vanadium carbide during milling and by attempts at keeping the sintering temperature as low as possible[6].

Preliminary studies have shown that these ultrafine products exhibit a wear resistance 2-6 times higher than conventional materials, and are continuing to find increasing usage in areas such as wood machining, metal machining, printed circuit board drills and dental work[10]. As a result various manufacturers are competing to produce nanostructured powders which are necessary to achieve ultrafine hard metals which have superior properties.

1.2 RESEARCH OBJECTIVES

- The main objective of this research was to evaluate and compare the fracture toughness properties of a series of ultrafine tungsten carbide hard metals manufactured via different powder metallurgy processing routes namely, the spray conversion process and conventional ball milling.

- A second objective was to compare the results obtained using two different fracture toughness tests that are commonly used in the hard metal industry namely, the Palmqvist[1] Indentation method and the ASTM Short Rod method[2]. There is a need to establish whether the data from the Palmqvist[1] test and that obtained from the Short Rod[2] test are interchangeable.

- A third objective was to relate the effect of composition and morphology to the fracture toughness of hard metals and to compare the ultrafine alloys to coarser grained cemented carbides.

Chapter 2

LITERATURE REVIEW

Tungsten carbide was discovered more than 100 years ago by Henri Moissan[15] in 1896. He first melted buttons of tungsten together with a great excess of tungstic oxide and got a bright and very hard metal with a density of 18.7g/cm^3. He then heated a mixture of tungstic acid and sugar coal and got a melted tungsten button assaying 99.87%W, without any carbon. Later by melting the buttons with excess carbon he prepared the compound W_2C, a gray, very hard material, with a carbon content of 3.05 to 3.22% and a density of 16.06g/cm^3.

By 1927, the Krupp Company commercially produced "WIDIA-N" (WC-6%Co), the first hard metal tool, where the name meant "diamond-like". This hard metal was based on a patent developed by Karl Schroter[16]. The tools were initially developed in response to demands for a material that was sufficiently wear resistant for wire drawing dies. It was soon discovered that the new material could be used for machining and that cemented carbides have higher hardness and wear resistance, including hardness at elevated temperatures, than high-speed tool steels. One of the most important forms in which cemented carbides were used was as tool bits, which were brazed or clamped into a steel holder. These types of tools are still being extensively used today and hard metals are now firmly established as important materials in applications ranging from metal machining, mining and civil engineering, to a wide range of metal and wear resistant applications. Their great technical and industrial importance has led to numerous experimental investigations aimed at developing the best hard material for a particular application.

2.1 HARD METAL CONSTITUENTS

The cemented carbides investigated in this work are comprised of tungsten (W), carbon (C), cobalt (Co) and vanadium (V). Tungsten and carbon form the carbide, WC that constitutes approximately 80-95% of the phases present in the sintered hard metal. Cobalt is added to cement the carbides together and provide ductility to the final component and vanadium is used as a grain refiner during sintering. A brief review is given of the different constituents and their properties.

2.1.1 TUNGSTEN CARBIDE

Tungsten exists in nature as wolframite, a complex iron-manganese-tungsten oxide, and scheelite, a calcium tungsten oxide. It has excellent resistance to attack by most of the common acids even at high temperatures. The best known use of tungsten is in combination with carbon as sintered carbide for cutting tools, where excellent abrasion resistance is needed.

Tungsten forms two carbides, W_2C and WC, but only the latter is used in the manufacture of cemented carbides. Tungsten monocarbide, WC has a simple hexagonal structure, with lattice parameters a = 0.291nm and c = 0.284nm. The ratio of c/a = 0.976[17]. The crystal structure is shown in figure 2.1. Carbon atoms are either located at 1/3, 2/3, or 1/2 all at 2/3, 1/3, 1/2, void positions.

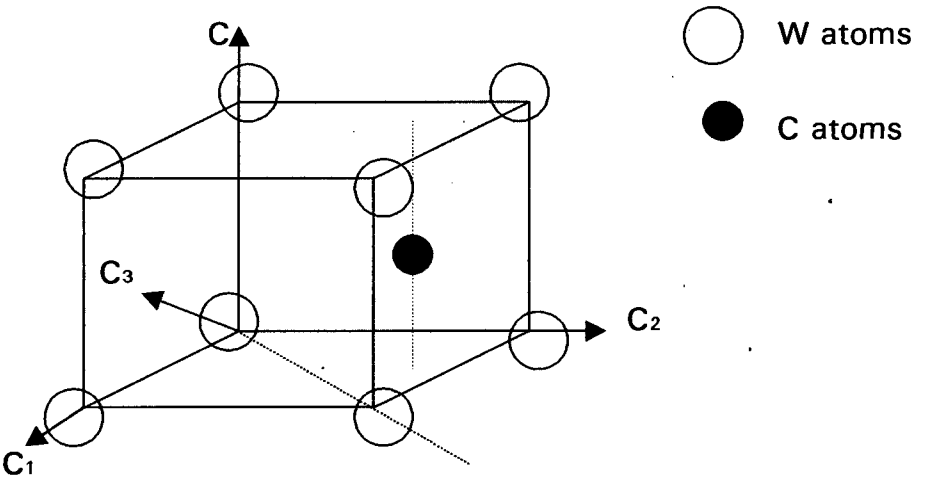

Figure 2.1 *Crystal structure of tungsten carbide. (After reference 18)*

2.1.2 COBALT

Although other materials have been used as the binder for tungsten carbide hard metals since 1914, cobalt has dominated this market as the ultimate binder[19]. This is due to cobalt's good wetting of tungsten carbide in the solid state and its adequate mechanical properties.

The markets for cobalt have been defined as follows[19]:

- superalloys (Ni and Co-based) 26%
- hard facing and other alloys 9%
- hard metals 10.5%
- magnets 11%
- ceramics/glass/pigments 10.5%
- chemicals – catalysts/driers soaps 33%

There are two allotropic forms of cobalt namely, the hexagonal close packed form that is stable at temperatures below 417°C and an face centered cube form that is stable at higher temperatures, up to the melting point (1495°C)[17,20]. The most accurate lattice parameters of cobalt are the following:

hcp: a = 2.5071A and c = 4.0686A with c/a = 1.623;
fcc: a = 3.5441A.

The cobalt present in sintered tungsten carbide-cobalt is mainly the metastable face centered cubic phase but can also contain lamellae of hexagonal cobalt[21,22]. The free energy change associated with the fcc⇔hcp transformation is very low and is usually suppressed during cooling by mechanical constraints developing as a result of differential thermal contraction. Other factors which determine the transformation are the binder mean free path (i.e. the distance between two carbide particles) and the amount of tungsten carbide dissolved in the binder.

The amount of tungsten in solution in the binder varies with the total carbon content of the hard metal. At high total carbon contents, the tungsten content is low and vice versa[21]. At room temperature, the cobalt binder contains about 2-10wt% tungsten carbide dissolved in solid solution. The tungsten atoms substitute

for cobalt atoms while the carbon atoms fill the octahedral interstices in the cobalt matrix[17,20]. Cobalt does not dissolve in the tungsten carbide phase.

2.1.3 VANADIUM

Vanadium is used as a grain growth inhibitor during the sintering process of cemented carbides. The most effective grain growth inhibitors have been found to be VC, Cr_3C_2 NbC and TaC, while the restricting effect is controlled by the M_xC_y/Co ratio. For example the optimal VC content is near 5% of the binder content[23]. The incorporation of different carbides such as VC and Cr_3C_2 in the tungsten carbide grades has proven to be useful in improving the quality of tools employed for specific applications and inhibiting and controlling the grain growth[13,24-26].

Grain growth inhibitors such as VC are more effective during sintering of micron-sized powder compared to sub-micron and nano-grained powders[27]. The reason for this is that vanadium carbide is most active as a grain growth inhibitor at 1300°C where sintering of micron sized powder specimen is carried out. The sintering of submicron grades is achieved at lower temperatures where vanadium carbide is not so effective as a grain growth inhibitor.

Sintering studies by Egami *et al.*[28], suggest that one mechanism of grain growth inhibition of tungsten carbide by vanadium is the decrease of the motive force of the precipitation of tungsten carbide from cobalt by the prior precipitation of vanadium compounds at the WC/Co interface during cooling. The difference in solubility of vanadium in cobalt at high temperature and at room temperature is much larger than that of tungsten in cobalt. As the solubility limit is determined by the solubility product of tungsten, vanadium and carbon, after the vanadium compounds precipitate, the supersaturating of tungsten in cobalt decreases. Moreover, as the vanadium is precipitated as (V, W)C, the content of tungsten in cobalt decreases rapidly. These particles are so small that they do not reduce the mechanical properties of sub-micron hard metals. However when the amount and size of (V, W)C increases the transverse rupture strength especially declines in spite of a sound microstructure.

2.1.4 CARBON

One of the important factors in the sintering of cemented carbides is the carbon balance. Correct control of the carbon is required in order to avoid the formation of the eta phase when there is a carbon deficiency, while if there is an excess of carbon, free carbon can form[29]. It has been stated that the best combination of mechanical properties can be achieved at the lowest possible carbon balance close to the appearance of the eta phase i.e., the highest fracture toughness for a given hardness[30].

It is necessary therefore to control the carbon content of the system in order to allow the composition to fall inside the two-phase region in which Co(W,C) phase is in equilibrium with WC as shown in the C-Co-W phase diagram (figure 2.2). Two phases, namely tungsten carbide and a cobalt rich solid solution appear in the sintered structure if the carbon composition corresponds very nearly to the theoretical carbon content of tungsten carbide, which is 6.12%. Small deviations from the ideal carbon content will result in the appearance of either free carbon or the double carbide, i.e. eta phase[17,20,32-34]. The carbon content must be kept within 0.05wt% of the stoichiometric composition.

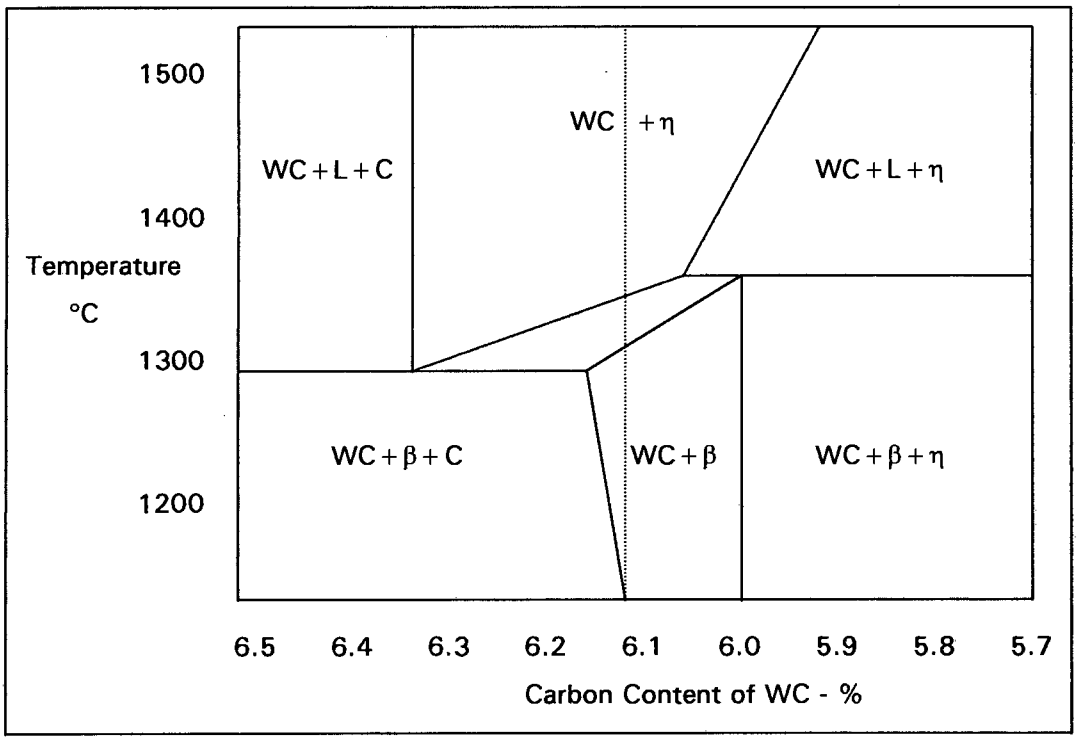

Figure 2.2 *W-C-Co phase diagram. (After reference 32)*

During sintering studies, Gurland[32] determined that the eta phase will form during sintering and will be present at room temperature if the tungsten carbide contains less than 6.00% carbon. If the carbon content of tungsten carbide is between 6.00 and 6.06%C, the eta phase will occur in the equilibrium structure within a narrow temperature range and can be maintained at room temperature only by rapid cooling.

Eta phase is formed according to the reaction:[33]

$$3WC + 3Co(liq.) \Rightarrow Co_3W_3C + 2C$$

The tungsten and carbon taking part in the reaction are the tungsten and carbon in solid solution in the cobalt. In the course of the reaction, tungsten and carbon are removed from the solution, hence the carbide grains adjacent to the growing eta phase partially dissolve[34]. This leads to embrittlement of the structure by the replacement of the binder with an eta-phase skeleton. The hardness of the eta-carbide is intermediate between that of the tungsten carbide and the binder. Eta increases the hardness of the alloy only if it is present in small amounts and is well dispersed. This double carbide brings about a drastic reduction of transverse rupture strength.

An excess of carbon results in the appearance of graphite clusters, which form weak points in the material. The graphite clusters are small and relatively isolated and are known to moderately decrease the strength and hardness. French and Thomas[35] found that such defects are located in a narrow zone at the surface of the material. According to them, localized excess carbon defects approximate small holes and can result in a strength reduction.

2.2 HARD METAL MANUFACTURE

It has been stated that an ideal process for the manufacture of cemented carbide powders should be versatile, robust, capable, clean, simple and low cost[36]. The most important factors affecting the properties of hard metals in service are the fabrication process and the microstructure generated during manufacture. This means optimization of the material selection, design and manufacturing process for

a particular service application. Hard metals, such as the cemented carbides are more sensitive to the manufacturing process than other materials due to their brittle nature.

When selecting a raw material the most critical considerations are the tungsten carbide grain size and the carbon content. The carbide grain size strongly determines the hardness level that will be present in the final component. The carbon content should be close to stoichiometric, approximately 6.12% for tungsten carbide. This is generally desired in the sintered hard metal components to prevent additional deleterious phases forming such as free carbon and eta phase. Hard metal manufacturers can alter the carbon balance of the original raw materials by additions of graphite or tungsten metal powder during milling, or by controlling the sinter atmosphere in the furnace.

Various techniques have been developed to produce tungsten carbide powders. In 1992, a newly developed spray conversion process (SCP)[12] made it possible to synthesize WC-Co composite powders "in situ" as compared with the traditional method of making tungsten carbide and cobalt powders separately and then blending them together. A short review is now given of the two methods of powder production, followed by a brief explanation of further manufacturing processes such as milling, pressing and sintering.

2.2.1 CONVENTIONAL PRODUCTION OF ULTRAFINE WC POWDER

Tungsten carbide powder manufacture is based on the production of tungsten powder by hydrogen reduction of tungsten oxide and subsequent carburisation. Alternatively, direct carburisation of tungsten oxides can also be carried out[21]. The starting materials in both cases are either tungsten acid or tungsten blue and yellow oxides originating from ammonium paratungstate. The aim in powder production is to produce a pure, uniform, fine and loosely agglomerated powder that can be easily dispersed during W-C powder mixing, WC powder deagglomeration and (WC/Co) powder milling.

Ultrafine tungsten powders obtained by the H_2 reduction of the tungsten oxides have a pseudomorphic (sponge-like) appearance in the oxide raw material. These sponge-like agglomerates form due to the extremely dry reduction conditions prevalent during the powder manufacture. They are made up of extremely fine metal grains of about 20-50nm, held together by strong intergranular forces as well as chemical and physical bonding. The ease with which these agglomerates can be broken down during subsequent deagglomeration varies significantly. If disintegration is more uniform during the deagglomeration process, the particle dispersion will be more uniform during subsequent blending with carbon black. With a lower degree of metal-metal contacts during carburisation, the coarsening of the particles decreases.

The carburization of the ultrafine tungsten carbide powders is carried out at low temperatures, around 1200-1450°C. Low temperatures are chosen in order to restrict severe particle coarsening during the W $\Rightarrow$ WC transition. However, a certain coarsening does occur by a strong decrease in the specific surface areas of the powders. Practical carburisation has indicated that there is a lower particle size range below which finer tungsten carbide powders cannot be produced. This limit lies in the range of 50-150nm. This limit is inherent to the existing conventional processing technique itself and can only be overcome by the establishment of new routes in carbide production.

2.2.2 THE SPRAY CONVERSION PROCESS (SCP)

The SCP has been under development by Nanodyne since 1992[36]. The essential process comprises of three unit operations namely:

- an aqueous solution mixing operation, in which the final composition of the powder is established;
- a spray drying operation, which converts the aqueous precursor solution to an easily fluidized solid solution powder having good flow characteristics;
- a gas/solid reaction operation that converts the solid powder solution to nanostructured WC-Co powder in a high temperature fluid bed reactor.

Figure 2.3 is a schematic detailing the overall process[36].

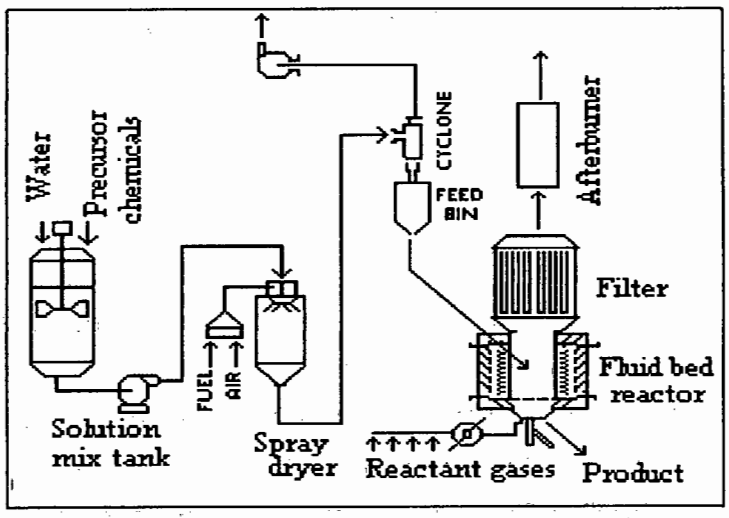

Figure 2.3 *The Spray Conversion Process. (After reference 36)*

The first step, solution mixing leads to the process's versatility in that amorphous solid solutions could be obtained by spray drying aqueous precursor solutions with any Co/W ratio. Precursor solutions can be made from a wide range of constituent raw materials even scrap hard metal. In this step the precursors are aqueous solutions of W-containing and Co-containing compounds that are mixed at an atomic level.

The second step in the process is the spray drying of the precursor solution to form a homogenous powder with an amorphous structure. The primary function of this step is to eliminate water and to maintain the level of mixing that was established in the aqueous solution. This is done to establish powder characteristics that will benefit powder handling and facilitate powder fluidization during the conversion reaction in the third step of the process.

In the third step the precursor powder is converted to a nanograined WC-Co powder. This process is carried out in a fluid bed reactor where the conversion temperature is around 700–900°C in a carburising atmosphere. Suitable atmosphere mixtures that are used include CO/CO_2 and CO/H_2. The inlet gas composition and reaction temperature determines the final phase composition of the powder by fixing the gas phase carbon activity. The entire system is brought to a steady state that is essentially the quasi-equilibrium state at the chosen reaction temperature. Spherical-shell particles of tungsten carbide are produced that have a mean diameter of approximately 70μm. Each shell particle has a sponge-like

structure that is comprised of approximately 20-50nm carbide crystallites embedded in a cobalt matrix.

2.2.3 MILLING

The main aim in hard metal milling is to obtain a homogeneous dispersion of tungsten carbide in the cobalt[37]. A decrease in the tungsten carbide particle size also occurs and this facilitates the sintering process[37-40]. It has been found that it is better to mill the tungsten and cobalt powders together instead of milling each powder separately and then mixing them together[41]. The disadvantage of the latter is that the sintered product has been found to be porous, even after extended sintering times, which leads to depreciation in the mechanical properties of the component[41].

During the course of milling stresses are induced in the tungsten carbide grains[42] and the cobalt phase changes from a predominantly cubic to a hexagonal close packed structure[39]. These strains induced in the carbide phase will lead to an enhanced sintering activity[43]. Carol[44] found that milling time influences the microstructure of the sintered component. If short milling times, i.e., 12 to 24 hours, were employed, cobalt pooling and extensive residual porosity would be present in the sintered structure. Shorter milling times can also result in inhomogeneous mixing which leads to discontinuous grain growth[45]. When milling times are increased, cobalt pooling can be eliminated and the porosity levels are lower. An increase in coercivity (by 700 Oes) and hardness (by 150 Vickers) has also been detected for longer milling times[44].

After milling the powder, a lubricant (e.g. paraffin wax) dissolved in a volatile solvent (e.g. xylol or carbon tetrachloride) is blended into the powder. The main function of the lubricant is to reduce friction between the powder mixture and the surfaces of the tools along which the powder slides during compaction. It also minimizes the tendency to form cracks. Sintering without such a lubricant may result in interlocking, bridging, intermittent voids, irregular shrinkage, variable density or severe distortion[27].

A common practice in the industrial production of cemented carbides is to add minor amounts of carbon (soot) or tungsten powder to the hard metal mixture during milling depending on the final microstructure and composition of the binder to be achieved. Soot additions are also made to compensate for carbon losses that may occur due to oxidation during pre-sintering and sintering. Both the pressing aid and the furnace atmosphere will also influence the carbon content during pre-sintering and sintering. Milling and handling of the material will also have a strong influence due to the presence of oxygen and moisture in the environment and in the milling liquids.

2.2.4 PRESSING

The mixed powders are pressed into shape in a rigid steel or carbide die under pressures of 150-900MPa[27]. Compacting pressures from 50 to 150MPa are usually applied via single or double-acting hydraulic presses. Components may be pressed directly into specified shapes or they may be pressed into a large block and subsequently shaped. During this stage the powder compacts maintain their shape by virtue of cold-welding of the powder grains within the mass. The compacts must be sufficiently strong to withstand ejection from the die and subsequent handling before sintering. The level and uniformity of the as-pressed density determine the final shape and mechanical properties.

2.2.5 PRE-SINTERING

The pre-sintering operation is carried out in hydrogen at a temperature gradually rising from room temperature to 800°C. The hydrogen reduces the amount of adsorbed oxygen and oxides present on the surfaces of the powder particles. During pre-sintering the following occurs:

- volatilization of the lubricant between 200–400°C, causing the lubricant to decompose and evaporate.
- "welding" between particles in the solid state at approximately 800°C.

On cooling the material is sufficiently coherent to allow further shaping and is also less susceptible to damage than in the compacted form.

2.2.6 SINTERING

When a compact from a mixture of tungsten carbide and cobalt powder is heated, a liquid phase is formed by the reaction between the tungsten carbide and the cobalt. Sintering of cemented carbides is therefore referred to as liquid phase sintering. The most crucial aspect of sintering is retaining the ultrafine microstructure of the WC in the consolidated (dense) material.

An interesting characteristic of nanocrystalline cemented carbide powders is that most of the densification during sintering takes place in the solid state[46], compared to that of regular, micron size powder, where little densification occurs in the solid state the majority taking place in the liquid state[28]. However, results of a study by Porat *et al.*[27], showed that nanocrystalline powders made by conventional metal production attain full density at temperatures lower than the liquidus point, while powders made by the SCP[36] had to be sintered in the liquid phase in order to reach full density.

The driving force for sintering of ultrafine grained hard metals is a reduction in the energy system by reducing the area of the surfaces and interfaces of the compact. This occurs by a combination of two process, namely[21]:

- densification during which the gas/solid interface is replaced by a lower-energy solid-solid or solid-liquid interface;
- tungsten carbide grain growth during which the solid-solid or solid-liquid interface areas decrease and low-energy prismatic interfaces form.

Sintering is usually carried out in a vacuum at temperatures between approximately 1350°C (high cobalt compositions) and 1550°C (low cobalt compositions). These temperatures are chosen with reference to the Co-W-C ternary system and the pseudo-eutectic WC-Co diagram in figure 2.4 which is most commonly used in describing the reactions that occur under commercial sintering conditions[47].

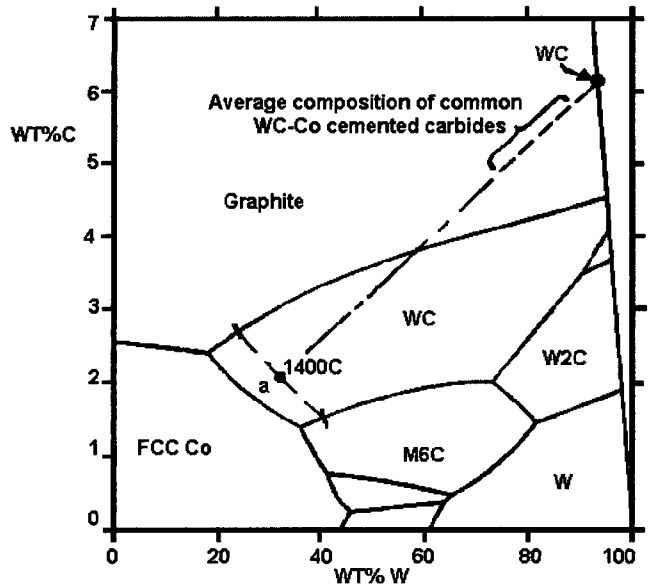

Figure 2.4 *Psuedo-eutectic WC-Co phase diagram (After reference 48)*

According to the calculated phase diagram the equilibrium contents of tungsten and carbon in the liquid are as much as 30wt%W and 2wt%C in a stoichiometric WC-Co alloy at 1400°C. This corresponds to a mole fraction of liquid of about 20% for an alloy containing 10wt%Co. The WC-carbide has a very narrow compositional range at temperatures below 2000°C and does not dissolve cobalt[48].

The result of the sintering process is dependent on the inherent properties of the alloy system, but also to a large extent on the production techniques used. Factors that influence sintering also include:[48,49]

- the carbon content of the powders, which should be sufficient to maintain stoichiometric WC and avoid eta-phase formation;
- the purity of the starting materials, since any oxide particles present are mainly responsible for residual porosity;
- the particle size, distribution and morphology, since these parameters strongly influence the packing density and uniformity of packing in the cold compact;
- the use of grain growth inhibitors which effectively mitigate tungsten carbide particle growth during liquid phase sintering;
- the amount of binder present and the solubility of the carbide in the binder

During sintering, the compact acquires the strength needed to fulfil the intended role as an engineering component. Recrystallization and grain growth may follow,

and the pores tend to become rounded and the total porosity of the whole volume tends to decrease. The rounded shape of the tungsten carbide in the early stages of sintering gives way to a faceted morphology and finally the grains will have the shape of flat trigonal prisms[50].

2.2.7 HOT ISOSTATIC PRESSING (HIP)

Hot isostatic pressing was invented by Saller *et al.*[51] in 1955 and first commercially used as a post-sintering operation for cemented carbides some twelve years later[27]. It involves the application of a high pressure (typically 100-150MPa) by an inert gas medium at temperatures 50°C above the solidus temperature of the binder phase[52]. The treatment results in a reduction in porosity. However HIP does not remove inclusion containing or surface connected pores.

Benefits from HIP include[53]:

- the reclamation of hard metal parts rejected because of porosity;
- improved surface integrity of tools used in metal fabrication processes, e.g. drawing, pressing, rolling. HIP removes sub-surface porosity giving excellent surface finishes;
- the ability to produce low (<4wt%) Co content cemented carbides.

Non-benefits are[53]:

- the coercive force may drop. It has been suggested that this may be due to changes occurs in the binder composition[54];
- if oxygen is present in the furnace, the carbon may oxidize and be removed so that eta phase may form;
- dimensional changes can also occur due to the relaxation of residual stresses, particularly when a component has previously undergone uniaxial hot pressing.

2.3 FRACTURE IN WC-Co ALLOYS

It has been stated that the ability of tungsten carbide grains to accommodate plastic deformation without the occurrence of brittle fracture is probably the single most important parameter underlying the success of WC-based hardmetals[21].

Hong and Gurland[55] concluded that the overall fracture process is similar for all WC-Co materials namely WC/WC boundary debonding and/or tungsten carbide cleavage followed by cobalt rupture. The former is a pre-condition for the latter. The energy required for the propagation of the intergranular or transgranular cleavage cracks in tungsten carbide is believed to be much smaller than that required by the plastic deformation and ductile rupture of the binder. This argument indicates that plastic deformation contributes a major portion of the dissipative work during fracture of the alloys. The different types of fracture paths found in cemented carbides along with general crack propagation will now be reviewed.

2.3.1 FRACTURE PATHS IN CEMENTED CARBIDES

A large amount of fractographic work has been carried out during the past three decades that indicate that four types of fracture paths exist in cemented carbides[55-59]. These are shown schematically in figure 2.5 followed by an explanation of the fracture characteristics of each type.

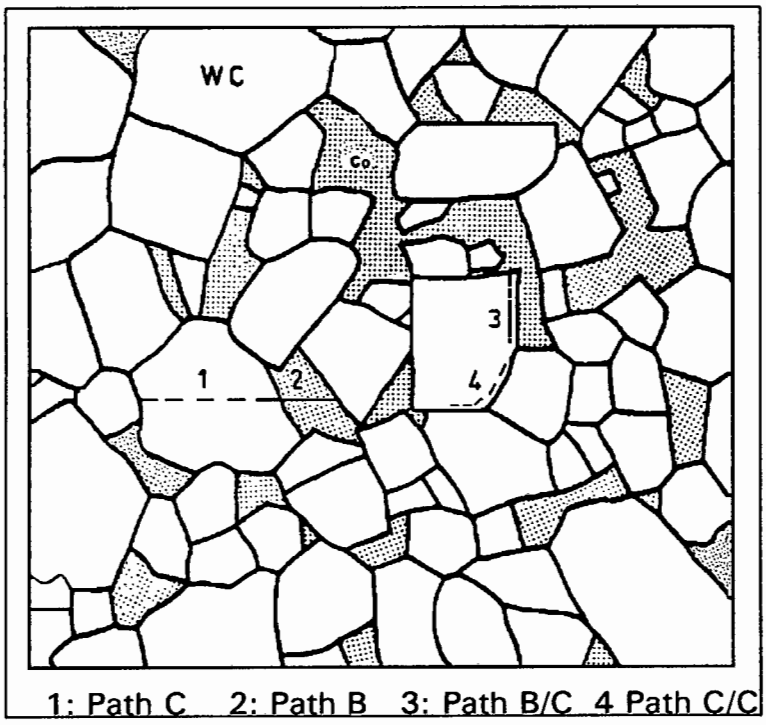

Figure 2.5 *The four types of crack paths found in cemented carbides (After reference 60)*

- **Path B: transgranular fracture though the binder phase**

This type of fracture is characterized by ductile rupture of the cobalt phase. This tearing of the cobalt layer leaves a pattern of dimples or tear ridges on both the fracture surfaces that are equally matched. The size of the dimples decreases as the width of the cobalt layers decrease.

- **Path B/C: Interface fracture along or parallel to the carbide-binder phase boundary**

Some researchers[56] have shown that this path proceeds along the binder/carbide interface whereas others show[55,58] that it proceeds parallel to and very close to the interface. This type is characterized by decoherence of the WC-Co interface boundaries where the WC-Co interface failure, after appreciable deformation, leaves the tungsten carbide and cobalt phase with a pattern of tearing ridges. The fracture surfaces show carbide facets on one face and smooth or fibrous cobalt on the other face. Closely spaced shallow dimples also appear in the cobalt phase and these are much finer than those in path B.

- **Path C/C: Intergranular fracture along the carbide grain boundaries**

This path is characterized by brittle fracture at the WC-WC boundary which leaves a pattern of ruptured cobalt ligaments on the larger tungsten carbide particle face at one fracture surface, and leaves several smooth carbide particles surrounded by a cobalt ridge on the opposite fracture surface.

- **Path C: Transgranular fracture through the carbide crystals/phase**

It is reported that larger tungsten carbide particles fracture transgranularly and smaller carbide particles fracture intergranularly[55]. The broken or debonded particles are surrounded by a coarse ridge of cobalt binder that matches on both fracture surfaces.

Thus a crack propagating through the microstructure can propagate between paths along the binder/carbide interface and paths across the binder regions. It has been shown by evaluations done by Speigler and Fischmeister[61] that the type of crack

path taken in WC-Co alloys is in fact determined by a critical value of the angle of entry of the crack into the binder region. They defined this critical angle as 25 ± 3°.

Figure 2.6 illustrates a typical situation in which the "main crack plane" in the ligament (MCP) is defined by the course of the crack through the carbide phase and it determines the orientation of the stress field that drives the crack through the binder phase region. The angle, φ, between the MCP and the nearest carbide interface will determine whether the crack will go right across the binder (crack path B) or run along a carbide flank (crack path B/C). If this angle is below a certain critical value, $\varphi < \varphi_c$, the crack will adhere to the carbide flank, choosing a path of type B/C. For $\varphi > \varphi_c$, the crack will follow the direction imposed by the MCP, and the path will be of type B[61].

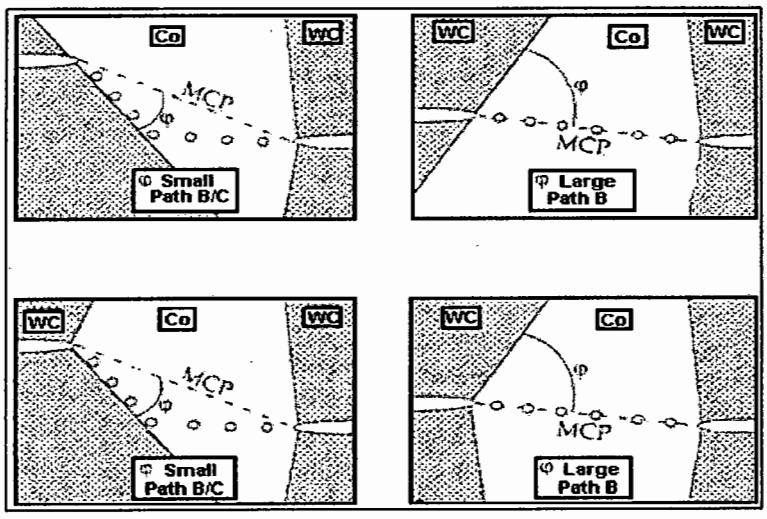

Figure 2.6 *Path of the main crack plane. (After reference 61)*

It has been suggested that the predominant fracture path is through the binder phase which has been corroborated by results from fracture replicas, scanning electron fractography and Auger spectroscopy[62,63]. However, using Auger spectroscopy on uncontaminated fracture surfaces in 6 and 12%Co-WC hard metals, Lea and Roebuck[63] demonstrated that about 50% of the fracture propagates through the WC/WC interfaces, and the latter contain approximately a monolayer of cobalt atoms, which is in good agreement with results of Sharma *et al*[64]. Further fracture observations demonstrated that less than 25% of the fracture would pass through the binder phase.

2.3.2 THE PROCESS ZONE

In multiphase materials such as cemented carbides, the crack tip region, known as the process zone, has been modeled extensively to increase understanding on what occurs in that region. Gille[59] proposed a model for cemented carbides based on models proposed for the process zones in anisotropic single-phase ceramics. He assumed that a large number of carbide cracks are present in front of the crack tip, most of which are stable, while a few are precursors of the main crack and become part of it during crack extension.

According to Evans *et al*[65] a crack in the brittle tungsten carbide phase circumvents the ductile binder regions leaving stretched inclusions across the crack faces. These stretched inclusions, also called ligaments, and the zone behind the crack tip in which such ligaments still bridge the crack is called a multiligament zone[65]. As a result no sharply defined crack tip exists[58]. Thus a multiligament zone is formed which consists of a continuous crack in the brittle phase interrupted by ligaments of ductile phase[56-58,61,65-69].

Almond[57] also observed this zone at the tips of Palmqvist cracks in WC-Co alloys. Also, Sigl *et al*[56] observed this zone at the crack tip of stably grown cracks in single edge notched beam WC-Co specimen in which they found the length of this zone to be of the order of five times the carbide grain size. Others[66] have found its length to be typically of the order of about 100μm. The plastic work involved in stretching and rupturing these ligaments is responsible for a great part of the toughening in these alloys[61]. The typical features in the vicinity of the crack are shown in figure 2.7 below.

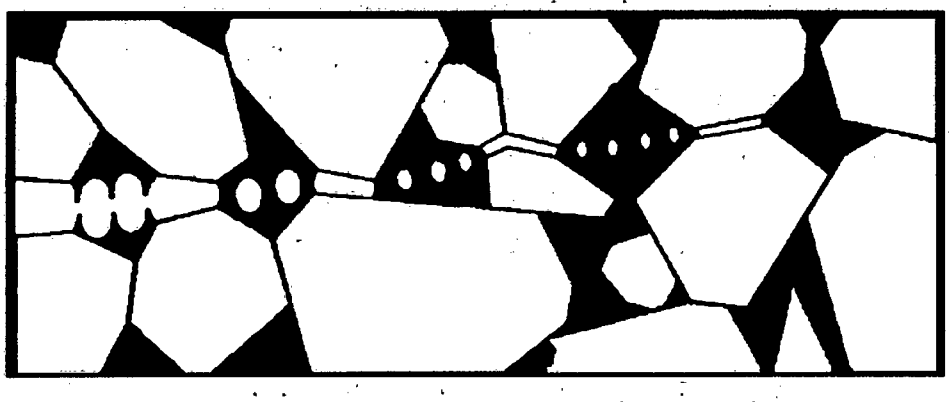

Figure 2.7 *Crack tip region in WC-Co alloy. (After reference 56)*

At the right hand side in figure 2.7, the microstructure is still fully coherent and both phases are deformed elastically. On the left-hand side, both the carbide and the binder phase are fractured. In the multiligament zone between these two regions a three-dimensionally continuous crack path exists in the carbide skeleton while the binder phase which has deformed plastically is still coherent.

Prior to crack formation the plastic deformation of the binder is severely constrained while the surrounding carbide skeleton remains intact. A drastic change of the stress situation in the alloy occurs as the multiligament zone begins to form. As the crack advances, the cobalt ligaments start to deform plastically. Lateral contraction of the ligament is constrained due to plane strain at the crack tip and the surrounding stiff carbide skeleton. In order to comply with binder volume constancy, voids form in the ligaments[56,58,65,69-71]. Finite element calculations[68] and slip line analysis[69] confirm these conclusions. The likelihood of void formation at any given site in the ligament will depend on that site's distance from the nearest carbide grain, and on the triaxiality stress profile introduced by the crack as it enters the ligament, coming from the carbide phase[71]. The formation of these voids is shown schematically in figure 2.8.

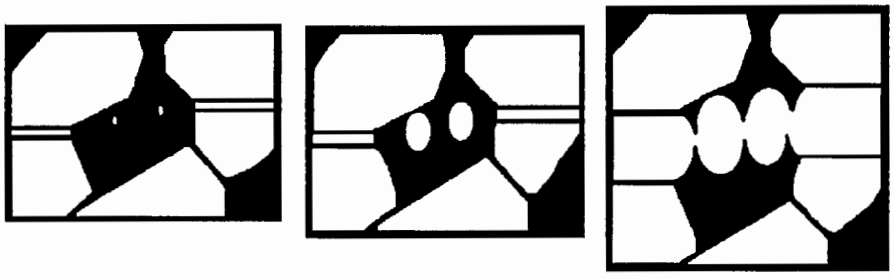

Figure 2.8 *Nucleation, growth and coalescence of voids. (After reference 56)*

Plastic flow is restricted to the ligament bridges between the voids since voids in the bulk of the ligament are bigger than the voids at a carbide-binder interface. All other ligament regions such as those behind the voids are still constrained by the tungsten carbide skeleton and deform in strict compatibility with the elastic deformation of the carbide. These considerations were confirmed by finite element anaylsis[58]. A crack advancing through the voids will lead to coalescence of the voids and rupture of the ligament bridges.

Slesar *et al.*[72] found that the types of ductile rupture in the cobalt ligaments is connected with the mean free path of the binder and the orientation of the

ligaments to the direction of major crack propagation and the operating stress. They observed that at low MFP values, ductile neck ruptures of the binder occurred and with an increase in MFP, neckings were more evident while the more spacious MFP areas were ruptured by dimple mechanisms. These are shown schematically in figure 2.9 below.

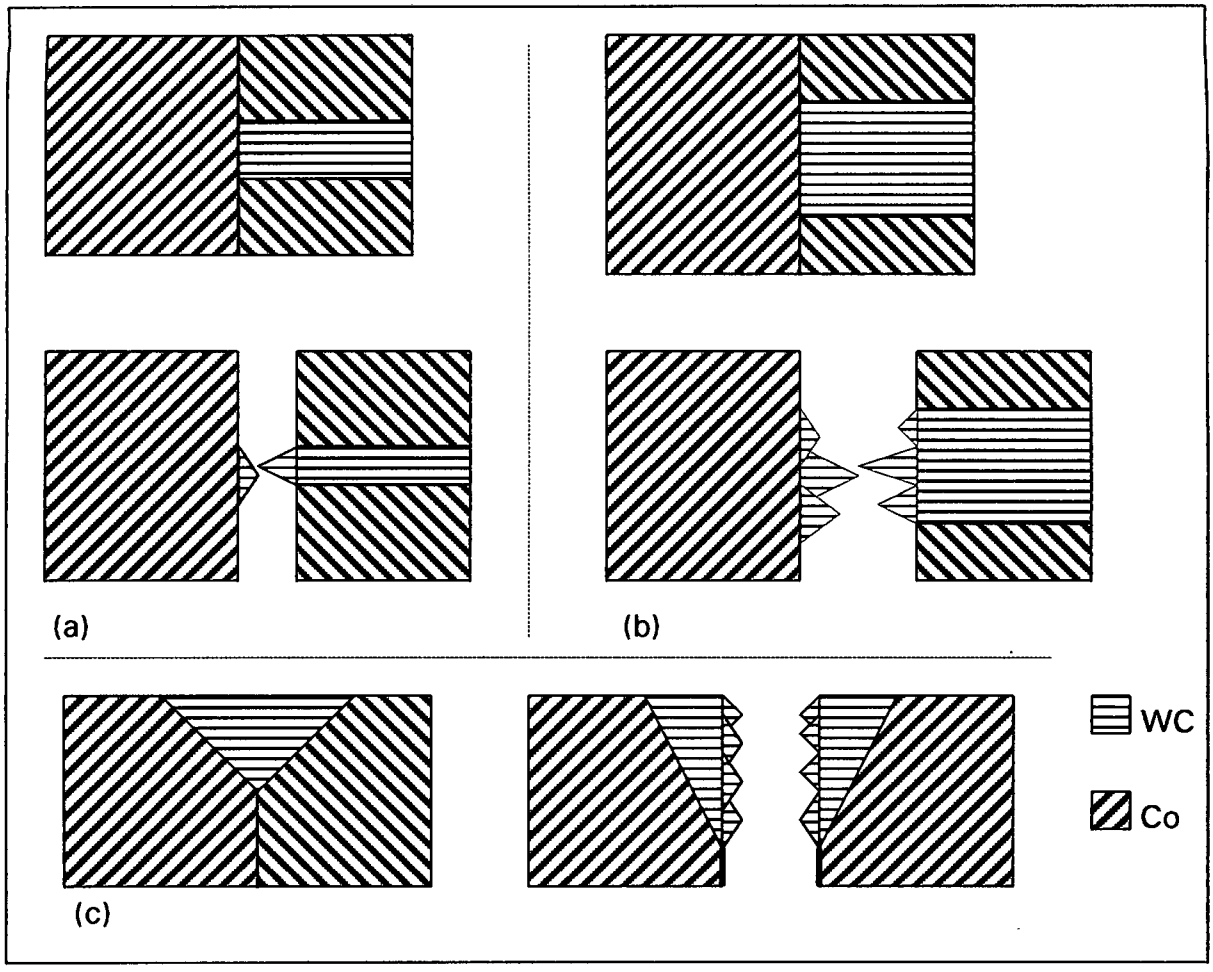

Figure 2.9 *Rupture modes in the binder phase. (After reference 72)*

2.4 TOUGHNESS

Toughness can be defined as the resistance to failure through fracture. Fischmeister and Olsson[73] pointed out that there could be two possible types of toughness, namely, macro-toughness and micro-toughness in tungsten carbide hard metals. The first type is likened to the transverse or torsional rupture of a tool bit or drill shaft. The other applies to the removal of tiny fragments from a cutting edge termed "attrition wear", "edge crumbling" or "microchipping" by tool engineers.

When applied, unqualified, to hard metals, the word "toughness" can have several meanings[74]:

- Plane strain fracture toughness, K_{Ic} ($MNm^{-3/2}$). This is the value obtained from toughness tests carried out on a specimen with a specified crack geometry. The chevron notch and the surface flaw in flexure methods have been proven to be acceptable fracture mechanics methods proposed by the ASTM. The fracture strength of a material, σ, is related to this intrinsic toughness, K_{Ic} and the length of the most severe defect in material tested, a, according equation 2.1 where α is a dimensionless proportionality factor depending on the crack geometry.

$$\sigma = \alpha K_{Ic} a^{-1/2} \quad \text{...(2.1)}$$

- Strain energy release rate, G_{Ic} (Jm^{-2}). This is an alternative expression for toughness, which is usually obtained by converting the plane strain fracture toughness, K_{Ic}, to G_{Ic} by means of equation 2.2.

$$G_{Ic} = K^2/E\,(1-\nu^2) \quad \text{...(2.2)}$$

- Palmqvist toughness, W (Nm^{-1}). This parameter can be evaluated from hardness indentation crack lengths at a single applied load. It can also be estimated from the inverse of the slope of a load against crack length graph. W can be converted to K_{Ic} values using various formulae and an example is given in equation 2.3[3,75,76] where A is a constant and H is the hardness.

$$K_{Ic} = A \sqrt{H} \sqrt{W} \quad \text{...(2.3)}$$

  For conventional metals a good correlation has been claimed between W and K_{Ic}[76].
- Toughness is also widely used to describe the empirical relation between the perceived resistance to dynamic impacts. This is neither standardized nor quantified.

Criticism has been raised concerning the practical significance of fracture toughness in hard metals[77]. This is based on the small variation of K_{Ic} for various hard metal grades and on the fact that K_{Ic} correlates closely with hardness rather than with strength. However, the major advantage of fracture toughness parameters are their well defined mechanical definition and their ability to characterize a material with respect to its resistance to the propagation of existing cracks.

It was stated in section 2.3.7 that the stretching of the cobalt ligaments across a crack face accounted for a major part of the toughening of cemented carbides.

Studies have strongly favored this crack bridging as the dominating toughening mechanism[58,66,67] and various arguments have been presented that deformation occurs only in the regions of metal phase that are intersected by the crack plane[58]. However, Sigl *et al.*[66,67] found that the toughness of cemented carbides was not fully accounted for by the plastic stretching of the crack bridging ligaments.

This conclusion was confirmed by Marshall *et al.*[78] who presented evidence of the contribution to toughness by two different zones of deformation in the hard metals. The first one is associated directly with the stretching and rupture of the bridging ligaments as the crack opening increases behind the crack tip, and the second one was that occurring within an extended zone (i.e. a plastic zone) in the crack tip stress field away from the crack plane. They found that the size of the plastic zone was dependent on strain rate and their results indicated that a significant fraction of the toughness in the cemented carbide material arose from the plastic zone. The plastic zone was found to be smaller for a crack growing unstably than for a stable or stationary crack.

Therefore, unless other contributing toughening mechanisms are enhanced under dynamic conditions more than the plastic zone shielding is decreased, the dynamic fracture toughness may be smaller than the quasi-static value[78].

2.5 INFLUENCE OF MICROSTRUCTURE ON MECHANICAL PROPERTIES

The mechanical properties of sintered carbides are very complex and the influence of the microstructure on these properties is evaluated extensively throughout the hard metal industry. The properties are functions of diverse microstructural parameters of the constituent phases including contiguity[79,80], porosity[81,82], oxidation[83-85], the composition (amount of tungsten and carbon in solid solution) of the cobalt regions[14,86-90] and the size distribution of the phases[14,32,91-98].

2.5.1 COBALT

Cemented carbides for technical applications contain from 5 to 25 wt% Co and its effect on properties has been extensively studied. Hardness decreases with increasing cobalt content, and the compressive strength reaches a maximum at 5wt% and then drops sharply when the cobalt content is increased[99,100]. The transverse rupture strength improves with increasing cobalt content up to a maximum at approximately 20±5wt%Co[32,79,99-104]. The maximum strength composition depends on variables such as the tungsten carbide grain size[79,101,104]. According to Suzuki *et al.*[86,105] the high ductility of the cobalt phase, which contains less tungsten in solid solution, results in lower strength in coarse-grained alloys and greater toughness in fine-grained alloys. Figure 2.10 shows the general trend of these properties for a tungsten carbide particle size of approximately 2μm.

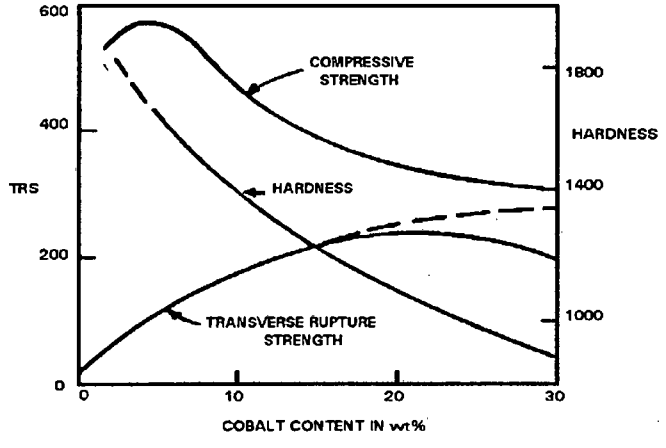

Figure 2.10 *Effect of cobalt content on strength. (After reference 14)*

2.5.2 MEAN FREE PATH OF THE BINDER (MFP)

The mean free path is a measure of the thickness of the cobalt layers and depends on both the cobalt content and the tungsten carbide particle size. Information on the state of the cobalt binder can be obtained from the magnetic coercive force. The coercive force is a measure of the saturation magnetization of the cobalt. It is sensitive to the MFP due to residual lattice strains and it is also very sensitive to the binder composition since saturation is limited by the electron-to-atom ratio. An increase in coercivity implies that smaller values of MFP should exist[106]. A slight decrease in coercivity with increasing cobalt content indicates that the MFP in the

cobalt phase increases slightly with cobalt content, which would lead to an expected increase in toughness with increasing cobalt[106].

The primary variable controlling the fracture toughness is the thickness of the binder phase layers, which has been shown by many researchers[57,91-93,101,107-113]. It has been shown by Gurland[57] that above a critical value of the MFP, the strength follows a dispersion-hardening mechanism[109] and is proportional to the volume fraction of tungsten carbide, but inversely proportional to the tungsten carbide particle size. Below this critical value, a Griffith type[107] relation is followed and strength is controlled by the ease of crack propagation. The compressive strength decreases with increasing MFP as does the hardness. The TRS exhibits a maximum when plotted against increasing MFP[101] as shown in figure 2.11.

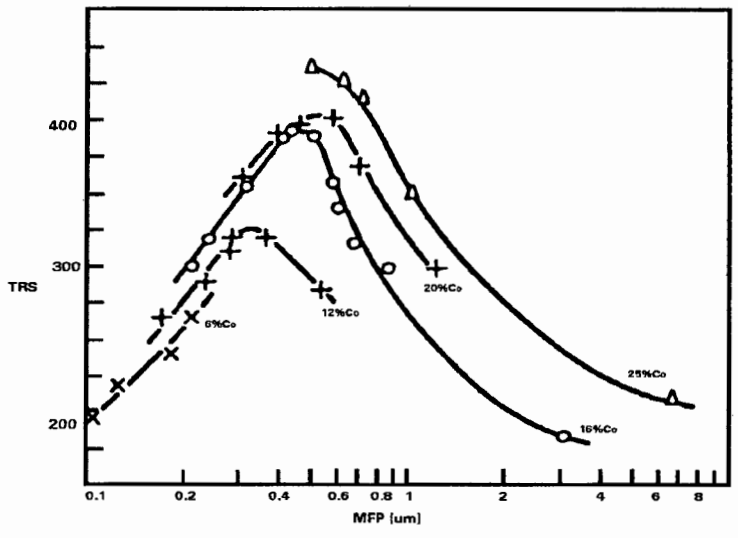

Figure 2.11 *The influence of MFP on strength. (After reference 14)*

2.5.3 CARBON CONTENT

It has been mentioned in an earlier section that carbon deficiency causes the appearance of the eta-phase, a double carbide of variable composition (e.g. W_3Co_3C), and excess carbon results in the presence of free carbon[32,114-116]. The effect of carbon content on the hardness and strength is shown in figure 2.12.

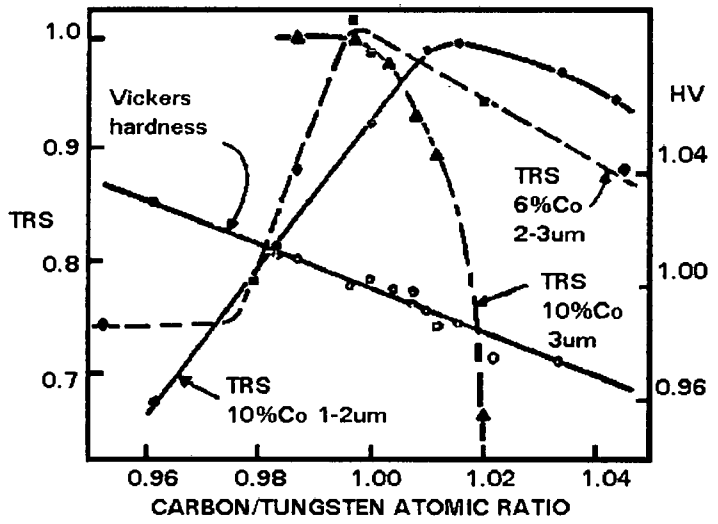

Figure 2.12 *Effect of C content on hardness and strength. (After reference 14)*

The Vickers hardness decreases linearly with increasing carbon content[105,117] while the TRS drops rapidly with increasing decarburisation[32,115]. This is considered to be due to the brittleness of the eta-phase and to the fact that the eta-phase removes cobalt from the binder[32,115]. To avoid embrittlement by the eta phase, commercial alloys usually contain a certain amount of excess free carbon. Some researchers[86,102,105] have reported only a slight decrease in the strength in the presence of free carbon, whereas other workers[114,117,118] show a pronounced influence, comparable to that of the eta phase. The transverse rupture strength has been shown to increase with increasing carbon in solution in fine-grained alloys, but decreases in coarse-grained alloys[32,86,105,117]. It is also believed that the composition of the binder phase will not be affected by the presence of free carbon, due to the limited solubility of carbon in the solid cobalt phase[119]. If excess carbon in an alloy is insufficient to precipitate free carbon, the density of the binder phase may actually increase slightly[119].

2.5.4 POROSITY

Studies of the total porosity on the strength of WC-Co alloys have been carried out by various researchers[81,120,121]. Their results show that material strength varies with the size and distribution of pores. However, hardness is not affected by the variation in porosity, within limits[122]. Thus attainment of a low level of porosity not exceeding 0.1%, is a key requirement during hard metal production. A uniformly

distributed residual porosity is usually present and is commonly accepted as not being harmful. Large pores often co-exist with other coarse flaws such as graphite inclusions, and uneven cobalt distribution[122]. The porosity level can be used to judge the success of the densification process[106].

Figure 2.13 shows the arithmetic mean and the standard deviation of the transverse rupture strength of commercial WC-10wt%Co alloys as a function of fractures initiated by pores. It was reported that these alloys did not exhibit any apparent porosity in polished sections.

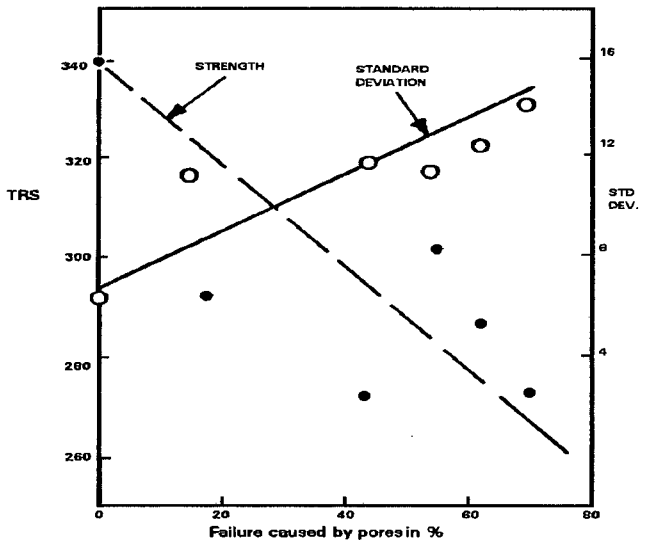

Figure 2.13 *Effect of pores on strength. (After reference 14)*

2.5.5 IMPURITIES

Impurities are introduced into cemented carbides in the powder production and milling processes. In milling, the powders can absorb iron, chromium or nickel from the stainless steel cladding of the mill itself or from the milling balls. While nickel, in small amounts, does not have any influence on the hardness and the strength, chromium and iron reduce the strength.

2.5.6 WC GRAIN SIZE

In liquid phase sintered alloys, the carbide grains tend to assume the shapes of flat trigonal prisms impinging upon each other but in insufficiently sintered alloys the crystal faces are not fully developed. Tungsten carbide crystals are anisotropic in

most of their properties. No anisotropy is present in sintered alloys because of the random orientation of the carbide particles. The strength of individual tungsten carbide particle decreases with increasing size[123] and that is probably one of the reasons for the different fracture mechanisms in fine-and coarse-grained alloys.

Numerous studies have been conducted into the influence of carbide grain size on the mechanical properties of the alloys[79,86,101-105,115,124]. Figure 2.14 shows that both the hardness and compressive strength decrease with increasing particle size. In figure 2.15 the TRS shows a pronounced maximum which lies at a particle size of approximately 3μm for a 12wt%Co alloy. This maximum has been explained in terms of crack propagation. In alloys with a small carbide size, fracture occurs mainly in the cobalt phase, but proceeds preferentially through the carbide particles in coarse alloys[32,101-104,124]. The maximum strength is reached when both phases have equal strength.

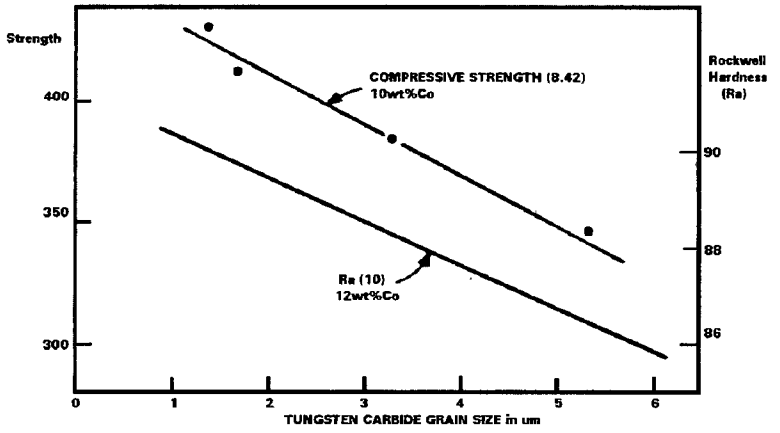

Figure 2.14 *Effect of WC grain size on hardness and compressive strength. (After reference 14)*

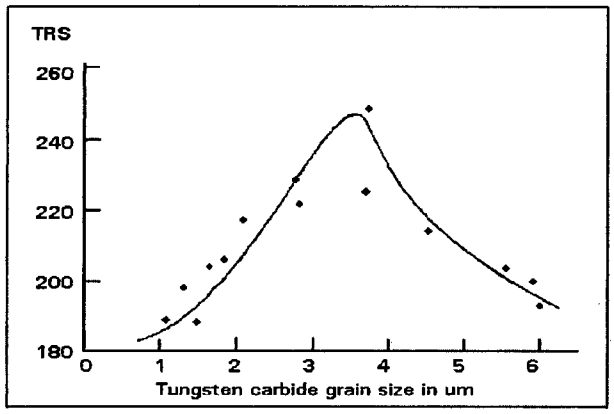

Figure 2.15 *Influence of WC grain size on transverse rupture strength. (After reference 14)*

The results of grain size measurement methods frequently depend on the method of preparation and examination of samples[125,126]. The most direct way of measuring the carbide grain size is to polish and etch a cross section of the microstructure. Quantitative metallographic techniques are then used to measure a mean value for the grain size either by point or area counting or by linear intercept techniques (Heyn method) or by measurement of the number of grains per unit area (Jeffries method)[127]. This can be performed using optical microscopes but, for many materials the grain size is too fine to be resolved optically and so electron microscopes must be used. In ultrafine grained hard metals the average grain size is very small, less than 0.5μm, and good quality images are difficult to obtain in conventional electron microscopes. Thus, there is great difficulty in trying to measure the carbide grain size of ultrafine hard metals.

Internationally, for the purpose of grade specification, there is as yet no widely agreed method for measurement of the carbide grain size, although in the research community it is fairly common practice to use the linear intercept technique outlined above. Attempts have been made to relate the carbide grain size to coercivity and these will be reviewed in the next section.

2.5.7 COERCIVITY

There have been several attempts at modeling coercivity to the carbide grain size[94,128-131] and in practice there are a few empirical equations that are being used. Many investigators have also tried to relate coercivity directly to the binder mean free path and the surface area per unit volume of the cobalt phase[94,131]. However, the relationship between the coercivity and the microstructure is more complex than a single factor can elucidate[119].

Coercivity is the measure of the force required to move the magnetic domain walls in the cobalt phase. This force that is related to the Co/WC interphase area, because the domain walls are pinned by these phase boundaries. The Co/WC interphase area is inversely related to the tungsten carbide grain size. For smaller values of the latter the interphase area increases and consequently so does the coercivity. However, coercivity also changes with changes in the cobalt

composition and this should be allowed for in empirical equations relating carbide grain-size to coercivity[127].

Furthermore, difficulties can arise when trying to correlate coercivity with grain size due to the effects of differences in the cooling rate from the sintering temperature. This results in changes to the composition of the binder phase that can have a significant effect on the coercivity. For example, in low carbon content hard metals it is possible to precipitate Co_3W in the binder phase on aging of the hard metal after accelerated cooling. This procedure results in very significant changes in coercivity.

It has also been shown[132] that deformed hard metals show a significant increase in coercivity due to deformation of the binder phase, i.e., creation of phase boundaries, twins and stacking faults, which is reduced on subsequent annealing. In addition, the role of WC/WC contiguity must also be acknowledged since it can be seen that two materials of different contiguity but similar grain size will have different interphase areas and hence different coercivities[132]. Finally, since the carbon content influences the binder composition and the final grain size in sintered parts, the coercivity is also very sensitive to changes in carbon content.

Some of the models that have been developed to relate coercivity to the tungsten carbide grain size are empirically based and some are physically based. There are significant disagreements amongst models and the major source of discrepancy is likely to be due to differences in the definitions and measurement methods used for grain size.

Equations 2.4, 2.5, 2.6 and 2.7 are some empirical models that are being used. However, it is good to mention that each equation works best for the range of materials on which it was based, so care should be exercised when attempting to use it outside of those ranges. In each of the equations K is the coercivity and V_{Co} is the cobalt volume fraction.

Porat & Malek[130]:

$$d_{WC} = 0.3\left(\frac{80}{K}\right)^{0.57(1/V_{Co})^{1/3}} \qquad \text{...(2.4)}$$

Fang & Eason[119]:

$$d_{WC} = 73(1 - 1.03\exp[-5V_{Co}])\left(\frac{1 - V_{Co}}{KV_{Co}}\right) \quad \text{...(2.5)}$$

Roebuck[132]:

$$d_{WC} = \frac{7.93}{K - 6.71} \qquad \textit{for } K > 12.5kAm^{-1} \quad \text{...(2.6)}$$

$$d_{WC} = \frac{10.9}{K - 1.79} \qquad \textit{for } K < 12.5kAm^{-1} \quad \text{...(2.7)}$$

One of the problems associated with using coercivity to determine the carbide grain size is that the measurement only gives a single value and does not indicate narrowness or spread of size distribution[127]. Thus, coercivity can be used in principle to predict grain size but agreement is needed on a standardized method to relate it to grain size.

2.5.8 CONTIGUITY

Lee and Gurland[133] found that the existence of a continuous skeleton is very probable in high carbide alloys. The skeleton thus represents an important load-bearing element in the structure. Not every carbide grain takes part equally in the skeleton structure and it has been proposed that hard metals comprise of a partially connected structure with the volume fraction of the continuous carbide volume equal to the volume fraction of the carbide phase, multiplied by the contiguity, i.e., $V_C = V_{wcC}$.

As a result contiguity has been defined as a quantitative measure of skeleton formation, which is defined as the ratio of grain boundary surface (WC/WC interface) to total surface (WC/WC + WC/Co interface)[79,98,134]. Contiguity drops very rapidly with added cobalt and it has also been reported[134] that the contiguity also depends on the processing history, such as, sintering time and temperature, or the mixing procedure.

Figure 2.16 shows the effect of contiguity on hardness and transverse rupture strength.

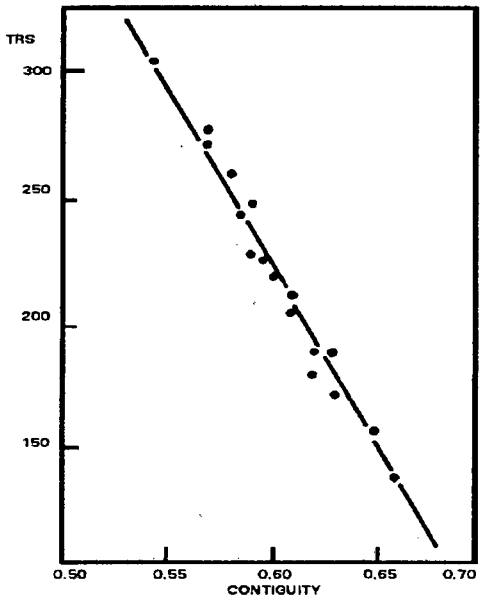

Figure 2.16 *Influence of contiguity on strength. (After reference 14)*

2.5.9 HARDNESS

➢ General

The hardness of a material has been defined as a measure of the material's ability to resist plastic deformation under a load applied to the material by a hard indentor[135]. It is measured by the mean indentation force resisted by the material when the deformation is fully plastic[135,136]. Since it is a force or pressure it can be related to the flow stress of the material[137].

Thus hardness is a material property that depends on the microscopic structural details of the material such as the amount of cobalt present in the material and the size of the carbide grains[135]. Roebuck[133] applied plastic limit analysis to an idealized model of the microstructure of cemented carbides and proposed equation 2.8 for the theoretical hardness of a hard metal.

$$H_c = V_{wc}CH_{wc} + (1 + V_{wc}C)H_m \quad \text{...(2.8)}$$

Where:

V_{wc} ⇒ volume fraction of the WC

C ⇒ contiguity

H_{wc} ⇒ hardness of WC

H_m ⇒ hardness of the matrix

They found this equation to be in good agreement with experimental data. From their results they deduced that contiguity is an important microstructural parameter for cemented carbides. However, ASTM and ISO methods do exist that provide a procedure for the determination of a material's hardness using calibrated equipment.

It has been reported[132] that comparison of hardness values determined on the newly developed very fine-grained hard metals is proving to be difficult because of the following factors:

- the use of a Rockwell indentor in the USA and Japan compared with the use of a Vickers indentor in Europe, UK and elsewhere. It is widely agreed that there is no direct scale comparison between the two methods;
- the occasional use of microhardness testing equipment (with loads of 1kg) which may only indent individual grains and hence the hardness is not indicative of the complete alloy;
- the lack of a standard surface preparation method to eliminate residual stresses which may be present if insufficient surface preparation is done;
- the problems that are associated with the measurement of small indentations as errors are maximized due to a lack of resolution.

➢ **Relationship between hardness and carbide grain size**

A limited amount of modeling has been done to relate the carbide grain size to hardness. A study of cemented carbides over a limited range of grain sizes has shown that the relationship can be expressed adequately by a Hall-Petch type relation shown in equation 2.9 where a and b are constants[133].

$$Hwc = a + bd^{-1/2} \ (kg/mm^2) \qquad \ldots(2.9)$$

➢ **Relationship between hardness and binder mean free path (MFP)**

Hardness has been shown to increase with a decrease in the binder mean free path (MFP). The ascending rate of the hardness with decreasing MFP in ultrafine hard metals has been shown to be much faster than the rate in the coarser alloys.

Gurland and Bardzil[101] suggested that the hardness of sintered cemented carbides varies with the MFP according to an exponential relationship.

➢ Relationship between hardness and cobalt

Schubert *et al.*[23] found that a higher binder content at a given hardness, combined with a lower average carbide grain size, did not necessarily mean a higher toughness. In particular, at lower hardness values this relationship does not exist. At higher hardness values high binder contents can reduce the carbide contiguity and thus improve the hardness-toughness relationship.

The hardness of the binder phase has also been described by Roebuck *et al.*[133] as a function of binder thickness and is given by a Hall-Petch type relation as shown in equation 2.10 where and b are constants and λ is the binder mean free path.

$$H_m = a + b\lambda^{-1/2} \ (kg/mm^2) \qquad \ldots(2.10)$$

➢ Relationship between hardness and fracture toughness

Fracture toughness and hardness of cemented carbide hard metals vary in different ways when the composition and/or microstructure of the material are varied. However, not all published results agree on the type of relationship that exists between these two properties. For example, Ingelstrom and Nordberg[112] found that the two variables have an 'almost linear' relationship that seems to be confirmed by Pickens[138], while Warren and Johannesson[139] and Chermant and Osterstock[140] found clear non-linear relationships. Even Chermant and Osterstock[140] and Pickens[138] do not agree on the toughness and hardness results at a constant carbide grain size. Chermant and Osterstock[140] again found a non-linear relationship while Pickens[138] relationship could be linear, although the scatter in his results precludes determining this with certainty. O'Quigley *et al.*[141] investigated the relationship at a constant grain size and found it to be linear.

Figure 2.17[21,139] shows a comparison of the toughness of different WC-Co grades at a constant hardness level. A significant gap appears between the highest and the lowest obtainable toughness values at a certain hardness, which indicates that the

hardness-fracture toughness relationship of individual alloys varies with changes in the composition/microstructure.

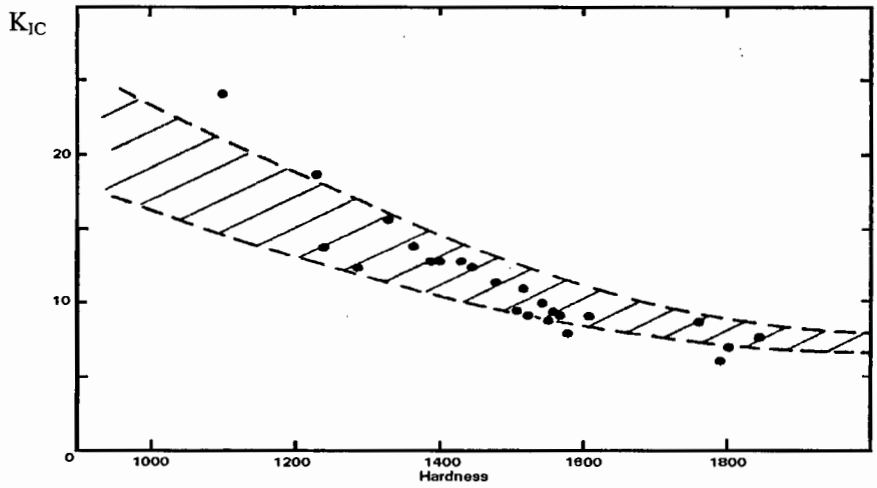

Figure 2.17 *A graph of fracture toughness against hardness for a range of hard metals. (After reference 21)*

It has been shown that the increase of hardness in the ultrafine hard metals does not always decrease their bulk fracture toughness[142], behavior opposite to what is found in the coarser alloys. This implies that different toughening mechanisms may exist in the conventional and ultrafine composites. Jia and Fischer[142] explained it in terms of the plastic deformation concept in conventional composites whereas for ultrafine hard metals, the bridging ligament mechanisms play a significant role in the alloy's toughness. This explanation was based on the fact that the bulk fracture toughness is related to crack propagation through the phases of the material.

2.6 FRACTURE TOUGHNESS TESTING

2.6.1 CONCEPT OF K_{Ic}

Irwin *et al.* first described the concept of K_{Ic} in 1958[143], but he only introduced the symbol K two years later[144]. K_{Ic} is regarded as a material property as it represents the lower limit of effective toughness with an increase in the degree of constraint to plastic deformation and it has the general tendency of decreasing with an increase in the yield strength of the material. The simplest definition of the K_{Ic} toughness of a material is the measure of the load that a specimen containing a crack can sustain without fracturing.

The value of K_{Ic}, is based on the stress analysis of cracks in linear elastic materials[143-146], and is related to K_I the mathematical quantity that is the opening mode stress intensity factor of a material. Generally, K_{Ic} values are determined by recording the load needed in bending or tension to propagate an artificial crack of known depth in a single-edge notched beam, or specimen of similar type. The K_{Ic} value is then determined by equation 2.11:

$$K_{Ic} = \varphi\sigma_f(\pi a)^{1/2} \qquad \text{...(2.11)}$$

Where: $\varphi = [a/W]^{1/2}-3.07[a/W]^{3/2}+14.53[a/W]^{5/2}-25.11[a/W]^{7/2}+25.80[a/W]^{9/2}$

σ_f = applied stress

a = crack length

W = width

φ[147] is a polynomial function for an edge crack in a finite width sheet in bending. Values for different types of specimen geometry's and crack types are available in reference 148.

There are many techniques that have been proposed to measure fracture toughness and for these techniques, various types of specimen configurations exist. The test procedures are based on mathematical analysis, which involve the specimen geometry, loading conditions, crack growth and the stresses that arise during fracture. Tests can be carried out in either bending or in tension. The increasing diversity of different fracture toughness tests leads to a difficulty in the comparison of data from different tests. Though numerous tests exist, only the four commonly used techniques will be reviewed in this section, two of which have been chosen for the research work conducted in this thesis.

2.6.2 THE DOUBLE TORSION METHOD

Outwater and Gerry first introduced the concept of the double torsion method in 1970[149]. In their work they subjected a specimen to a constant load while directly measuring the crack velocities by monitoring the crack lengths created. From this they established that the crack velocity remained constant under a constant load.

On the basis of the constant crack velocity proposal, Williams and Evans[150] pointed out that as long as the crack front adopted a stable shape soon after loading, all elements along the front could be regarded as moving with constant velocity along the specimen. They also assumed that the crack front is at all points' perpendicular to both the upper and lower specimen surfaces.

This approach results in the K_{Ic} value being a continuous measurement as the crack propagates and K_{Ic} then becomes a function of the average crack velocity which corresponds to a selected rate of crack opening displacement[151]. Due to this continuous nature, the test appears to eliminate factors such as crack tip radius and the crack location with respect to microstructure flaws. These factors have been shown to effect the K_{Ic} values that are obtained by other toughness tests.

The test method is simple and its advantages include simple specimen geometry, ease of pre-cracking and the use of four point loading. Figure 2.18 shows the basic specimen geometry that consists of a plate, which has a partial crack down the center, forming essentially two beams. The specimen center is grooved to a depth of 0.5-1.0mm using a spark erosion machine. The groove width is approximately 0.6mm and the groove can be cut on one or both sides of the plate. An initial notch of 3mm in length is cut into the specimen to be the pre-crack. The plate is loaded in four point bending at one end as shown in figure 2.18, causing the crack to propagate down the center of the specimen. The groove helps to constrain the propagating crack to the center of the specimen.

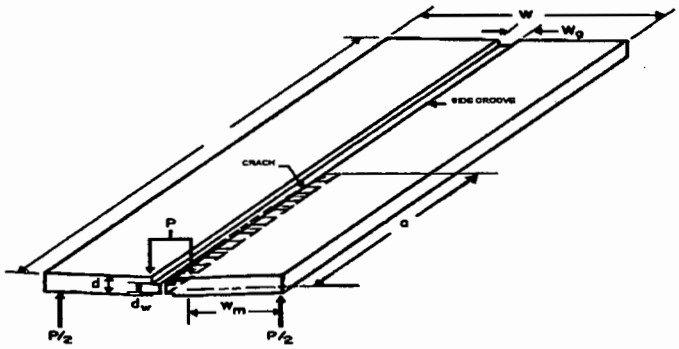

Figure 2.18 *The test piece configuration for the double torsion method. (After reference 152)*

The K_{Ic} value is determined by the relationship shown in equation 2.12.

$$K_{Ic} = PW_m [(3(1+2v)^{1/2})/(Wt\ T^3)] \quad \text{...(2.12)}$$

Where:

P = applied load,
W_m = moment arm
W = specimen width
t = crack width
T = specimen thickness
V = Poisson's ratio

Due to the test's unique feature of propagating stable cracks, the effects of variation in parameters such as crack opening displacement rate, temperature, or environment, can be studied by noting only the changes in the applied load.

From equation 2.12, K_{Ic} is shown to be independent of crack length. However this factor has been critically assessed by various researchers. It has been shown that the independence of crack length is only valid over a limited range of crack lengths. In addition, when the crack tip is close to either end of the plate, K_{Ic} then becomes dependent on the crack length. There have also been some discrepancies concerning the validity of using this test for thick specimens[153]. However, Fuller[152] found that by adding a correlation factor to the equation, which he based on the elastic theory for thick plates, that this method could be used for thick plates.

2.6.3 THE BEND TESTS

The most common bend tests used to determine the toughness of cemented carbides have been three point bending[109,154,155] and four point bending[112,156,157]. Before the specimen can be loaded in these tests they need to be pre-cracked. Importantly, the validity of a pre-cracking technique to determine a material's fracture toughness, is its ability to introduce a sharp crack into the specimen that is equivalent to a 'natural' crack.

➢ Pre-cracking techniques

The most common method of introducing a pre-crack into a metallic material is by means of a fatigue method[158]. Successful pre-cracking has also been done by means of electron discharge machining, wedge indentation[157], impact-loaded wedge indentation[114,159] and by controlled fracture[160]. Two of these methods will now be dealt with in more detail.

▪ Fatigue pre-cracking

Early researchers found that the introduction of a fatigue crack into cemented carbides as difficult due to the brittle nature of the metal[161]. In addition the stress intensity factor required for pre-cracking is often very close to the critical fracture toughness value of the carbides[162].

However, by the 1900's, researchers were discovering easy, practical ways of carrying out fatigue pre-cracking. For example, Suresh and Brokkenbrough used uniaxial cyclic compression[163] to produce the pre-crack. In 1991, Iizuka and Tanaka[156] used compressive fatigue cycling at room temperature to do the pre-cracking. Their method made use of a lower maximum load than the one used by Suresh and Brokkenbough[163].

Initially a notch is introduced into the specimen by means of spark cutting to a depth of 1.5mm. Thereafter the fatigue pre-cracking is carried out using compressive cyclic loads with the load ratio of P_{min}/P_{max} kept at a constant level. Figure 2.19 shows the schematic of the pre-cracking method and the four point bend test used to determine the toughness. This method was found to produce stable crack propagation and a maximum pre-crack length of 0.13mm could be achieved. It was also found that that crack closure would often result when the cracks were extended for too long, but contact portions of the metal were removed by etching. The effect of crack tip profile is considered to be negligible when using this method of pre-cracking.

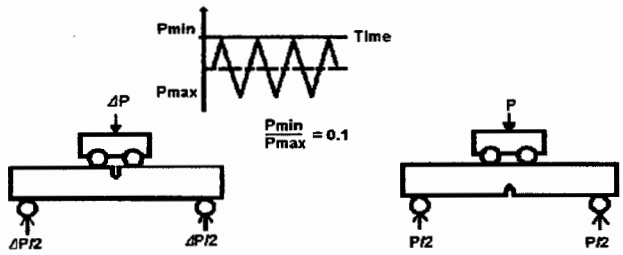

Figure 2.19 *Schematic of pre-cracking method. (After reference 156)*

- **Electron discharge machining (EDM)**

The EDM method was first used by Yen[164] when he compared K_{Ic} results from mechanically pre-cracked double cantilever beam (DCB) specimen with EDM notched single-edge notched beam (SENB) specimen. The SENB specimen configuration is illustrated in figure 2.20. He found the results from the SENB specimen to be much lower than those obtained by using the DCB method. Chermant *et al.*[110] found similar results when they compared EDM notched SENB specimen with diamond ground notches in SENB specimen. He too discovered that the EDM specimens were giving lower K_{Ic} results. This difference was attributed to the presence of small local curvature regions at the root of the EDM notch. Thermal microcracks are also found at the root of the notch and these have been found to set up a dual notch-microcrack system[111]. They also noted that at an EDM notch radius of less than 70μm the K_{Ic} values reached a constant minimum. This reasoning was used to assert that EDM produces a natural crack, making it a valid pre-cracking technique.

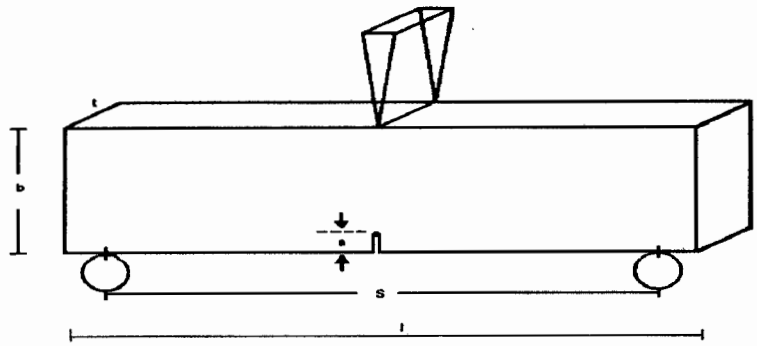

Figure 2.20 *SENB specimen configuration. (After reference 164)*

2.6.4 THE SHORT ROD AND SHORT BAR TEST

Barker first introduced the short rod and short bar fracture toughness tests in 1977[165]. The specimen dimensions for both the rod and bar were designed so that K_{Ic} measurements made using both specimens are interchangeable. The advantages of this method include the dependence of the K_{Ic} value solely on the peak load recorded during the test and since this value depends only on the specimen geometry, the method is considered to be independent of material properties. This means that there is no need to know the crack length measurement that is always required by other fracture toughness tests. The specimen configurations for both the short rod and short bar are illustrated in figure 2.21 below.

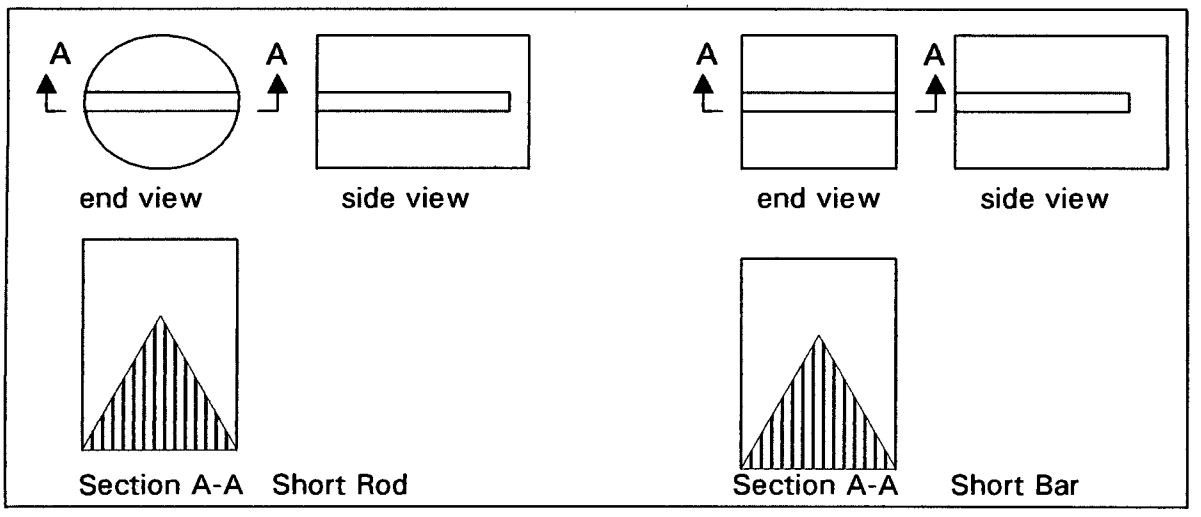

Figure 2.21 *Short rod and short bar specimen configuration. (After reference 2)*

The test specimen can be loaded in two different ways to measure the maximum force. In the first method, grips are used to pull the specimen apart as shown in figure 2.22. In the second method a thin inflatable bladder, referred to as a flatjack, is placed inside the grooved specimen as shown in figure 2.23 and by applying pressure to the bladder, a crack is initiated at the chevron tip.

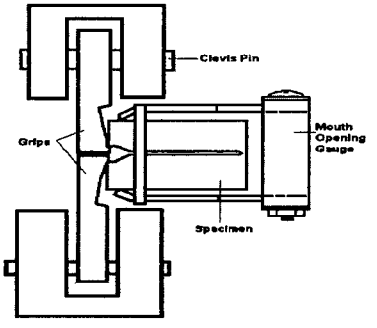

Figure 2.22 *Load cell loading method for the short rod/bar test. (After reference 2)*

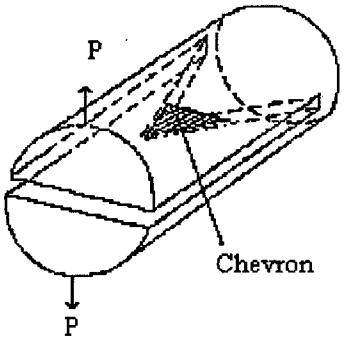

Figure 2.23 *Fractometer loading method for the short rod test.*

During initial loading of the specimen, crack growth from the tip of the chevron shape is stable and thus a real "natural" crack is formed in the sample, eliminating the process of pre-cracking. The applied load increases until a critical maximum load is reached and recorded. From this load the K_{Ic} measurement is determined. Thereafter, the load decreases and the sample eventually fractures into two halves.

The crack once initiated will grow uniformly and will remain perpendicular to the axis of the specimen provided that the sample is symmetrical about the crack plane. The onset of crack growth instability results in the stress intensity at the tip of the crack to always be of equal value to the K_{Ic} value during the test. Also, in this test the crack speed varies with the loading rate, while the rate of change of K_{Ic} does not.

The K_{Ic} value, using the flatjack method is determined according to equation 2.13[165,166].

$$K_{ic} = AF_c/[B^{3/2}(1-\nu^2)^{1/2}] \quad \text{...(2.13)}$$

Where:

A = a dimensionless constant

F_c = maximum load

B = specimen diameter

ν = Poisson's ratio

Barker[165] defined the constant A by determining a condition for crack growth stability that was extrapolated from Irwin and Kies's[166] condition for crack position stability. The constant A, is based on the calibration of the specimen geometry for the test method. Once a standard calibration has been made, the value of A may be used for any specimen which has the exact same geometrical proportions as the

standard test piece used to make the calibration. A has been defined by equation 2.14.

$$A^2 = (B^3/2b_c)[(d(cE))/da]_{a=ac} \quad \text{...(2.14)}$$

Where:

B = the specimen diameter
b_c = the crack width at the maximum load
c = specimen compliance at crack length a
E = Young's Modulus
a = crack length
a_c = crack length at maximum load

In experiments conducted by Barker in 1977 he found the value for A to be 20.8 ± 1.4.

The test described above is valid for materials that show ideal linear elastic fracture mechanics (LEFM) behavior. However, at times, some materials exhibit non-ideal LEFM behavior and therefore correction factors have been designed which can be added to equation 2.14 which can then be used to determine the fracture toughness of the material.

Non-ideal linear behavior is illustrated in figure 2.24, in the form of crack jumping and in hysteresis loops that occur from unloading/reloading paths. Extreme crack jumping may be associated with the stiffness of the testing machine. At the point of crack growth in the specimen, the stored elastic strain energy in the machine is released causing a jump in the crack. It has been proposed that a separate K_{Ic} value may be determined for each jump[167]. In the case of the hysteresis loops, ambiguity may result in the measurements taken of the unloading slope. It has been suggested that these loops are due to bridges of material which connect the crack faces behind the crack front[167].

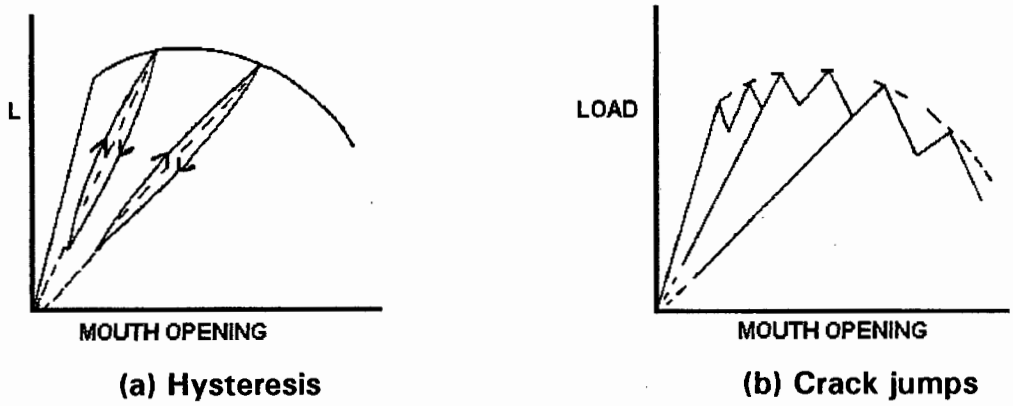

Figure 2.24 *Non-ideal linear behavior during crack propagation. (After reference 168)*

Non-ideal LEFM behavior also arises when the unload/reload paths do not extrapolate through zero as is shown in figure 2.25. It has been postulated that the cause of this is due to the presence of longitudinal residual stresses in the specimen, shown in figure 2.26. For these stresses a plasticity factor has been designed by Barker[169,170] to correct the K_{Ic} equation values.

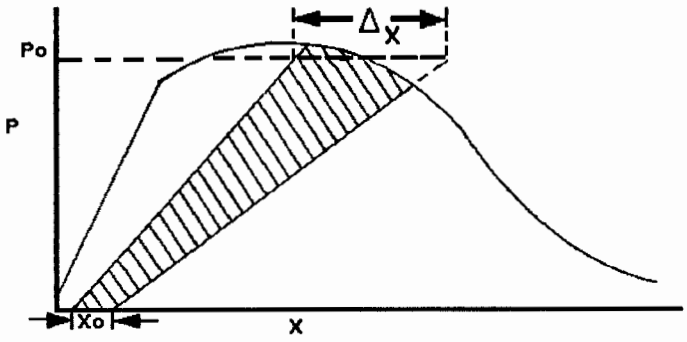

Figure 2.25 *Another form of non-linear LEFM behavior when the path does extrapolate through the origin. (After reference 169)*

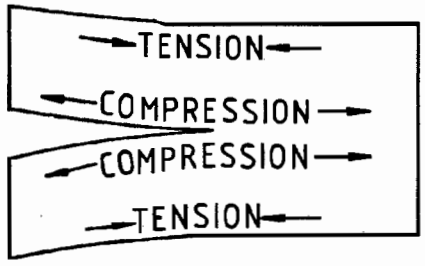

Figure 2.26 *Stress pattern in the specimen during testing. (After reference 168)*

This short rod/bar fracture toughness test designed by Barker has been transposed into an approved ASTM test method for determining the fracture toughness of cemented carbides[2].

2.6.5 INDENTATION FRACTURE TOUGHNESS TESTS

There exists a set of empirical tests for hard metals that is based on the measurements of the surface cracking that occurs during indentation in a hardness test. The cracks are mainly circumferential and radial for spherical and cone indentors, and mainly radial for pyramid indentors. Extensive efforts have been made to relate the degree of surface cracking to the property - plain strain fracture toughness (K_{Ic}).

Discrepancies often occur when trying to compare values from the various tests because of the effects from differences in indentor geometry, work-hardening rates of the test materials, and the manner in which the results are expressed. However, it has been shown that provided these limitations are realized, the test gives useful information on mechanical properties[60], and impact erosion and abrasion wear mechanisms[171]. The tests can also play a role in quality control or product development, either in the original form of the test or with certain modifications[172].

Three types of indentation cracks have been expressed empirically in relation to toughness namely, Hertzian cone cracks, semi-circular median cracks and Palmqvist cracks. These crack types are shown in figure 2.27. As the Palmqvist crack test was used for this project a detailed review of this test will be given.

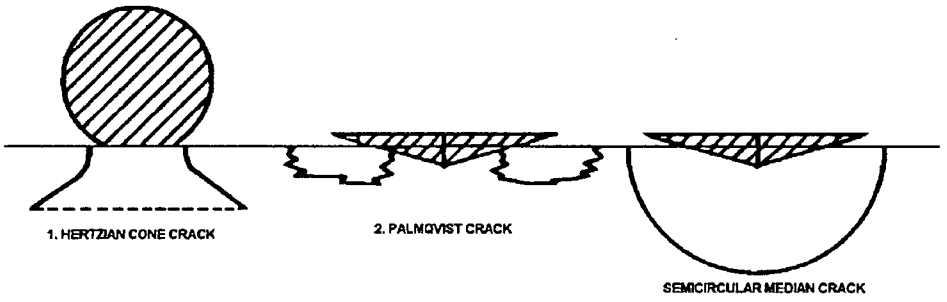

Figure 2.27 *The different types of indentation cracking. (After reference 76)*

2.6.5.1 Palmqvist crack test

Palmqvist[1] was the first to observe that a linear relationship exists between the sum of the lengths(Σl) of the four cracks from the corner of a Vickers hardness indentation, and the load (P) applied to the indentor: This relationship is shown in equation 2.15.

$$\Sigma l = a_1 P - a_2 \qquad \text{...(2.15)}$$

Here a_1 and a_2 are constants that depend on the composition and the microstructure of the material. It was found that the constant a_1 decreased with increasing cobalt content while a_2 increased. Palmqvist also inferred that a_1 is an indirect measure of the work required to produce cracks.

Later, Exner[173] found that prolonged polishing of the surface, before indentation, led to the disappearance of the constant a_2. Work done by Luyckx[174], also confirmed that the value of a_2 depended on the preparation of the surface, at least for cobalt contents up to 9wt%. The value of a_1 seemed to be independent of the degree of polishing, within reasonable limits[173,174].

Thus equation 2.15 was reduced to $\Sigma l = a_1 P$ and finally after Exner[173] defined $1/a_1$ as "W", the crack resistance of a material, then in the form of equation 2.16:

$$W = \frac{P}{L} \qquad \text{...(2.16)}$$

Where:

$W \Rightarrow$ Crack resistance (N/m)

$P \Rightarrow$ Applied load (N)

$L_i \Rightarrow$ Total crack length (m)

"W" has since become known as the Palmqvist toughness and the cracks that emanate from the apex of a Vickers indentor are now referred to as Palmqvist cracks.

Exner[173] also showed that the Palmqvist cracks have a constant length at a given load and in a given material only if the compressive stresses introduced by grinding the surface are completely removed either by prolonged polishing or by annealing.

He also established the conditions under which the crack length is reproducible and these, along with the importance of correct surface preparation, will now be reviewed.

- **The influence of sample preparation on the Palmqvist cracks.**

Based on Exner's[173] observations, Roebuck[132] concluded that the method of surface preparation in metals is a source of uncertainty, since the development of the residual stresses induced by grinding and polishing effects the indentation crack length measurements, which in turn effects the calculated Palmqvist toughness values. The Vickers indentations need to be made on a surface that is free from any residual stresses, and the surface should be prepared in such a way as to eliminate these stresses and in doing this, the maximum crack length is obtained.

According to the theory of thermally introduced stresses, the binder phase in WC-Co alloys is assumed to be under tensile stress in the as-sintered condition. This is due to the coefficient of thermal expansion of the cobalt phase being three times that of the tungsten carbide phase. Also, the compressive stresses in the carbide phase increases with increasing cobalt content, but deviations from this statement have been found in very high cobalt content alloys. In work done by Snell and Parnama[175] they found that the carbide phase is always under compressive stresses independent of the amount of cobalt present, the size of the carbide grains or any surface treatment. The stress states of the tungsten carbide and the cobalt phases are shown in figure 2.28.

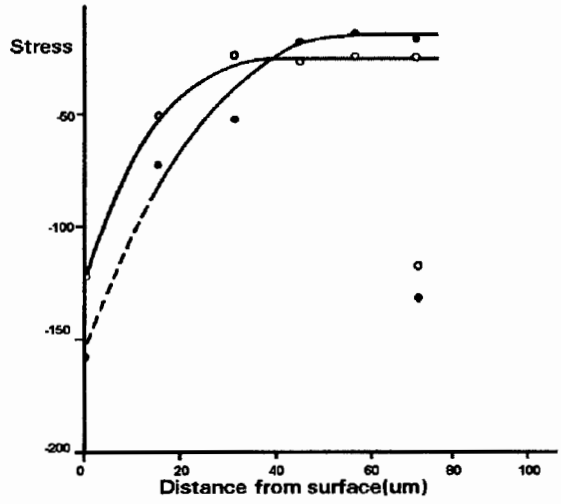

Figure 2.28 *Stress distribution in the two phases in a WC-Co alloy. (After reference 173)*

When grinding a sintered alloy, Exner[173] found that the compressive stresses introduced by grinding were a function of the distance from the ground surface. These compressive stresses near the surface were found to be balanced by induced tensile stresses toward the middle of the specimen. Thus grinding superimposes compressive stresses in the surface layer that increases the compressive stresses in the tungsten carbide and decreases the tensile stresses in the cobalt phase. As a result any residual stresses which may be present would be of the same sign and magnitude in the different phases. This finding was in agreement with an axiom developed by Palmqvist[1].

Exner[173] also found that the residual tensile stresses present in the cobalt after being cooled down from the sintering temperature added to the effective indenting load and facilitated crack propagation. He inferred that when a carbide grain is hit by a hard particle during grinding, it may break allowing the cobalt matrix to relax or the tungsten carbide particle could change its position putting the cobalt matrix under greater tensile stress on one side and compressive stress on the other side. Thus, some of the cobalt layers are stronger in the unmachined state and as a result can resist an applied force and stop a crack from propagating. This is shown in figure 2.29.

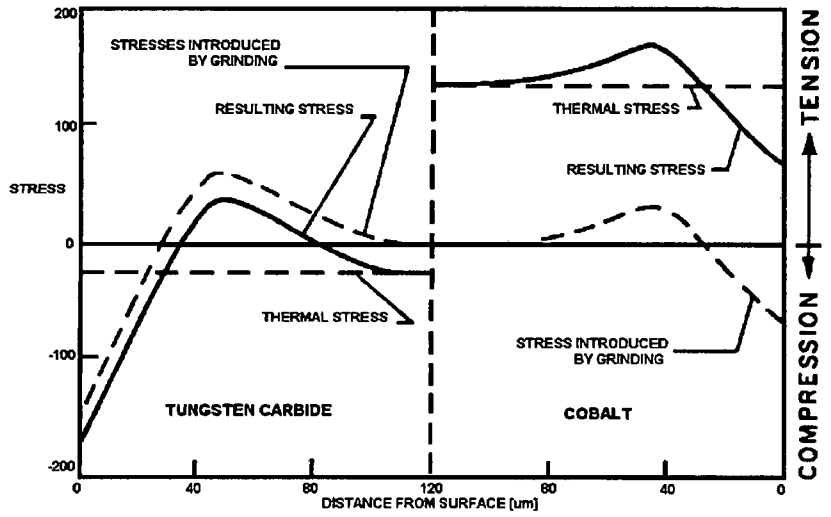

Figure 2.29 *Stress distribution vs. distance from surface in a WC-Co alloy. (After reference 173)*

In further work done by Exner[173], he explained that ground surfaces produced short cracks as a result of surface deformation and the compressive stresses induced

during the grinding process. He found that polishing and annealing restored the stress pattern to the original one produced exclusively by the residual thermal stresses. In fact, by making x-ray measurements it was shown that the stress state of an annealed or polished surface is similar to the stress state as it would be in fracture, which is noted to be the best approximation of an undeformed surface. He also concluded that annealing after polishing would only give a change in the crack length if the polishing had caused work hardening of the cobalt or carbide grains, or caused tensile stresses in the cobalt phase.

The main requirement of surface preparation is that it should be prepared in such a way to obtain the maximum crack length, which is determined exclusively by the indenting load and the properties of the alloy, such as the residual thermal stresses, alloy composition and phase structure. The crack length will also be impeded from reaching a maximum length if the surface preparation causes any extra compressive stresses into the cobalt phase.

Various authors have used equation 2.17, first developed by Exner[173], to determine at what stage of polishing the maximum crack length is achieved. The equation is used to calculate the thickness of the layer of material removed after polishing with various grades of diamond paste for set time periods.

$$A = \frac{D_1 - D_2}{2}.\cot\frac{\alpha}{2} \qquad \text{...(2.17)}$$

Where: A $\Rightarrow$ thickness of layer removed;

$D_{1/2}$ $\Rightarrow$ diagonals of the Vickers indentation before and after polishing;

α $\Rightarrow$ angle between the faces on the top of the Vickers pyramid.

No direct relationship exists between the polishing time and the amount of material removed, however, the crack length increases proportionally to the thickness of the layer removed and at some point reaches a constant value. This is shown in figure 2.30.

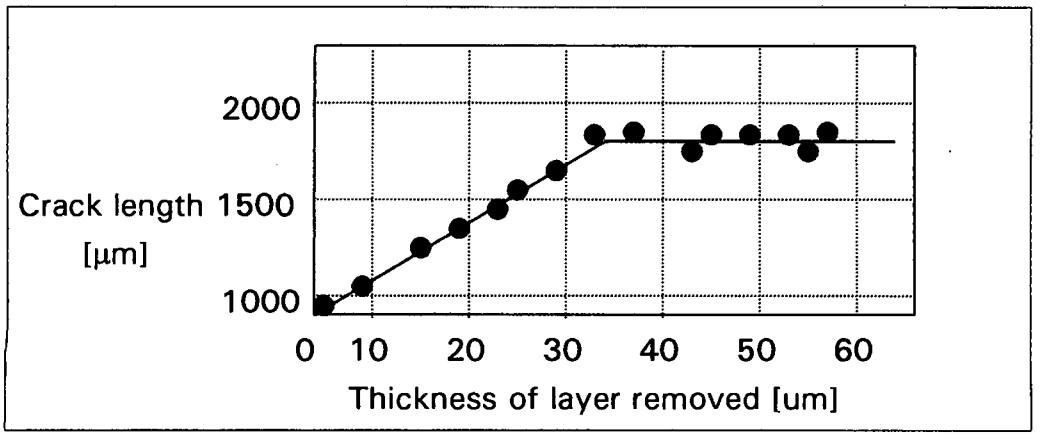

Figure 2.30 *Influence of polishing time on material removal. (After reference 173)*

A linear relationship exists between crack length and the applied load[76,173,175-179]. This relationship is shown in figure 2.31. For unstressed materials this graph should pass through the origin. However, when it does not pass through the origin, it implies that an initial load is required before cracking will occur in the material[76].

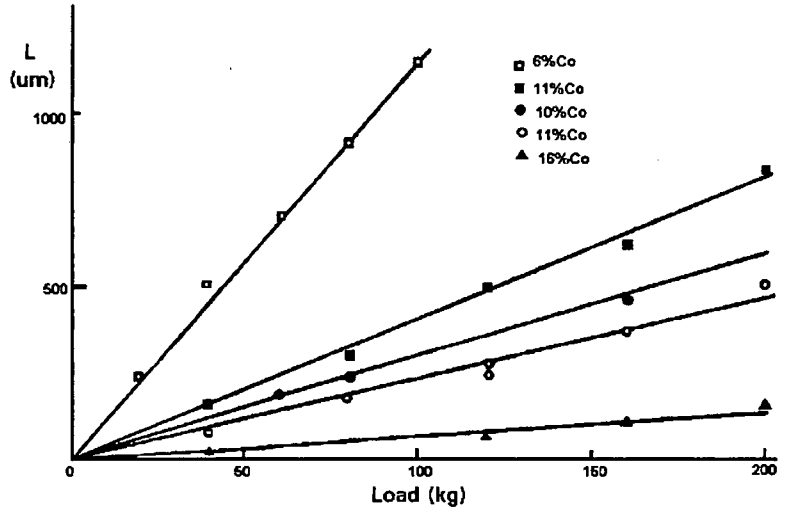

Figure 2.31 *Effect of increasing indenting load on crack length. (After reference 178)*

- **Relation of W to K_{Ic}**

W denotes the resistance to the initiation and the growth of the crack, while K_{Ic} denotes only the resistance to the propagation of cracks and as a result the one cannot be used as a substitution for the other[178]. Thus attempts have been made to find a relationship between K_{Ic}, the bulk fracture toughness and W, the Palmqvist

toughness. Crack resistance in indentation can be used as a measure of toughness in its own right or related empirically to conventional fracture toughness[76].

From analysis based on linear elastic fracture mechanics[179], the correlation between W and K_{Ic} was initially thought to have been a direct linear one as indicated by equation 2.17 where a and b are constants.

$$W = a + bK_{Ic} \qquad \text{...(2.17)}$$

Based on correlations of W and K_{Ic} independently with hardness or binder mean free path, Viswanadham and Venables[179], and subsequently Peters[177], suggested the same direct linear relationship between W and K_{Ic}. Peters[177] established that this relation worked well up to a cobalt content of 10wt%, after which a marked deviation in linearity was observed. This observation was confirmed by Exner *et al.*[180] and Perrot[181] who found experimentally that the relationship between W and K_{Ic} was linear only up to $K_{Ic} = 0.2 kJ/m^2$ and $W = 1 MJ/m^2$.

The change in linearity has been attributed to a change in the fracture mechanism in the metals[181,182]. In low cobalt alloys, fracture occurs predominantly by rupture of the Co/WC interlayer, whilst at high values of cobalt content, WC cleavage takes place presumably via the dislocation pile-up stress generated by the plastic deformation in the binder[182,183]. The change in linearity has also been attributed to changes in the relative amounts of crack growth occurring during loading and unloading, respectively, of the indentor[181,184].

Later, when Luyckx[174] plotted $1/K_{Ic}$ against hardness for grades with the same grain size, she found a monotonic correlation, which was thought to be linear. It was shown that at a constant grain size W and K_{Ic} are related as shown in equation 2.19 with α and β being constants.

$$1/W = \alpha/K_{Ic} + \beta \qquad \text{...(2.19)}$$

Niihara[185] and Warren and Matzke[76] independently suggested a relationship of the form shown in equation 2.20 where b is a dimensionless constant and H is the material's hardness. The equation predicts that W is constant. Lawn and Wilshaw[186] gave a similar equation.

$$K_{Ic} = \left(\frac{1}{3\left[1-\nu^2\right]\left[2^{1/2}\pi \tan\omega\right]^{1/3}} \right)\left(\frac{[HP]^{1/2}}{[4a]^{1/2}} \right) \qquad \text{...(2.21)}$$

Where:

$\nu \Rightarrow$ Poisson's ratio

$\omega \Rightarrow$ half the indentor angle

$H \Rightarrow$ hardness

$P \Rightarrow$ indenting load

$a \Rightarrow$ crack length

Equation 2.21 is also written in the more conventional form of equation 2.22 where ν is 0.22(typical for WC alloys) and ω is 68, which gives b a value of 8.89×10^{-2}.

$$K_{Ic} = b(HW)^{1/2} \qquad \text{...(2.22)}$$

The results of Shetty et al[3] show that the Palmqvist cracks in cemented carbides follow the linear dependence of crack length on indentation load rather than the two-thirds power dependence expected for the half-penny cracks. Their regression analysis also shows that on an equal basis of comparison the two models do give very similar predictions, especially for the low binder cemented carbides. The model works for alloys with fracture toughness values up to $15 MNm^{-3/2}$.

Chapter 3

EXPERIMENTAL METHODS

3.1 INTRODUCTION

In this chapter, details of the experimental methods used in investigating the fracture toughness of various tungsten carbide hard metals are given. The two fracture toughness test methods employed are described in detail. Various experimental techniques have been used to determine the microstructure properties that not only quantify each alloy but also influence their fracture toughness.

3.2 TUNGSTEN CARBIDE GRADES INVESTIGATED

Thirty-six tungsten carbide grades have been investigated. The powders from which the hard metal grades were made, were produced by four different powder manufacturers. Three of the manufacturers use the conventional methods of ball milling powder production, whereas the fourth manufacturer uses the spray conversion process to make its powders. Both production methods were reviewed in chapter 2. Table 3.1. shows the nominal alloy composition of the various WC grades used. The first letter used for the grade designation describes the tungsten carbide particle size distribution in the sintered metal and the second letter represents the name of the powder manufacturer. The WC particle distribution letters are explained as follows:

U $\Rightarrow$ ultrafine having WC grain sizes in the range 0.3-0.5μm
F $\Rightarrow$ fine having WC grain sizes > 0.5μm, but less than 1μm
M $\Rightarrow$ medium having WC grain sizes $\geq$ 1μm but less than 3μm
C $\Rightarrow$ coarse having WC grain sizes $\geq$ 3μm

Table 3.1 *Nominal alloy compositions for the WC-Co hard metals.*

Grade designation	*wt% VC*	*wt% Co*			
UD	0.4	6	8	10	15
UD	0.8	6	8	10	15
UN	0.4	6	8	10	15
UN	0.8	6	8	10	15
US	0.4	6	8	10	15
US	0.8	6	8	10	15
FB	0.2	6	8	10	15
MB	-	6	8	10	15
CB	-	6	8	10	15

The different manufacturers produce WC powders with or without the addition of alloying powders. Manufacturer D produces WC powder with a powder grain size of 0.4μm to which cobalt and vanadium carbide powders were added during laboratory milling at Boart Longyear Research Centre. The cobalt powder added has a grain size of approximately 1.4μm and the vanadium carbide powder 1μm.

The powders produced by manufacturer N have the respective cobalt contents added. These powders have a grain size range between 0.2-0.5μm. The VC is added during further milling. Manufacturer S produces WC powders that include the respective VC contents. The respective cobalt contents were added during subsequent processing. Hard metal grades FB, MB and CB were produced by manufacturer B. Cobalt and vanadium powders are added during milling.

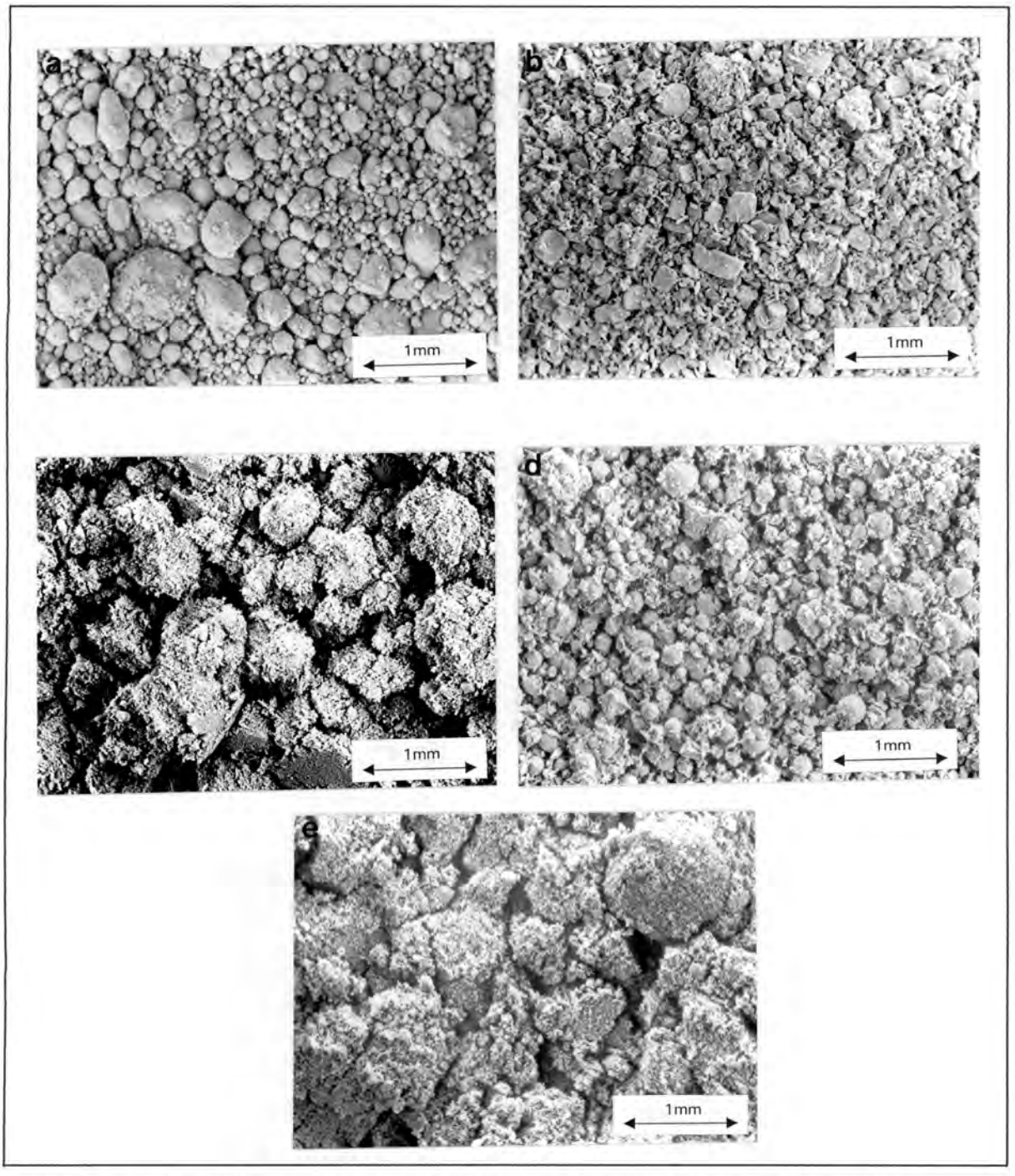

Figure 3.1 *SEM micrographs showing the powders used to manufacture the cemented carbides.*

(a) Cobalt Powder

(b) Vanadium carbide powder

(c) D powder

(d) N powder

(e) S Powder

All thirty-six grades of hard metal were produced under similar laboratory conditions using a 1kg-attritor mill. Exactly 1kg of powder was used for each milling process. A homogenous powder mixture was ensured by ball milling for five hours using hexane as a solvent. The balls were 4mm diameter WC and the ball charge rate was 8:1, which implies that during the milling operation, the mass of the balls is 8 times greater than that of the powder charge rate. A paddle speed of 300rpm was used for the mixing. After the 5 hours of milling, 2wt% paraffin wax, dissolved in hexane was added to the mill pot and the milling continued for a further 1 hour.

The milled powder mixture, together with the balls, was dried in a vacuum at 75°C for one and half-hours. Thereafter, the mixture was screened and granulated for ease of pressing into the required shape. A screen size fraction of 90 to 350 microns was used for this purpose.

The powder was subsequently compacted using a 100 ton Danish Industries Hydraulic compacting press using a pressure of ±109MPa. The die design is such that it is possible to press the test pieces in a double acting mode even though the bottom plate does not move in relation to the top plate. The test pieces were pressed into the form of cylindrical rods 14mm in length with a 10mm diameter.

After compaction, the samples were sintered in a combined sinter hip cycle. In this cycle, the specimen were sintered in a vacuum at a set temperature and time period and thereafter, high-pressure argon was introduced into the sintering chamber for a set time period. Sinter-hipping, also known as pressure assisted sintering, eliminates surface porosity and ensures that the sintered metal has a relative density of approximately 92%.

The sintering temperature, which was held for 20 minutes, is shown in table 3.2. The choice of sintering temperature is dependent on the cobalt content. Reasons for this were given in chapter 2.

Table 3.2 *Sinterhip temperature for each grade with respect to cobalt content.*

Wt% Co	*Temperature in °C*
6	1420
8	1390
10	1370
15	1350

The samples were then subjected to a pressure of 50 bars using argon gas, for 40 minutes at the sintering temperature and then cooled down to ambient. Afterwards, the samples were ground to a surface finish R_a between 0.3 – 0.5 microns.

3.3 HEAT TREATMENT

It is has been shown[21,173] that on cooling down from the sintering temperature that microscopic residual stresses are present in the hard metal. This occurs as a result of the differences in the co-efficient of thermal expansion between the phases. The thermal co-efficient of expansion of cobalt is three times that of tungsten carbide. This causes the cobalt binder to be in a state of tension and the tungsten carbide regions go into compression, thus setting up stress gradients in the hard metal. Annealing the hard metals is necessary in order to relieve these residual stresses[173].

The alloys were annealed in a Balzers Tocco Meltmaster furnace for two hours in a vacuum and then furnace cooled. A vacuum was used to prevent oxidation of the samples and the 2 hours was chosen based on suggestions by other researchers who have found that annealing for anytime less than 1 hour may be insufficient to fully relieve the stresses[132].

Various researchers[21,132] also suggested using an annealing temperature of 800°C. However, it was decided to anneal one set of hard metals at 800°C and a second set at 900°C to investigate the influence of annealing temperature on the fracture toughness values.

Thus the WC alloys were investigated under three conditions, namely:

Condition 1: As received condition
Condition 2: Annealed at 800°C for 2 hours
Condition 3: Annealed at 900°C for 2 hours

3.4 PHYSICAL PROPERTIES

It is not necessary to employ a standard sample size for the measurement of density, coercivity and magnetic saturation. The samples need only be small enough to fit inside the individual test apparatus. However, the test methods to be followed are standardized.

3.4.1 DENSITY

Density is a measure of the mass per unit volume and was carried out on each specimen using the Archimedes submersion method outlined in ASTM B311-58. This measurement gives an indication of the percentage of binder material that cements the carbide grains together with the unit of density being grams per centimeter cubed (g/cm^3). Typical values for cemented carbides range from 13-15g/cm^3.

3.4.2 MAGNETIC SATURATION

Magnetic saturation is a measure of the magnetic permeability of the metal and as the cobalt phase is the magnetic phase, this property can also be used to determine the percentage of free cobalt in the material. However, this applies only when the metal is fully magnetized and the carbon balance is precise. When there is a carbon deficiency, the free tungsten present will combine with some of the cobalt during sintering to form a carbon deficient phase. This phase is non-magnetic and results in a reduction of the measured magnetic saturation value. The test was carried out on a LDJ model SM-8100 Saturation Induction measuring system. The units of measurement are Gauss centimeter cubed per gram (Gcm^3/g). Typical values for hard metals range between 100-600 Gcm^3/g.

3.4.3 COERCIVITY

Coercivity is a measure of the force required to completely demagnetise a magnetically saturated material. The coercivity was measured using a Forster Koerzimant 1.095 machine according to the method outlined in ISO3326-1975. Coercivity is also used as a measure of the stress experienced by the cobalt during sintering. This measurement has also been used as a non-destructive method of determining the carbide grain size distribution, a method that will be described in section 3.6.

The unit of measure is the Oesterds (Oe) and typical value range from 50 to 300 Oe. The SI unit commonly used is the kA/m that is calculated by the relationship of:

$$1Oe = \frac{1}{4\pi} kA/m \qquad \text{...(3.1)}$$

3.4.4 HARDNESS

Vickers indentations were carried out on an ESE WAY semi-automatic Vickers hardness tester. An indenting load of 30kg was used for the indentations as recommended by ISO 3878. The duration of loading was 14.91 seconds for all measurements. The indentation diagonal measurements were performed using a Reichert MeF3A optical microscope at a magnification of 200X. The Vickers hardness was calculated from equation 3.2:

$$HV = \frac{1.85P}{d^2} \qquad \text{...(3.2)}$$

Where: P = indentation load (N)
D = mean diagonal of indentation (m)

The results presented in this work represent the average of at least thirty indentation measurements taken on each grade.

3.5 SHORT ROD FRACTURE TOUGHNESS TEST

3.5.1 TECHNICAL DESCRIPTION OF TERRA TEK FRACTOMETER

All short rod fracture toughness tests were performed on a Terra Tek Fractometer I machine shown in figure 3.2

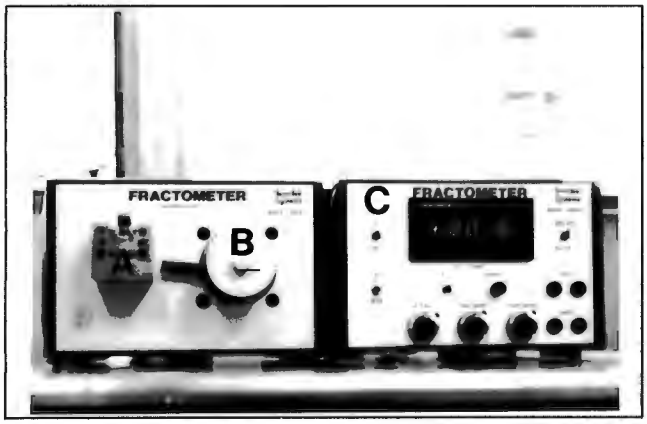

A: *Flatjack*
B: *Stress Intensity Meter*
C: *Pressure Drive System*

Figure 3.2 *The Terra Tek Fractometer I.*

The Fractometer I test system is designed to perform fracture toughness tests on brittle materials that exhibit linear elastic fracture mechanics (LEFM) behaviour. The machine can be operated both manually and automatically. The tests for this project were done using the automatic mode.

The Flatjack, shown in figure 3.2 and in figure 3.4, is an inflatable, ultra thin bladder, which is filled with mercury. Mercury is used since it has a high stiffness that assures controlled, steady crack growth during the test. Pressure is applied automatically to the mercury which causes a crack to initiate at the chevron tip shown in figure 3.3. A further increase in Flatjack pressure causes the crack to advance through the specimen in a stable growth mode.

A stress intensity meter monitors the opening load on the specimen in units of $ksi\sqrt{in}$ or $MPa\sqrt{m}$. A peak load detection circuit detects and stores the peak load, which is recalled from memory following the test procedure.

3.5.2 TEST METHOD

The samples were in the shape of cylindrical rods and the dimensions are shown in figure 3.3. A Leco cutting machine was used to saw 0.33mm wide longitudinal slots in each specimen, leaving a chevron-shaped ligament joining the two specimen halves in the intended crack plane. The thinness of the slot aid in achieving plane strain conditions at the crack front. The final specimen geometry is shown in figure 3.3.

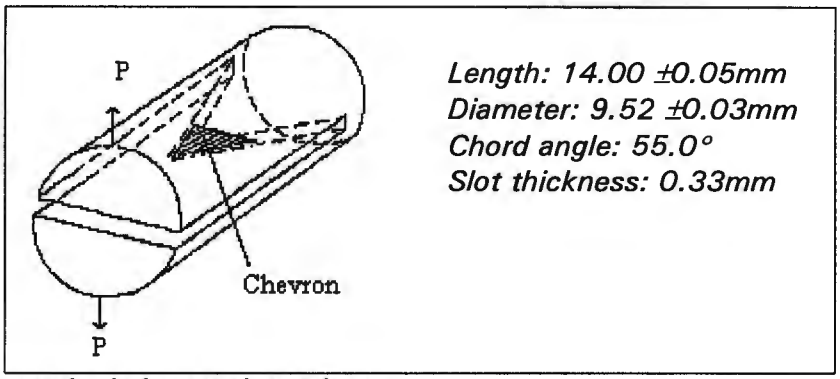

Figure 3.3 *Chevron-notched short rod specimen.*

Before testing, the open edges were beveled with a diamond file and cleaned with sewing machine oil to prevent rupture of the mercury bladder during positioning of the sample. Figure 3.4 shows the positioning of the sample on the flatjack.

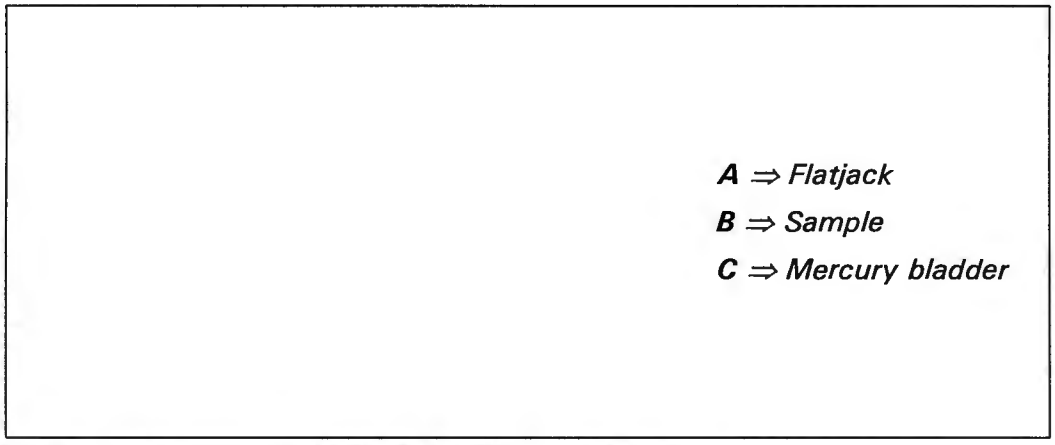

Figure 3.4 *Positioning of sample on mercury bladder.*

An opening load P, provided by the pressure in the mercury bladder, is applied to the chevron tip, causing a crack to initiate at its point. Crack growth is stable due to the constant widening of the crack front as it propagates along its axis. Thus, a real crack, also known as a 'natural' crack, is created in the specimen before the toughness measurement is made.

When the crack is in the central region of the chevron, the maximum load is recorded, which is converted automatically into a fracture toughness measurement. After the maximum load is reached, the load decreases with further crack growth, until the specimen splits in half. The test takes approximately 15 seconds. A fractured chevron of the specimen is shown in figure 3.5.

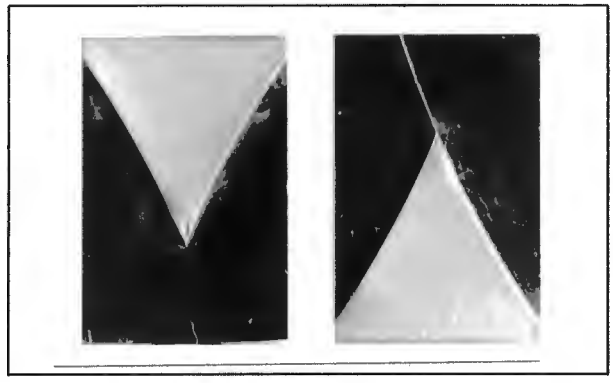

Figure 3.5 *Fractured short rod specimen halves.*

3.6 PALMQVIST FRACTURE TOUGHNESS TEST

3.6.1 PALMQVIST POLISHING PROCEDURE

The fractured short rod specimen halves were ultrasonically cleaned in alcohol and then mounted in Leco lucite powder using a Buehler Ltd, specimen mounting press. Thereafter, the specimens were ground with a Struers metal bonded 40um-diamond wheel to provide flat surfaces to facilitate polishing. This grinding took approximately 10 minutes on a Struers RotoSystem automatic polisher using a load of 30N and a wheel speed of 300 rpm and water was used as a lubricant. Both wheel and specimen turned in the same direction.

The importance of a correct polishing procedure was outlined in the chapter 2. The following polishing procedure was established using the method outlined by Exner[173] as a guideline. An automatic polishing machine was used to apply a fixed pressure of 30N onto the samples during polishing and the wheel speed was 150 rpm. Struers DP-Lubricant Blue was used as the lubricant throughout the polishing procedure. The diamond suspensions and polishing pads that were used are also by Struers. After, the specimen were ground on the 40um grinding disc, the following procedure was carried out in order to determine the point at which a constant, maximum crack length is obtained in each grade.

- Procedure used

1. The sample was indented with a Vickers diamond indentor using loads of 20, 30, and 50kg. Three indents per load were made on each sample.
2. The indent diagonals and the crack lengths extending from the corners of each indent were measured using an optical microscope at a magnification of 120 times. The crack lengths were measured from the end of the indent to the end of the crack as shown in figure 3.6.

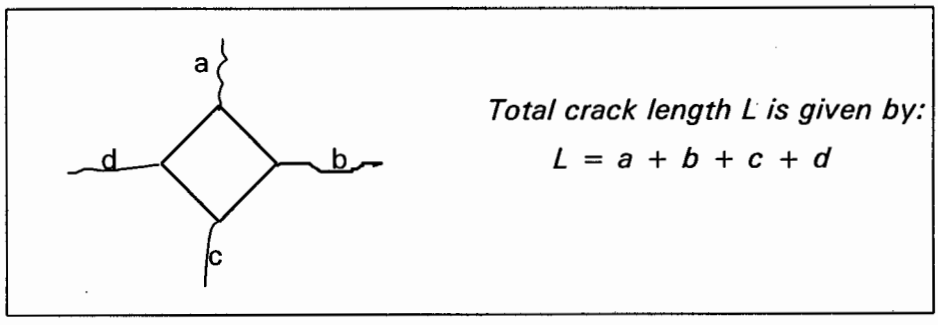

Figure 3.6 *Vickers indentation with the cracks emanating from the indent corners.*

The cracks did not always originate from the apex of the indent.

3. The sample was then polished for 1-minute using 9μm diamond suspension and cleaned ultrasonically in alcohol.
4. The diagonals of the indents made in step 2 were again measured, to determine the amount of material removed after one minute of polishing using equation 3.3.

5. Steps 1 to 4 were repeated until a constant, maximum crack length was obtained. A new layer of diamond suspension was always applied on the polishing cloth.
6. Steps 1 to 5 were repeated using 0.25μm diamond suspension.

The two different grades of diamond suspension were used to compare their effect, if any, on the crack lengths produced. Equation 3.2, developed by Exner[173], was used to calculate the thickness of the layer removed after each polishing step:

$$A = \frac{D_1 - D_2}{2}.\cot\frac{\alpha}{2} \qquad \text{...(3.3)}$$

Where: A $\Rightarrow$ thickness of layer removed

$D_{1/2} \Rightarrow$ diagonals of the Vickers indentation before and after polishing;

$\alpha \Rightarrow$ angle between the faces on the top of the Vickers pyramid (136°).

After the maximum crack length was reached, ten indentations were made per load on each sample using the three different loads. The crack lengths were measured according to step 2 above and these total crack lengths were used to determine the Palmqvist toughness and the Palmqvist fracture toughness.

3.6.2 THE PALMQVIST TOUGHNESS (W)

The Palmqvist toughness, which is a measure of the material's resistance to crack initiation and propagation, was calculated using equation 3.4 developed by S Palmqvist in 1957[1]:

$$W = \frac{P}{Li} \qquad \text{...(3.4)}$$

Where: $W \Rightarrow$ Palmqvist toughness (N/m)

$P \Rightarrow$ Applied load (N)

$L_i \Rightarrow$ Total crack length (m)

3.6.3 THE PALMQVIST FRACTURE TOUGHNESS (K_{Ic})

The Palmqvist fracture toughness was calculated using equation 3.5 developed by Shetty et al (1985)[3]:

$$K_{IC} = 0.0889\sqrt{\frac{H.P}{Li}} \qquad \text{...(3.5)}$$

Where:

$H \Rightarrow$ Vickers hardness (Nm^{-2})

$P \Rightarrow$ Indent load (N)

$L_i \Rightarrow$ Total crack length (m)

3.7 MICROSTRUCTURE ANALYSIS

3.7.1 POROSITY AND FREE CARBON

Pores can act as fracture initiation points and stress raisers, making the extent of their presence important to the value of the fracture toughness of a material. Therefore, following Palmqvist testing, the samples were ultrasonically cleaned in alcohol, dried and examined using optical microscopy. ASTM specification B276-54 was used to assess the porosity and free carbon with respect to presence, type and distribution.

The pore type was identified as either A-type or B-type depending on the pore size. A-type pores have a pore diameter less than 10μm and B-type pores have pore diameters from 10μm to 40μm. It is possible to observe pores with pore diameters greater than 40μm, but none were found in the specimens examined during this work. The pore distribution, within each pore type, was matched with photomicrographs given in the ASTM specification and when a match was found, the designation given below the photomicrograph was assigned to the specimen.

The presence of free carbon was also recorded by also matching the specimen microstructure to photomicrographs given in the specification and would be designated C-0, C-1, C-2, up to C-6, with C-0 meaning no free carbon was

observed and C-6 would represent the maximum amount of free carbon distribution present.

3.7.2 COBALT VOLUME FRACTION (V_{Co})

The cobalt volume fraction was determined using equation 3.6:

$$V_{Co} = \left(\frac{X_{Co}}{8}\right)\left(\frac{\rho_{th}}{100}\right) \qquad \text{...(3.6)}$$

Where: $X_{Co} \Rightarrow$ weight percentage of Co

$\rho_{th} \Rightarrow$ density of composition

3.7.3 WC GRAIN SIZE (dwc)

There is no standardised method for measuring the carbide grain size, although empirical equations using coercivity have been devised. The most common method of determining grain size measurements for various materials is by etching a cross-section of a material and using metallographic techniques, such as the linear intercept method, to obtain a value. However, for the ultrafine grades used in this research work, this method proved to be impossible due to the small size of the grains which could not be resolved in the microscope.

An attempt was made to measure the grain size by etching the fracture surfaces of the samples after short rod testing. The fractured samples were left in HCl acid for four weeks in an attempt to remove the cobalt from the surface layers. The fracture surfaces were then observed using electron microscopy at a magnification of 40 000 times and the average grain size estimated.

In order to provide a comparison with the estimated grain sizes, three equations developed by three different sets of researchers were also used to calculate the carbide grain size. These equations make use of the coercivity values of the material and two of them include the cobalt volume fraction.

The following equations were used, with V_{Co} representing the cobalt volume fraction and K representing the coercivity in kAm^{-1} in equations 3.7, 3.9 and 3.10, while the coercivity value in equation 3.8 is in oesterds.

Porat & Malek[130]:

$$d_{WC} = 0.3\left(\frac{80}{K}\right)^{0.57(1/V_{Co})^{1/3}} \qquad \text{...(3.7)}$$

Fang & Eason[119]:

$$d_{WC} = 73(1 - 1.03\exp[-5V_{Co}])\left(\frac{1-V_{Co}}{KV_{Co}}\right) \qquad \text{...(3.8)}$$

Roebuck[132]:

$$d_{WC} = \frac{7.93}{K - 6.71} \qquad \text{for K > 12.5kAm}^{-1} \qquad \text{...(3.9)}$$

$$d_{WC} = \frac{10.9}{K - 1.79} \qquad \text{for K < 12.5kAm}^{-1} \qquad \text{...(3.10)}$$

Porat and Malek[130] derived their equation from a graph of carbide grain size plotted against coercivity. The carbide grain sizes had been determined by lineal analysis of 26 grades of cemented carbides. The grain size range was between 1μm and 8μm. Fang and Eason[119] derived their equation by combining three equations namely:

- $H_C = \frac{73}{\lambda}$

  which is an equation developed by Fischmeister and Exner[94] who showed, through graphical data, that the coercivity(Hc) is inversely proportional to the mean free path through the cobalt phase.

- $L_{WC} = \lambda(1 - C)\left(\frac{1-V_{Co}}{V_{Co}}\right)$

  is an equation developed by Exner[17] where C is the contiguity of the material and Lwc is the mean linear carbide grain size.

- $C = 1 - 1.03\exp(-5V_{Co})$

is an equation developed by Fang and Eason[119] from experimental data complied by Exner[17].

Roebuck[132] derived his equations from graphic plots of coercivity versus carbide grain size, where the grain sizes were obtained from lineal analysis of fifty cemented carbides. The grain size range was between 0.28 and 3.26μm.

3.7.4 BINDER MEAN FREE PATH (λ)

The binder mean free path (λ) was determined using equation 3.11 developed by Underwood[187]:

$$\lambda = d_{WC}\left(\frac{V_{Co}}{1-V_{Co}}\right) \qquad \text{...(3.11)}$$

Where: $d_{WC} \Rightarrow$ WC grain size

$V_{Co} \Rightarrow$ cobalt volume fraction

Each of the four grain sizes obtained by equations 3.7, 3.8, 3.9 and 3.10, as well as the estimated grain size for each hard metal grade were used to determine the mean free path values for each grade.

3.7.5 MICROSTRUCTURE DEFECTS

3.7.5.1 Cobalt pooling

The polished specimens were rinsed in distilled water, dried and examined using light microscopy at a various magnifications to detect the presence and extent of cobalt pooling. Cobalt pooling arises due to insufficient mixing during milling.

3.7.5.2 Eta(W_3C) Phase

The polished samples were etched for 30 seconds using Murakami's etchant. The time is sufficient for the eta phase to be clearly visible, if present, in the form of black patches. Light microscopy at a magnification of 200 times was used to detect the presence of eta phase.

3.7.5.3 Discontinuous grain growth

This kind of grain growth defines exaggerated carbide crystal growth in comparison to the rest of the microstructure in the form of W_3C crystals. While noting the presence of eta phase, the presence of discontinuous grain growth was also noted. The distribution of the types of grain growth was described as either isolated, single crystals or clusters of many crystals.

3.8 FRACTOGRAPHY

The fracture surfaces of the samples following short rod testing were examined using a Cambridge 440 scanning electron microscope at a magnification of 15 000 times. Differences amongst the grades were recorded, as was the nature of the fracture. Smearing of the grains as well as the presence of holes was also noted.

Fracture surfaces were etched in an attempt to distinguish between fracture markings that could be characteristic to the two material phases. To examine the carbide features the surfaces were etched using 32%HCl acid and then to observe the cobalt features, the surfaces were etched using 80%KOH. It proved to be quite difficult to observe the fracture markings of the ultrafine grades due to the fine nature of the microstructure.

Additionally, the polished specimens were etched in concentrated 32%HCl acid, which etches the cobalt, for 10 hours and then examined using the electron microscope to observe the nature of the cracks extending from the corners of the hardness indents. An attempt was also made to identify whether the crack paths were intergranular or transgranular and to note if any interfacial carbide cracking had occurred.

Chapter 4

RESULTS: MATERIAL CHARACTERISATION

4.1 INTRODUCTION

This chapter sets out the material characterisation results for each grade of hard metal investigated. The hard metals were characterised with respect to:

(a) density
(b) magnetic saturation
(c) the presence of microstructural defects
(d) Vickers hardness
(e) coercivity
(f) carbide grain size
(g) cobalt volume fraction
(h) binder mean free path

The influence of cobalt content and grain growth inhibitor on these properties are discussed. Comparisons are also drawn between the ultrafine grades made via the three different powder routes. Finally, the ultrafine grades are compared to the conventional hard metals with respect to these properties.

4.2 DENSITY

The results of the density tests for the hard metals are given in Table 4.1.

Table 4.1 *Densities for the various hard metals.*

Grade	Density	*Grade*	Density	*Grade*	Density
UD64	14.90	*UN64*	14.83	*US64*	14.84
UD84	14.60	*UN84*	14.67	*US84*	14.67
UD104	14.43	*UN104*	14.42	*US104*	14.43
UD154	13.90	*UN154*	13.89	*US154*	13.94
UD68	14.76	*UN68*	14.74	*US68*	14.70
UD88	14.51	*UN88*	14.49	*US88*	14.54
UD108	14.28	*UN108*	14.26	*US108*	14.32
UD158	13.87	*UN158*	13.82	*US158*	13.81
FB62	14.91	*MB6*	14.95	*CB6*	14.95
FB82	14.68	*MB8*	14.74	*CB8*	14.75
FB102	14.50	*MB10*	14.52	*CB10*	14.55
FB152	14.01	*MB15*	14.03	*CB15*	14.05

Through comparison of the data in table 4.1, it can be seen that the measured densities of the hard metals correlate well with the theoretical densities of WC-Co alloys that are listed in Table 4.2. One of the essential differences between the theoretical and experimental values is that the theoretical determination does not take into account the presence of porosity or free carbon, which decreases the density, nor the presence of eta phase which causes the density to increase.

Table 4.2 *Theoretical density of WC-Co, based on densities of 15.77g/cm^3, 8.9g/cm^3 and 5.77g/cm^3 for WC, Co and VC respectively.*

wt% Co	Theoretical Density in g/cm^3			
	0wt%VC	*0.2wt% VC*	*0.4wt% VC*	*0.8wt% VC*
6	14.95	14.90	14.85	14.76
8	14.74	14.69	14.64	14.55
10	14.53	14.49	14.44	14.30
15	14.04	13.99	13.95	13.82

Figure 4.1 shows the scatter of the density data for the grades with respect to cobalt content which shows that an increase in cobalt content is associated with a decrease in density. It is noticeable that as the tungsten carbide grain size decreases, the sample also density decreases for a given cobalt content. The densities of grades UD64 and US84 are higher than the theoretical densities and may contain eta phase. Grades UN154, UN88 and US68 show densities that are lower than the theoretical values and one would expect to find free carbon in these samples.

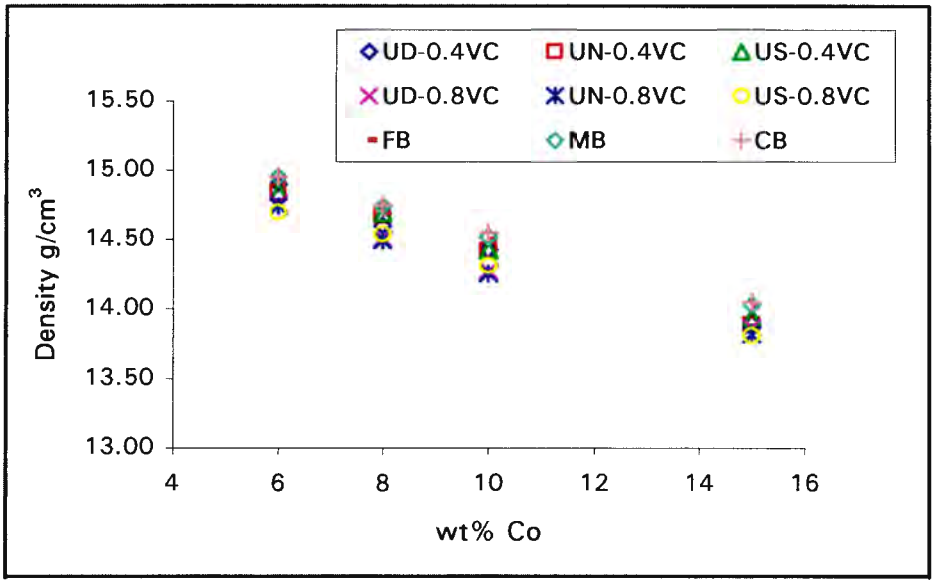

Figure 4.1 *The influence of cobalt content on the hard metal's density.*

4.3 MAGNETIC SATURATION

Tables 4.3, 4.4 and 4.5 show the magnetic saturation data for the hard metals. The magnetic saturation measurements are expressed in three forms: the magnetic saturation of the composite, the normalised magnetic saturation of the binder phase (calculated using the nominal binder content of the composite) and the magnetic saturation of the binder phase of the alloys expressed as a percentage to that of pure cobalt which is 160 Gcm^3/g.

Table 4.3 *Magnetic saturation measurements for the 0.4%VC ultrafine hard metals.*

Grade	Magnetic Saturation $4\pi\sigma$	Normalised MS Gcm^3/g	MS relative to pure Co (%)
UD64	84 ±2	1400	70
UD84	136 ±1	1700	85
UD104	170 ±1	1700	85
UD154	269 ±1	1793	90
UN64	109 ±1	1817	91
UN84	136 ±2	1700	85
UN104	182 ±1	1820	91
UN154	275 ±1	1833	92
US64	106 ±2	1767	88
US84	118 ±1	1475	74
US104	170 ±1	1700	85
US154	259 ±1	1727	86

Table 4.4 *Magnetic saturation measurements for the 0.8%VC ultrafine hard metals.*

Grade	Magnetic Saturation $4\pi\sigma$	Normalised MS Gcm^3/g	MS relative to pure Co (%)
UD68	106 ±1	1767	88
UD88	146 ±1	1825	91
UD108	178 ±1	1780	89
UD158	274 ±3	1827	91
UN68	108 ±1	1800	90
UN88	141 ±2	1763	88
UN108	183 ±2	1830	92
UN158	281 ±1	1873	94
US68	103 ±1	1717	86
US88	147 ±1	1838	92
US108	176 ±1	1760	88
US158	268 ±2	1787	89

Table 4.5 *Magnetic saturation measurements for the conventional hard metals.*

Grade	Magnetic Saturation $4\pi\sigma$	Normalised MS Gcm^3/g	MS relative to pure Co (%)
FB62	110 ±1	1833	92
FB82	138 ±2	1725	86
FB102	170 ±1	1700	85
FB152	281 ±1	1873	94
MB6	110 ±1	1833	92
MB8	138 ±1	1725	86
MB10	184 ±1	1840	92
MB15	260 ±1	1733	87
CB6	105 ±1	1750	88
CB8	138 ±1	1725	86
CB10	190 ±2	1900	95
CB15	260 ±2	1733	87

The normalised magnetic saturation of the binder phase can be seen to vary in general between 1700 and 1900 Gcm^3/g. This represents between 85 and 95% of the specific magnetic saturation of pure cobalt. These values lie within the WC+β region of the WC-Co phase diagram, indicating that the presence of a third phase is unlikely and represent the range of the hardmetals most commonly used by hardmetal manufacturers.

It has been reported[120] that when the specific magnetic saturation of the binder phase is less than 78% of that of pure cobalt, then the formation of the eta phase is most likely. Grades UD64 and US84 for which the specific magnetic saturation of the binder phase is respectively 70 and 74%, are expected to contain regions of eta phase. These grades were not rejected so that their influence on the fracture toughness would be noted.

Eta phase forms when the metal is carbon deficient. Due to the shortage of carbon, tungsten will combine with some of the cobalt during the sintering cycle and will form this eta phase, which is non-magnetic and results in a decrease in the values of the specific magnetic saturation. Depending of the morphology of the eta phase present it may cause embrittlement of the material and can lower its fracture toughness.

The 0.8wt% vanadium carbide alloys show 2 to 3% higher specific magnetic saturation values than the 0.4wt% vanadium carbide alloys. This arises probably because the vanadium carbide depresses the amount of tungsten in the cobalt binder.

4.4 THE PRESENCE OF DEFECTS

4.4.1 POROSITY

Pores are difficult to avoid during the production of the hard metals even when the correct carbon balance is maintained. Thus, a uniformly distributed residual porosity is usually present and is commonly accepted as not being harmful. Optical electron examinations of the polished specimen surfaces showed the porosity levels of the majority of the grades to be <A02 B00 according to ASTM standards. This indicates that the maximum pore diameters were less than 10 microns and the porosity constituted less than 0.02 volume %.

4.4.2 FREE CARBON

Free carbon also known as carbon porosity or graphite, forms in the presence of excess carbon. Optical electron examinations of the polished specimen surfaces showed the porosity levels of the majority of the grades to be <C00 according to ASTM standards. Noteable exceptions to this were grades UN154, UN88 and US68, which was expected due to their low density values shown in table 4.1. Figure 4.2 shows the extensive distribution of free carbon in grade UN154. This type of carbon porosity is evidence of either an inferior milling technique or a substandard de-waxing procedure.

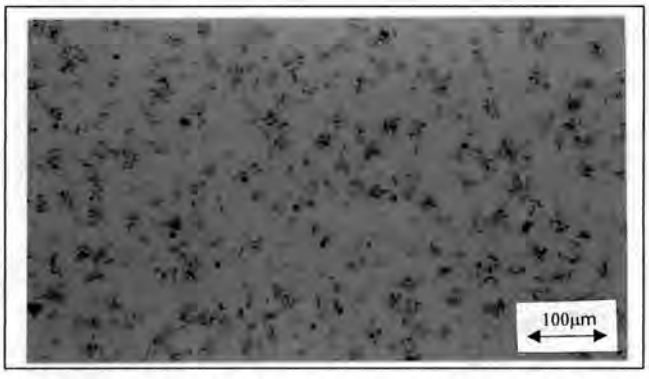

Figure 4.2 *Bright field micrograph showing extensive distribution of free carbon in alloy UN154 due to substandard de-waxing procedure.*

Figure 4.3 shows the free carbon distribution found in grade US68. This type of free carbon can occur from the presence of wax-flecks after the milling procedure. These flecks "burn-out" during the pre-sintering stage, leaving behind these "slits" of graphite, which will not "heal" during final sintering. These "slits" may also be "pressing-crack" which form during compaction.

Figure 4.3 *Bright field micrograph of grade US68 showing "slits" of graphite formations possibly due to the presence of wax-flecks after milling.*

4.4.3 ETA PHASE

The eta phase is formed during sintering, when there is a carbon deficiency in the metal. Its formation is a nucleation and growth process. Growth of the eta phase is controlled by the diffusion of carbon over large distances in the hardmetal matrix at the sintering temperature. The precipitation of the eta phase occurs usually in concentrated patches which displace a considerable area of the matrix, resulting in a reduction of the effective contribution of WC to the strength of the composite.

After a 30 second etch using Murakamis Reagent, regions of the eta phase were found on grades UD64 and US84. This was expected due to their low values of specific magnetic saturation and high density values. Figure 4.4 illustrates the eta phase found in grade US84

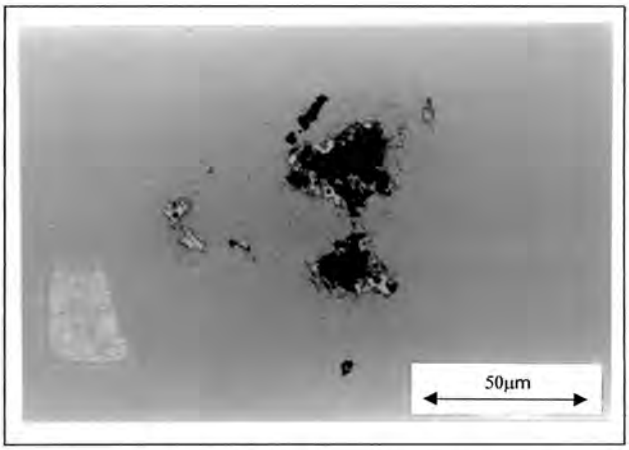

Figure 4.4 *Bright field micrograph showing typical eta phase formations found in US84.*

The hardness of the eta-carbide is intermediate between that of the tungsten carbide and the binder. Eta phase will lead to an increase in the alloy hardness only if it is present in small amounts and is well dispersed.

4.4.4 DISCONTINUOUS GRAIN GROWTH

Discontinuous grain growth is also known as non-uniform grain growth and constitutes one of the principle problems in ultrafine alloy manufacture. This growth type is usually more pronounced in the case of low cobalt alloys (6wt%) than in the case of high cobalt alloys (>10wt%). Different modes of grain growth can be observed in the sintering of the alloys and figure 4.5 illustrates two types that were observed in grades UD108 and MB6, namely, single isolated carbide grains and clusters of carbide grains.

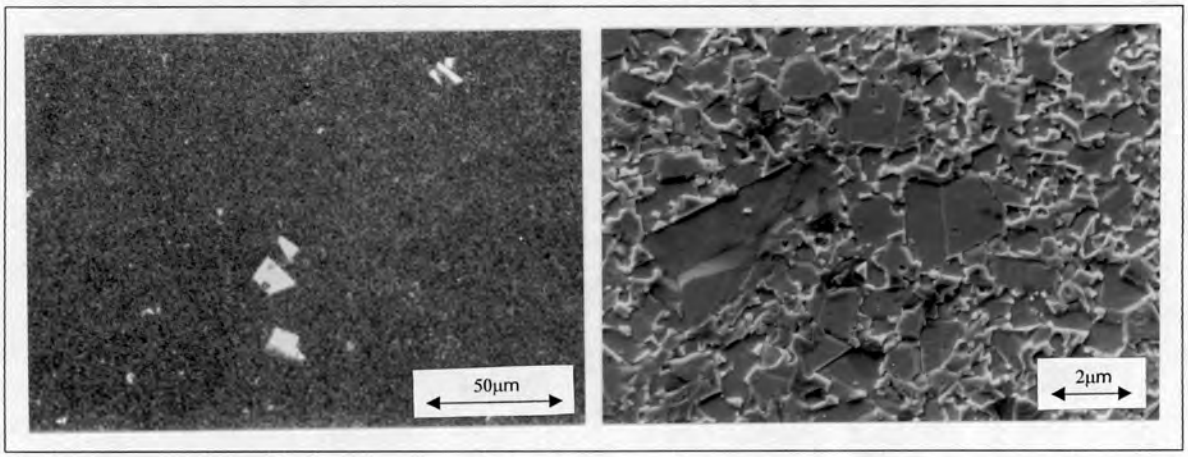

Figure 4.5 *Bright field(left) and SEM(right) micrographs showing exaggerated carbide grain growth in grades UD108(left) and MB6(right).*

This growth was probably caused either by chemical or geometrical irregularities in the green powder compact. A secondary reason could be that insufficient amounts of grain growth inhibitor were added or that the inhibitor was not evenly distributed during milling of the powder. A third reason is the possibility of contamination by coarser-grained powders during processing. These larger grains will act as seeds for discontinuous grain growth.

4.4.4 COBALT POOLS

Cobalt pools are formed when the milling procedure is inhomogeneous. This inhomogeneous microstructure is caused by a poor cobalt/grain growth inhibitor distribution, as well as partially de-agglomerated tungsten carbide powder in the formulated composition. Long milling times can also lead to the formation of

cobalt flecks. Examination of the specimens showed that grade **UN64** displayed extensive cobalt pooling as is illustrated in figure **4.6**. It was decided to reject this grade and have it remade, since the level of cobalt pools detected were deemed unacceptable.

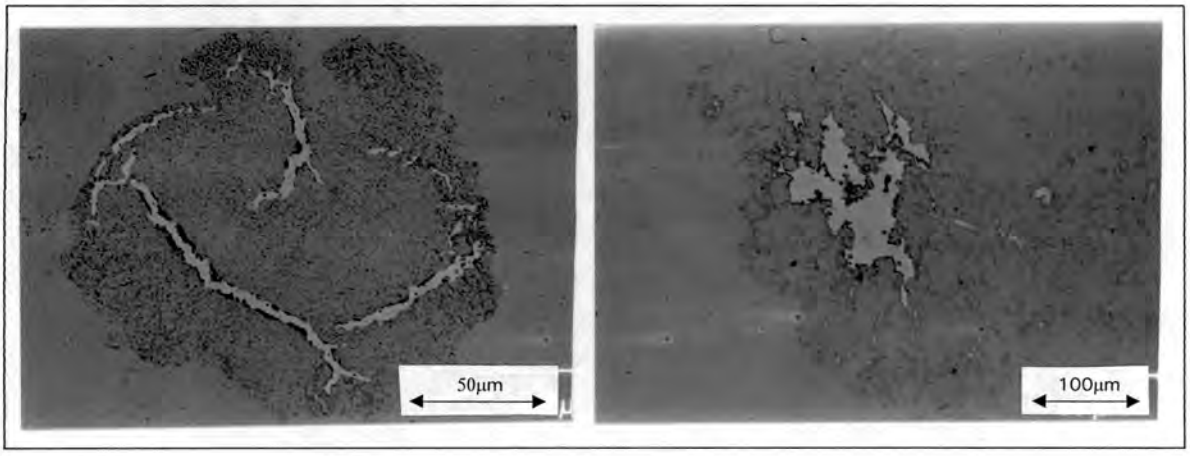

Figure 4.6 *Bright field micrographs showing two types of cobalt pools observed in UN64.*

4.5 VICKERS HARDNESS

The average hardness values for the cemented carbide specimen are listed in table **4.6**. This average was calculated using indenting loads of **20**, **30** and **50**kg and at least thirty indents per load were made on each grade. The hardness values of the annealed ultrafine specimen were found to be similar to those of the as-received specimen and these measurements were included in the calculation of the average values shown in the following tables. The tables of hardness measurements taken for each ultrafine grade at each load and in each annealed condition are listed in Appendix A.

Table 4.6 *Hardness data for the WC-Co alloys.*

Grade	Hardness Kg/mm²	Grade	Hardness Kg/mm²	Grade	Hardness Kg/mm²
UD64	1987 ±5	***UD68***	2164 ±17	***FB62***	1764 ±5
UD84	1869 ±2	***UD88***	2020 ±13	***FB82***	1711 ±7
UD104	1761 ±9	***UD108***	1910 ±5	***FB102***	1607 ±12
UD154	1526 ±12	***UD158***	1570 ±70	***FB152***	1364 ±10
UN64	1932 ±2	***UN68***	2108 ±3	***MB6***	1557 ±6
UN84	1840 ±3	***UN88***	1995 ±3	***MB8***	1526 ±11
UN104	1732 ±5	***UN108***	1869 ±6	***MB10***	1404 ±10
UN154	1529 ±2	***UN158***	1612 ±3	***MB15***	1163 ±11
US64	1885 ±3	***US68***	2152 ±10	***CB6***	1255 ±9
US84	1825 ±2	***US88***	2033 ±2	***CB8***	1244 ±7
US104	1713 ±3	***US108***	1888 ±3	***CB10***	1201 ±10
US154	1494 ±3	***US158***	1655 ±3	***CB15***	1012 ±13

An expected trend of increasing hardness with a decrease in the cobalt content is observed in all the grades. There is a larger scatter in the data of the conventional alloys compared to the 0.4wt% vanadium carbide alloys which show the least deviations. It is also noticeable that the ultrafine alloys display much higher hardnesses compared to the other alloys. This trend is clearly shown in figure 4.7 where the 0.8wt% vanadium carbide UD hardness values are plotted against those of the conventional grades.

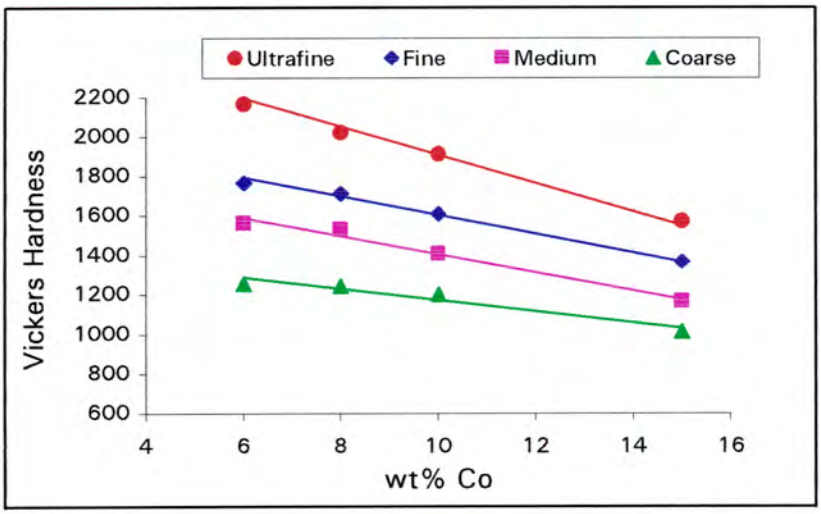

Figure 4.7 *The influence of cobalt content on the hardness of alloys with different carbide grain size distributions.*

From figure 4.7 the superior hardness of the ultrafine alloys is clear. This increase in hardness, which increases the wear resistance of the metal is one of the major reasons why emphasis is being placed on the production of fine grained metal powders. Even with a cobalt content of 15wt%, the UD grade has a hardness of 1570 Vickers, which is higher than all the other grades except the 6, 8 and 10wt% cobalt FB grades which have a hardness range of 1707-1764 Vickers.

The slopes of the three conventional grades show a limited range of attainable hardness values for hard metals containing 6 to 15wt% cobalt. The maximum difference in hardness with the coarser grained CB grades is 243 Vickers. The ultrafine grades however display a hardness range of 600 Vickers which is more than double the value of the CB grades over the same cobalt range. This is yet another desirable feature of finer grained metal products.

It is worth noting that as the vanadium carbide content is increased, the hardness also increases. This is due to the grain refinement brought about by the vanadium carbide and as shown in figure 4.7, finer grained materials have higher hardness values. This effect of vanadium carbide on the carbide grain size is shown in figure 4.8 while figure 4.9 compares the hardness values for metals containing 6wt% cobalt and varying amounts of vanadium carbide. The values shown in figure 4.8 represent the respective carbide grain sizes. Figure 4.8 shows that the carbide grain sizes are kept below 1 micron with the addition of the vanadium carbide.

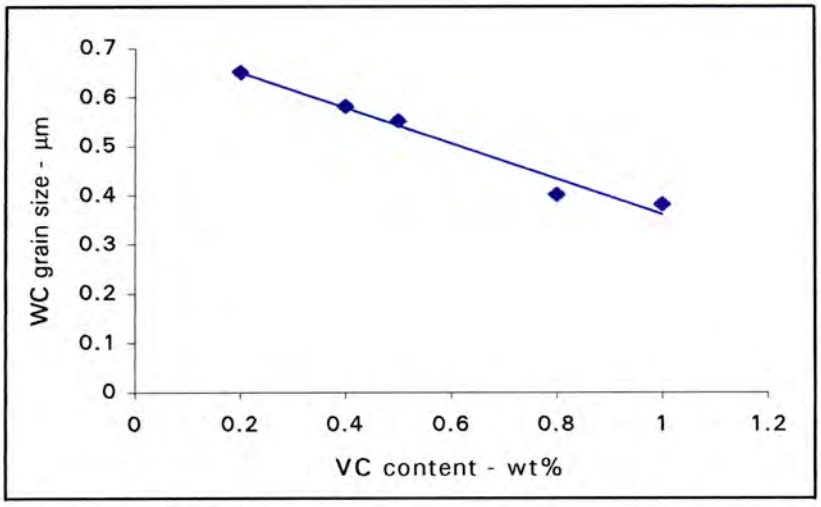

Figure 4.8 *The influence of vanadium carbide content on the carbide grain size*[188].

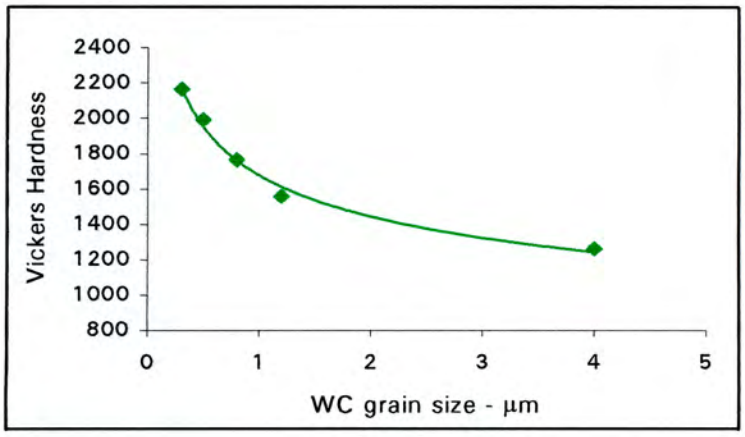

Figure 4.9 *The influence of tungsten carbide grain size on the hardness of a series of 6wt% cobalt alloys containing varying amounts of vanadium carbide.*

Figure 4.9 illustrates the sharp increase in hardness achieved when a grain growth inhibitor is added to the metal. Prior to grain refinement techniques, hard metals could only attain hardness values up to approximately ±1800 Vickers. This was achieved with additions of titanium carbide and tantalum carbide. Now, with grain refinement, hardness values in excess of 2000 Vickers can be obtained using additions of vanadium carbide and chromium carbide. It should be noted that additions of vanadium carbide keep the carbide grain size below 1µm which results in an increase in the hardness of the materials.

Regardless of the method of powder production it was found that ultrafine grades with similar binder contents displayed similar hardness values. No one type showed a clear superior hardness above the next. Figures 4.10 and 4.11 show the comparison of the hardness data for the respective 0.4 and 0.8wt%VC ultrafine alloys.

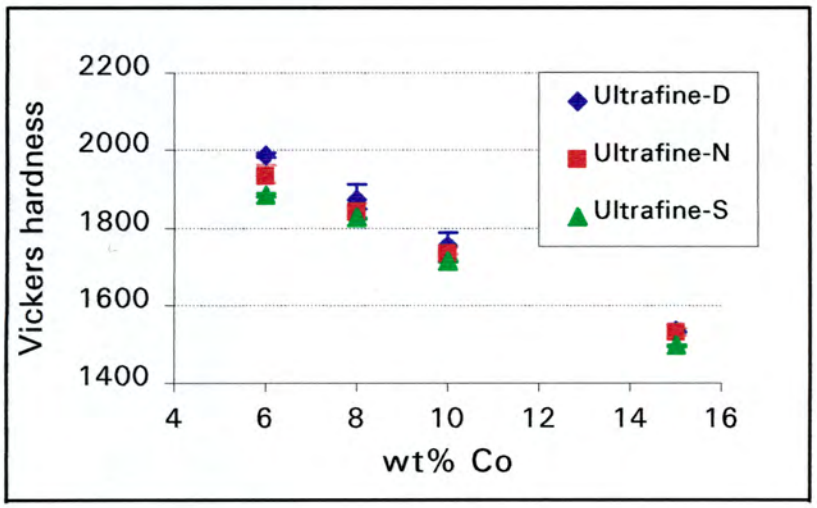

Figure 4.10 *Comparison of the hardness of the 0.4wt% vanadium carbide ultrafine alloys.*

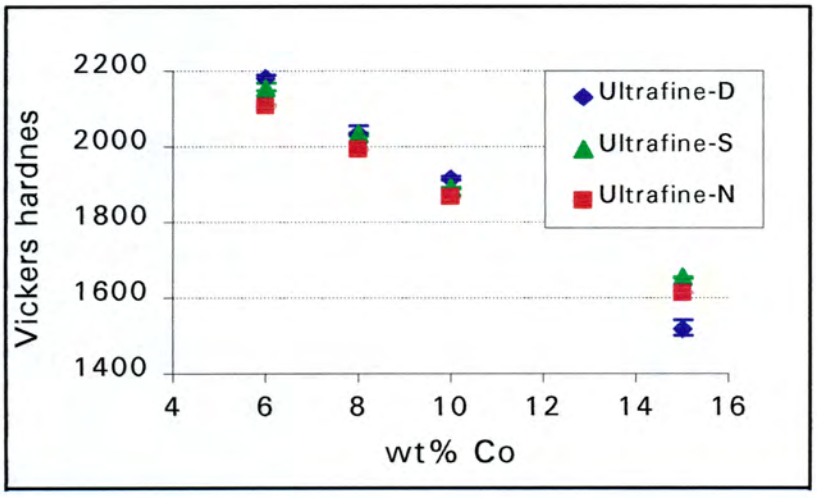

Figure 4.11 *Comparison of the hardness of the 0.8wt% vanadium carbide ultrafine alloys.*

The 0.8wt%VC grades display higher hardness values than the 0.4wt% alloys. In both figures the UN grades show the smallest scatter in data while the UD grades show the highest. Across the cobalt range the UD grades show higher hardness values than the UN and US grades. The only exception is noted for the UD158 grade that has a lower hardness than its counterparts with the same cobalt content. The UN alloys are harder than the US 0.4wt%VC grades while for the 0.8wt%VC grades, the opposite is observed.

4.6 COERCIVITY

Table 4.7 shows the coercivity data for the various grades in units of oersteds (measurement unit of test apparatus) and in the S.I. units of kAm^{-1}.

Table 4.7 *Coercivity results for the tungsten carbide hard metals.*

Grade	Coercivity		Grade	Coercivity	
	Oe	kAm^{-1}		Oe	kAm^{-1}
UD64	740 ±2	58.87	***UD68***	770 ±1	61.26
UD84	520 ±2	41.37	***UD88***	590 ±1	46.94
UD104	470 ±1	37.39	***UD108***	550 ±1	43.75
UD154	280 ±3	22.28	***UD158***	410 ±2	32.62
UN64	555 ±2	44.15	***UN68***	650 ±1	51.71
UN84	400 ±1	31.82	***UN88***	640 ±1	50.91
UN104	370 ±1	29.44	***UN108***	540 ±1	42.96
UN154	310 ±1	24.66	***UN158***	355 ±1	28.24
US64	520 ±3	41.37	***US68***	650 ±1	51.71
US84	390 ±1	31.03	***US88***	560 ±1	44.55
US104	280 ±1	22.28	***US108***	530 ±2	42.16
US154	240 ±2	19.09	***US158***	370 ±2	29.44
FB62	300 ±1	23.87	***MB6***	175 ±2	13.92
FB82	285 ±1	22.67	***MB8***	159 ±1	12.65
FB102	255 ±2	20.29	***MB10***	150 ±1	11.93
FB152	159 ±1	12.65	***MB15***	95 ±1	7.56
CB6	102 ±1	8.11	***CB10***	75 ±1	5.97
CB8	90 ±4	7.16	***CB15***	60 ±1	4.77

The coercivity values in general decrease with an increase in cobalt content for similar grained hardmetals. The ultrafine alloys display higher values of coercivity than the conventional grades. This trend is clearly illustrated in figure 4.12 which compares the coercivity data for the conventional grades to that of the 0.8wt% vanadium carbide US grades. A $20kAm^{-1}$ difference separates the ultrafine alloys from the other grades. It is also noticeable that the slope of the ultrafine grade is steeper than the slopes of the conventional alloys indicating that a wider range of coercivity values can be obtained with finer grained hard metals.

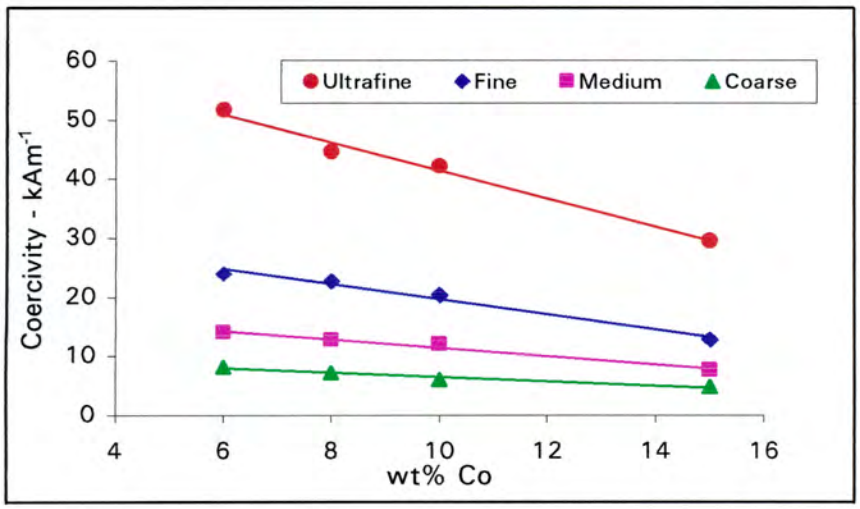

Figure 4.12 *Comparison of the coercivity data for the alloys with varying carbide grain size distributions.*

From figure 4.12 it can be deduced that the finer the carbide grain size, the higher the coercivity value. This relationship between the carbide grain size and coercivity is shown to be exponential in figure 4.13 resulting in a steep increase in the coercivity with a decrease in the grain size.

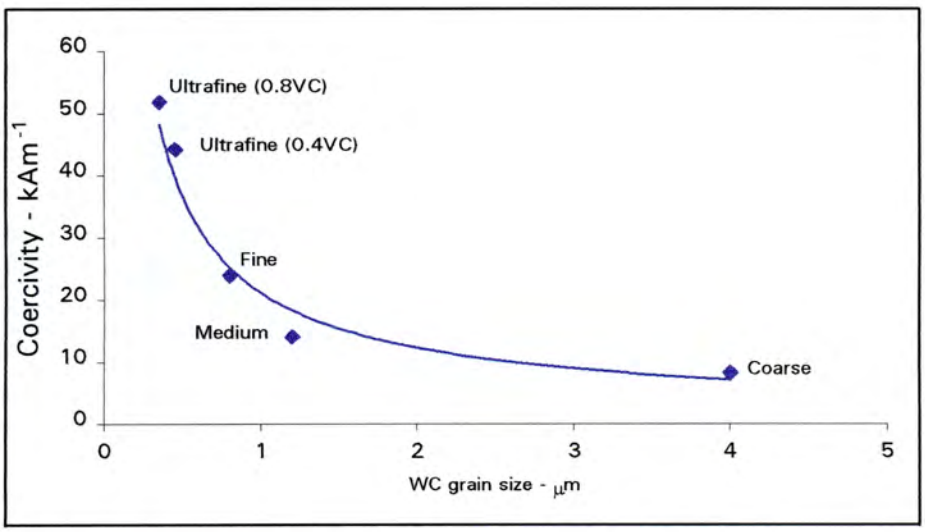

Figure 4.13 *The relationship between coercivity and carbide grain size.*

Figure 4.14 provides a comparison of the coercivity data for all the ultrafine alloys. The 0.4wt% vanadium carbide grades show a small decrease in coercivity data compared to the corresponding hardmetal composition with 0.8wt% vanadium carbide.

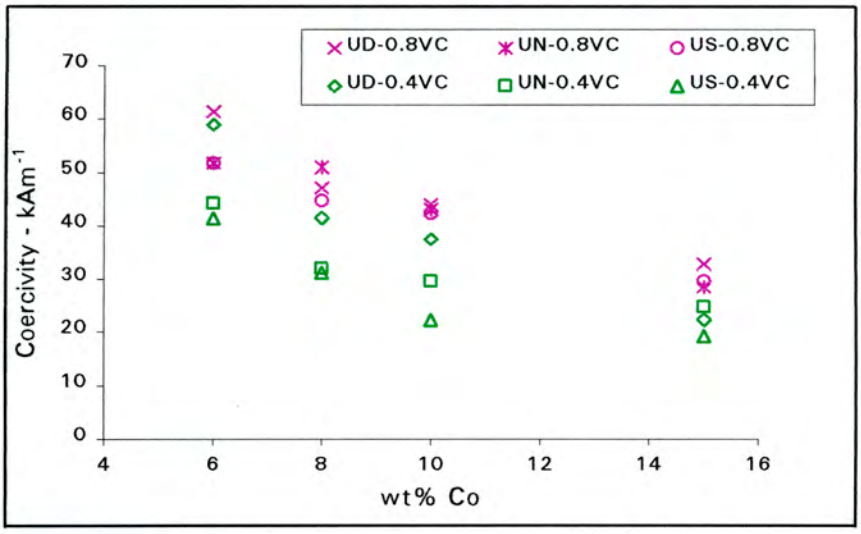

Figure 4.14 *Comparison of the coercivity data for the ultrafine alloys.*

4.7 TUNGSTEN CARBIDE GRAIN SIZE

Four different types of grain size distributions exist amongst the specimen tested namely ultrafine, fine, medium and coarse. These distributions are shown in figure 4.15 which show scanning electron micrographs of specimens taken after they were etched in Murakami's Reagent for four minutes.

The differences between the grades can be clearly seen. From the figures, it is possible to determine the grain size measurements for the conventional grades using lineal analysis. However, the grain sizes of the ultrafine grades could not be determined in the same way as the grains were too fine to resolve in the microscope.

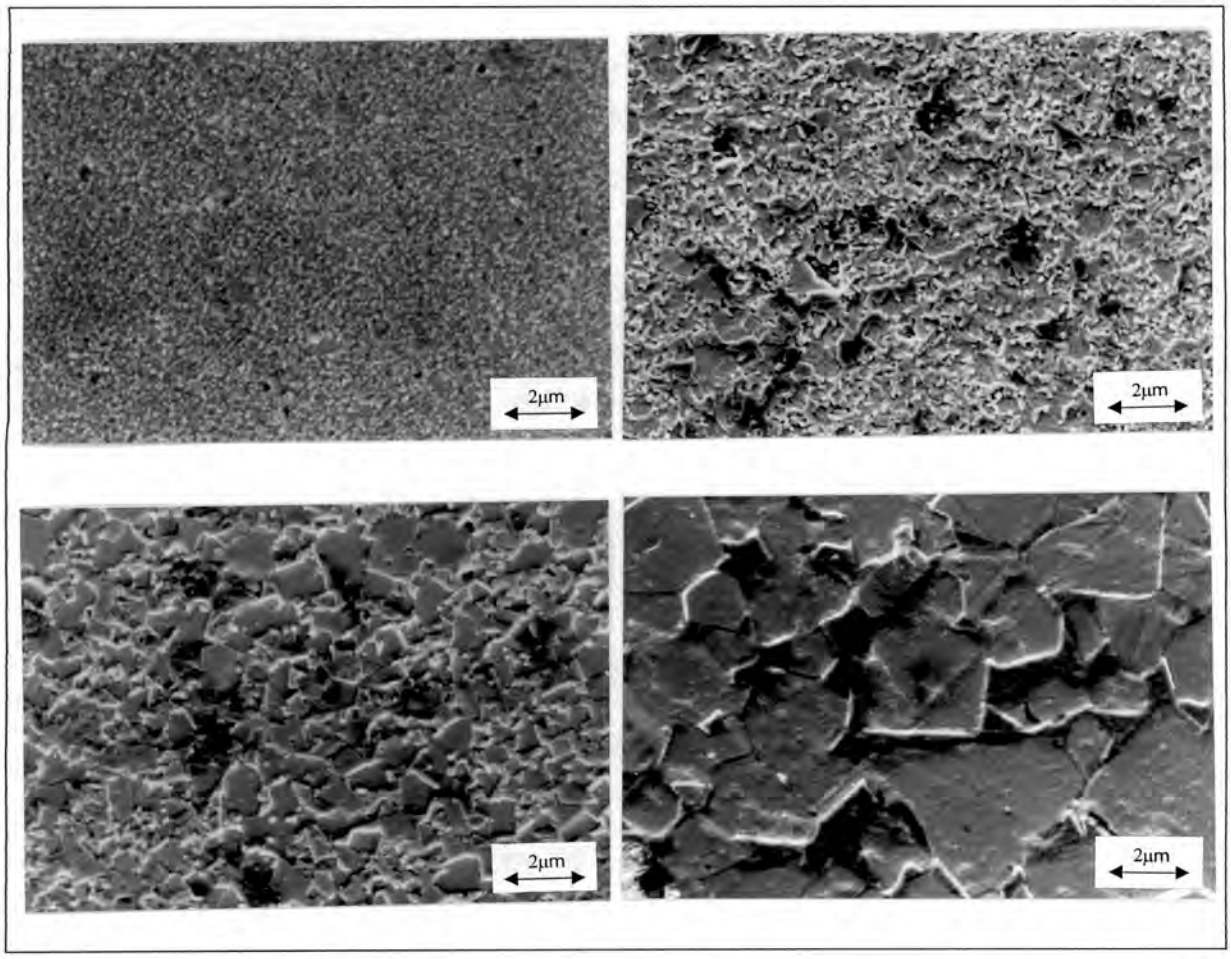

Figure 4.15 *SEM micrographs depicting the microstructures of the four different types of grain size distributions found in the alloys tested: (top-left) ultrafine UD64 grade; (top-right) fine FB62 grade; (bottom-left) medium MB6 grade and (bottom-right) coarse CB6 grade.*

Measurement of the ultrafine carbide grain size proved to be difficult to obtain. Attempts were made to leach out the cobalt binder using various acids and figure 4.16 illustrates some of the resultant microstructures. Despite some success, it was still difficult to distinguish a sufficient amount of carbide grains to make linear measurements.

It was then decided to fracture some of the hard metals and then etch the fracture surfaces with various acids. This decision was taken since the polished surfaces used for figure 4.16 were very flat and smooth. It was thought that by fracturing the specimen, the surfaces would show more contrast since they would be uneven. Success was achieved to a certain extent and the resultant microstructures are shown in figure 4.17 from which the average grain sizes were estimated from lineal analysis.

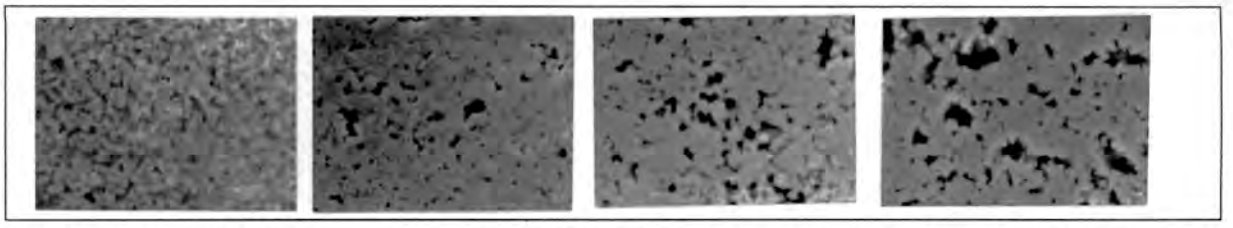

Figure 4.16 *SEM micrographs revealing the carbide grains of alloy US64 after being polished and then etched for 2 hours using (from left to right) Murakamis Reagent; KOH acid; HNO_3 acid and HCl acid.* 2μm

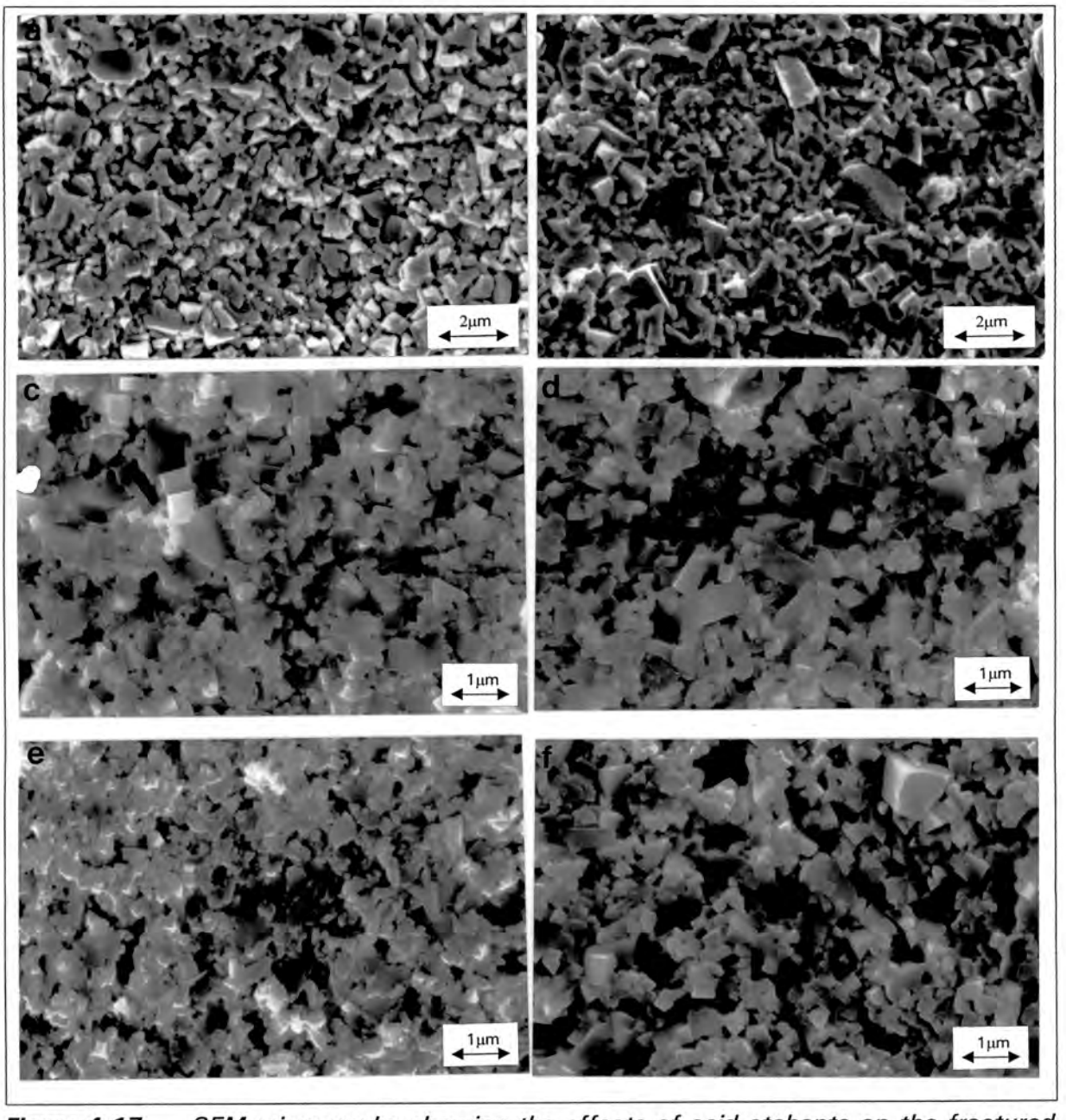

Figure 4.17 *SEM micrographs showing the effects of acid etchants on the fractured surfaces of some of the cemented carbides.*

(a) Grade UN64 etched with HNO_3 acid; (b) Grade UN64 etched with H_2SO_4 acid

(c) Grade U 154 etched with HCl acid; (d) Grade U 154 etched with H_2S

(e) Grade U 158 etched with HCl acid; (f) Grade U 158 etched with H_2S

Table 4.8 lists the average carbide grain sizes for the four types of distributions as measured during the micrographic investigations.

Table 4.8 *Estimated tungsten carbide grain size.*

Grain size distribution	***WC grain size (μm)***
Ultrafine (0.8VC)	0.35
Ultrafine (0.4VC)	0.45
Fine	0.8
Medium	1.2
Coarse	4

Theoretical equations obtained from literature were also employed to determine the carbide grain sizes. These equations were discussed in chapter 3 and are given again in equations 4.1, 4.2, 4.3 and 4.4. They make use of the value of the hardmetal's coercivity to calculate the carbide grain size. The relationship between coercivity and carbide grain size was illustrated in figure 4.13.

Porat & Malek[131]:

$$d_{WC} = 0.3\left(\frac{80}{K}\right)^{0.57(1/V_{Co})^{1/3}} \qquad \text{...(4.1)}$$

Fang & Eason[120]:

$$d_{WC} = 73\left(1 - 1.03\exp\left[-5V_{Co}\right]\right)\left(\frac{1 - V_{Co}}{KV_{Co}}\right) \qquad \text{...(4.2)}$$

Roebuck[133]:

$$d_{WC} = \frac{7.93}{K - 6.71} \qquad \text{for K} > 12.5\text{kAm}^{-1} \qquad \text{...(4.3)}$$

$$d_{WC} = \frac{10.9}{K - 1.79} \qquad \text{for K} < 12.5\text{kAm}^{-1} \qquad \text{...(4.4)}$$

The carbide grain size results determined using these theoretical equations are listed in table 4.9. The data represents the average value for each grade family*. The values for each individual grade are listed in Appendix B. One disadvantage with using these equations is that a single value is obtained per sample and thus a grain size distribution for the sample cannot be determined.

---

* Grade family refers to a set of hardmetals which were produced using powders made by the same manufacturer and which have a specific tungsten carbide grain size distribution.

Table 4.9 *Carbide grain size results obtained using the theoretical equations.*

Grade family	WC grain size - μm		
	Porat & Malek	Fang & Eason	Roebuck
UD4	1.01 ± 0.48	0.45 ± 0.10	0.27 ± 0.14
UN4	1.26 ± 0.27	0.52 ± 0.05	0.31 ± 0.09
US4	1.63 ± 0.54	0.62 ± 0.11	0.40 ± 0.17
UD8	0.74 ± 0.21	0.37 ± 0.03	0.20 ± 0.06
UN8	0.82 ± 0.27	0.39 ± 0.05	0.22 ± 0.08
US8	0.85 ± 0.21	0.40 ± 0.03	0.23 ± 0.07
FB2	2.73 ± 0.57	0.86 ± 0.11	0.67 ± 0.39
MB	6.31 ± 0.77	1.47 ± 0.15	1.31 ± 0.40
CB	15.35 ± 1.87	2.58 ± 0.15	2.51 ± 0.85

The values in table 4.9 show a large discrepancy using the three equations for each grade family. There is a some similarity between the values obtained using the equations of Roebuck[133] and Fang & Eason[120], but the values obtained using Porat and Malek's[131] equations are completely incomparable which is shown in figure 4.18 for the UD4 grade family.

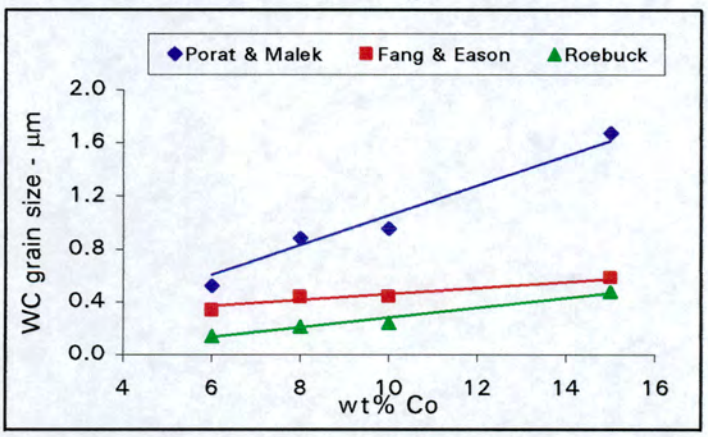

Figure 4.18 *Comparison of the three theoretical equations used to determine the carbide grain size for the 0.4wt% vanadium carbide UD alloys.*

By comparing the values obtained using the equations with those observed in the SEM micrographs for the CB and MB grades, it is easy to see that Porat and Malek's[131] equation is invalid for these alloys. However, the values obtained using the other two equations are comparable to these obtained from the micrographic analysis, the only difference being that the values obtained via Roebuck's[133] equations are about 0.2 microns smaller than those observed in by lineal analysis.

A plot of the grain sizes against coercivity values result in different types of graphs for Roebuck's equation and for that of Fang and Eason's[120] equation. An exponential distribution of data is obtained with Roebuck's[133] equation, while a linear relationship is found using Fang and Eason's[120] equation, which is illustrated in figures 4.19 and 4.20 respectively for the ultrafine alloys.

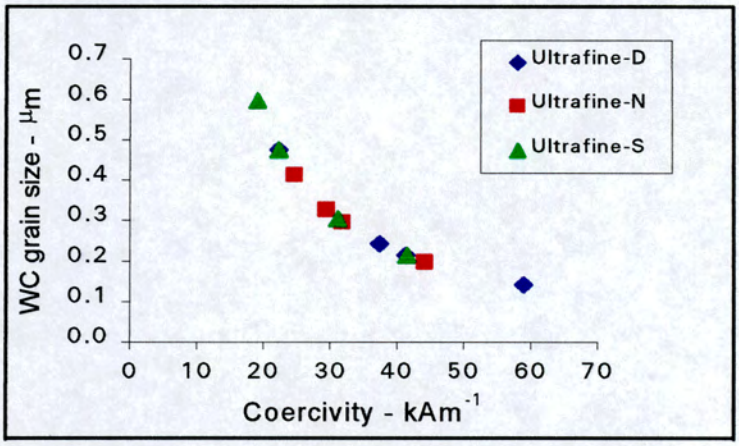

Figure 4.19 *Relationship between carbide grain size and coercivity using Roebuck's equation for the 0.4wt% vanadium carbide alloys.*

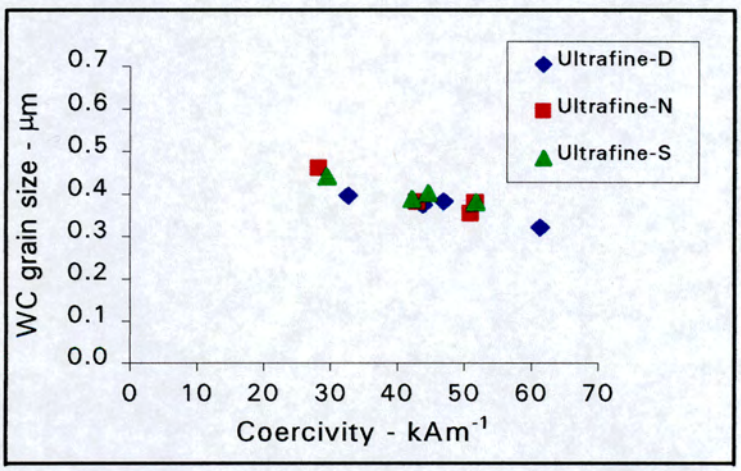

Figure 4.20 *Relationship between carbide grain size and coercivity using Fang and Eason's equation for the 0.8wt% vanadium carbide alloys.*

This clearly shows that the two equations are different, contrary to what is implied in figure 4.18. Thus caution should be exercised when using equations developed by different researchers. In most cases, equations are only valid for the range of metals for which they were developed. Attempting to extrapolate these equations for a wider range of similar metals does not appear to be successful. Fang and Eason's[120] equation is better since it gives a linear relationship for a particular grain size distribution.

It is noted that the UD grade family has a smaller grain size than both the UN (approximately 0.1μm smaller) and US (approximately 0.2μm smaller) grade families containing 0.4wt% VC. A similar observation is also noted for the 0.8wt% vanadium carbide alloys. These trends also explain the higher hardness values shown by the UD grades over the other two grades.

4.8 COBALT VOLUME FRACTION

Table 4.10 shows the data for the volume fraction of cobalt in each of the grades. The first number represents the fraction value and the second number the percentage with respect to the composite metal.

Table 4.10 *Data for the cobalt volume fractions of the tungsten carbide grades.*

Grade	V_{Co}		Grade	V_{Co}	
		%			%
UD64	0.100	10	***UD68***	0.100	10
UD84	0.131	13	***UD88***	0.130	13
UD104	0.162	16	***UD108***	0.160	16
UD154	0.234	23	***UD158***	0.234	23
UN64	0.100	10	***UN68***	0.099	9
UN84	0.132	13	***UN88***	0.130	13
UN104	0.162	16	***UN108***	0.160	16
UN154	0.234	23	***UN158***	0.233	23
US64	0.100	10	***US68***	0.099	9
US84	0.132	13	***US88***	0.131	13
US104	0.162	16	***US108***	0.161	16
US154	0.235	24	***US158***	0.233	23
FB62	0.101	10	***MB6***	0.101	10
FB82	0.132	13	***MB8***	0.132	13
FB102	0.163	16	***MB10***	0.163	16
FB152	0.236	24	***MB15***	0.236	24
CB6	0.101	10	***CB10***	0.163	16
CB8	0.133	13	***CB15***	0.237	24

The grades with similar binder contents have the same volume fractions, with a few acceptable deviations. This indicates that the correct amount of cobalt was added to each of the grades and its distribution is consistent throughout the samples. The trend of increasing volume fraction with cobalt content is shown in figure 4.21, where the 0.8wt% vanadium carbide UD alloys are plotted against the conventional hard metals.

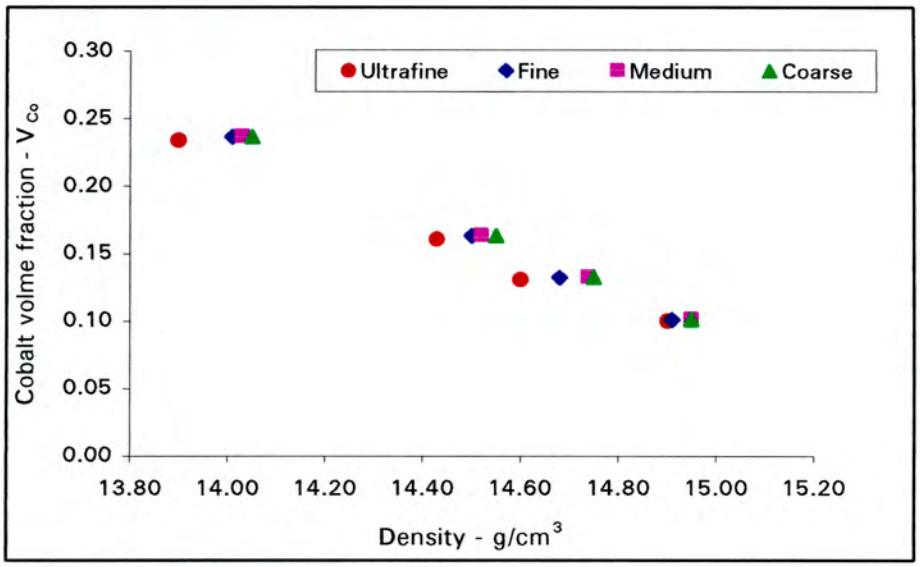

Figure 4.21 *Variation in the volume fraction of cobalt content for grades with different carbide grain size distributions.*

4.9 MEAN FREE PATH OF THE BINDER

Table 4.11 lists the data for the binder mean free path of the various alloys tested. The data shown in the table represents the values calculated using carbide grain sizes using Fang and Eason's[121] equation and the grain sizes estimated from the SEM micrographs.

Table 4.11 *The binder mean free path (MFP) data for the WC-Co grades.*

Grade	Binder mean free path - μm		Grade	Binder mean free path - μm	
	Fang and Eason	Estimated		Fang and Eason	Estimated
UD64	0.037	0.050	***UD68***	0.035	0.039
UD84	0.065	0.068	***UD88***	0.057	0.052
UD104	0.084	0.087	***UD108***	0.071	0.067
UD154	0.177	0.138	***UD158***	0.121	0.107
UN64	0.049	0.050	***UN68***	0.042	0.039
UN84	0.085	0.068	***UN88***	0.053	0.052
UN104	0.107	0.087	***UN108***	0.073	0.067
UN154	0.160	0.138	***UN158***	0.140	0.106
US64	0.053	0.050	***US68***	0.042	0.039
US84	0.088	0.068	***US88***	0.061	0.053
US104	0.141	0.087	***US108***	0.074	0.067
US154	0.207	0.138	***US158***	0.134	0.107
FB62	0.092	0.089	***MB6***	0.158	0.134
FB82	0.120	0.122	***MB8***	0.215	0.183
FB102	0.156	0.156	***MB10***	0.265	0.234
FB152	0.314	0.247	***MB15***	0.526	0.372
CB6	0.270	0.448	***CB10***	0.531	0.782
CB8	0.381	0.611	***CB15***	0.833	1.241

The binder mean free path increases with an increase in the cobalt content and grain size. This is shown in figure 4.22 where the conventional hard metal grades are compared to the 0.4wt% vanadium carbide UD grades. The coarser grades show a much steeper increase in the mean free path with an increase in cobalt content than the other grades. The mean free path values used in the figure represents the estimated data from table 4.11.

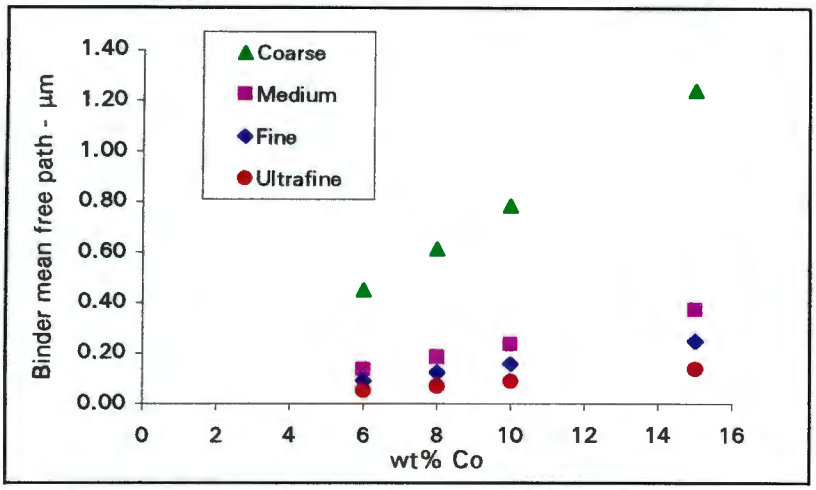

Figure 4.22 *Relationship between binder MFP and cobalt content for a series of cemented carbides with varying carbide grain sizes.*

Figures 4.23 and 4.24 compare the binder mean free path for the 0.4 and the 0.8wt% vanadium carbide ultrafine alloys respectively. There is a greater variation of mean free path values amongst the 0.4wt% vanadium carbide alloys across the whole cobalt range compared to the 0.8wt% vanadium carbide alloys, where the only variation is noted amongst the 15% cobalt grades. The mean free path values used in the figures represent the values obtained using Fang and Eason's[120] equation from table 4.11.

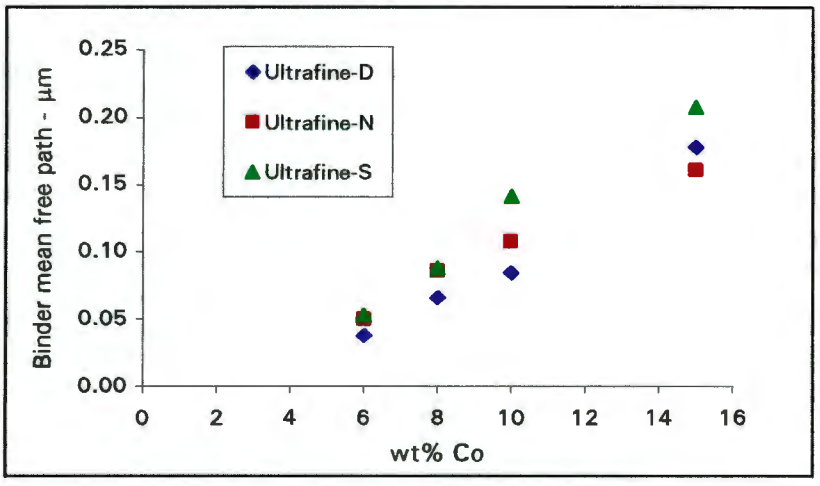

Figure 4.23 *Relationship between binder MFP and cobalt content for the 0.4wt% vanadium carbide ultrafine alloys.*

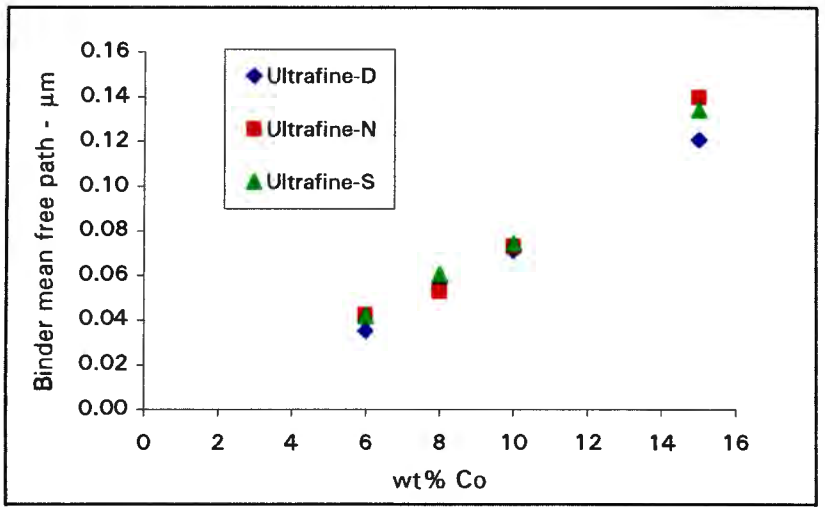

Figure 4.24 *Relationship between carbide grain size and cobalt content for the 0.8wt% vanadium carbide ultrafine alloys.*

Figure 4.25 shows the variation in hardness with mean free path for hard metals with varying grain sizes and cobalt contents. The 0.8wt% vanadium carbide ultrafine UD grades are used in this figure. As the carbide grain size decreases the respective slopes of the plots become greater. A much wider range in the mean free path is obtained for the coarser grained specimen, but at the same time the coarser grades show a limited hardness range.

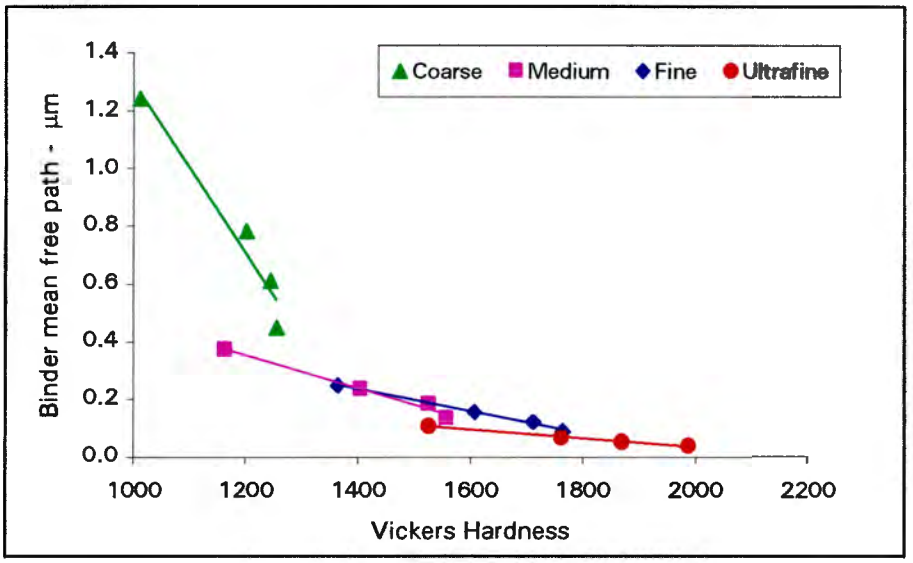

Figure 4.25 *Relationship between Vickers hardness and binder MFP for the hard metals.*

Chapter 5

RESULTS:
PALMQVIST FRACTURE TOUGHNESS

5.1 INTRODUCTION

This chapter outlines the results of toughness testing carried out on the cemented carbides using the Palmqvist crack test method. This method employs a Vickers pyramid diamond to indent the samples. The cracks that emanate from the four corners of the indent impression on the specimen are known as Palmqvist cracks. The length of these cracks are measured and used to determine the Palmqvist fracture toughness for that specimen.

The results in this chapter are set out as follows:

1) The crack length measurements
   a) specimen surface preparation
   b) the effects of the indenting loads
   c) microscopic studies of the cracks
2) The Palmqvist fracture toughness test results

The influence of cobalt content, vanadium carbide and hardness on the toughness is also discussed. Comparisons are drawn between the ultrafine grades made via the three different powder routes. Finally the toughness of the ultrafine grades are compared to the toughness of conventional cemented carbides.

5.2 CRACK LENGTH MEASUREMENTS

5.2.1 SPECIMEN SURFACE PREPARATION

The importance of proper specimen surface preparation for the Palmqvist crack measurements was discussed in detail in chapter 2. Each grade of hard metal was prepared according to the procedure outlined in Chapter 3, section 3.6. using equation 5.1 developed by Exner[173].

$$A = \frac{D_1 - D_2}{2} . \cot \frac{\alpha}{2} \qquad \text{...(5.1)}$$

Where: A $\Rightarrow$ thickness of layer removed

$D_{1/2} \Rightarrow$ diagonals of the Vickers indentation before and after polishing;

$\alpha \Rightarrow$ angle between the faces on the top of the Vickers pyramid (136°).

The crack lengths produced by each Vickers hardness indentation was measured using optical microscopy at a magnification of 200X. Some crack lengths were also measured using a SEM to compare the results to those made using the optical microscope. Figure 5.1 shows the comparison using the two microscopes to measure the crack lengths on an ultrafine alloy.

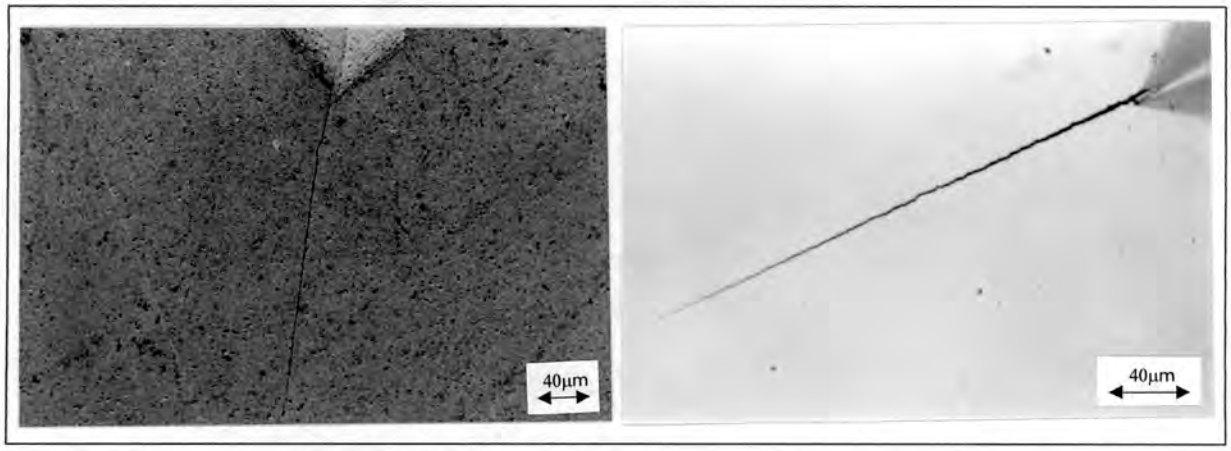

Figure 5.1 *Micrographs of a crack measurement made on a UD68 grade using scanning electron microscopy(left) and optical microscopy(right).*

It was found that the SEM measurements were longer than the optical measurements by 0.01%. This difference is due to the higher magnifications that can be achieved in the SEM.

However, as the error did not have any significant effect on the resultant Palmqvist toughness values, it was decided to continue using the optical microscope for the crack length measurements. The optical microscope was chosen since it does not require any setting up procedures and the measurements are very easy to make.

The specimens were polished using two different diamond suspensions, namely a 9μm grit size and a 0.25μm grit size. Three indenting loads of 196, 294 and 491N were employed. Table 5.1 lists the results of the polishing procedure carried out on grade UD64 using 9μm diamond grit size. The last row of data in table 5.1 is obtained using 0.25μm diamond grit and an indenting load of 491N. This was included to provide a comparison to that using 9μm diamond grit with a load of 491N. Similar tables were generated for each grade of hard metal.

Table 5.1 *The influence of indenting load and diamond grit size on the crack lengths for the UD64 ultrafine grade. The data represent the average values of five indents made per time interval.*

A ⇒ *amount of material removed after each time interval*

TCL ⇒ *total crack length of indent measured after each time interval*

Load N	Time (min)	0	1	2	3	4	5	10	15	20
196	A (μm)	0	16	43	72	99	121	148	197	237
	TCL (μm)	180	415	405	400	400	401	400	400	400
294	A	0	23	52	84	113	136	163	212	251
	TCL	380	585	590	545	665	625	485	530	505
491	A	0	33	64	103	138	163	193	247	298
	TCL	710	955	1000	955	1005	895	1030	865	825
491	A	0	4	-	-	-	12	31	66	-
	TCL	710	955	-	-	-	845	905	999	-

It is noted that an increase in crack length is obtained with an increase in the indenting load. Also as the amount of material removed increases, the crack lengths produced by the respective loads' approach a constant value. This is most obvious when considering the data of the 196N load as illustrated in figure 5.2.

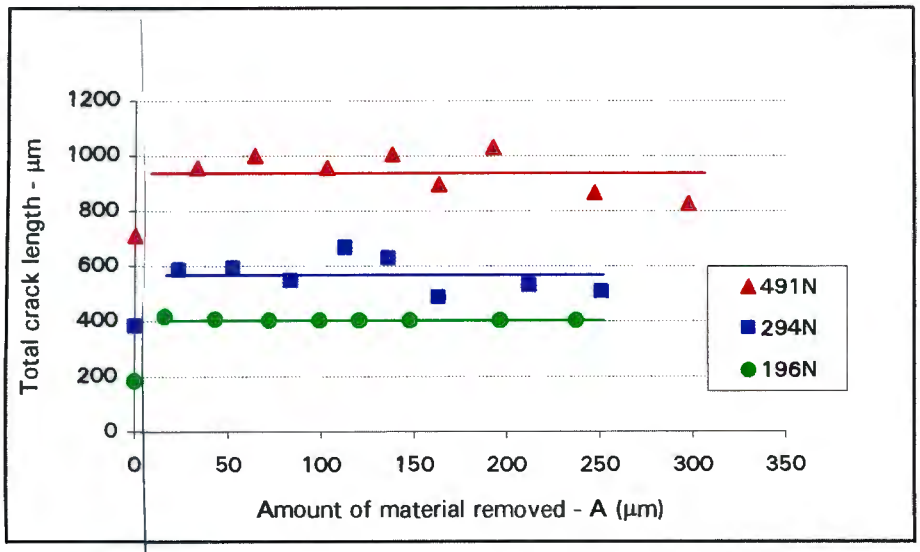

Figure 5.2 *Influence of extended polishing time on crack lengths for grade UD64.*

From the figure it is seen that there is more scatter in the data as the testing load is increased. This trend was observed for all the hard metal grades. The solid lines in the figure represent the average crack lengths for each indenting load. When a 'constant' crack length was reached for each grade at each load, the polishing procedure was halted for that grade. Similar graphs were produced for each grade using the 0.25µm diamond grit and figure 5.3 shows the comparison in using the two different diamond grits for the UD64 grade at loads of 491N and 196N.

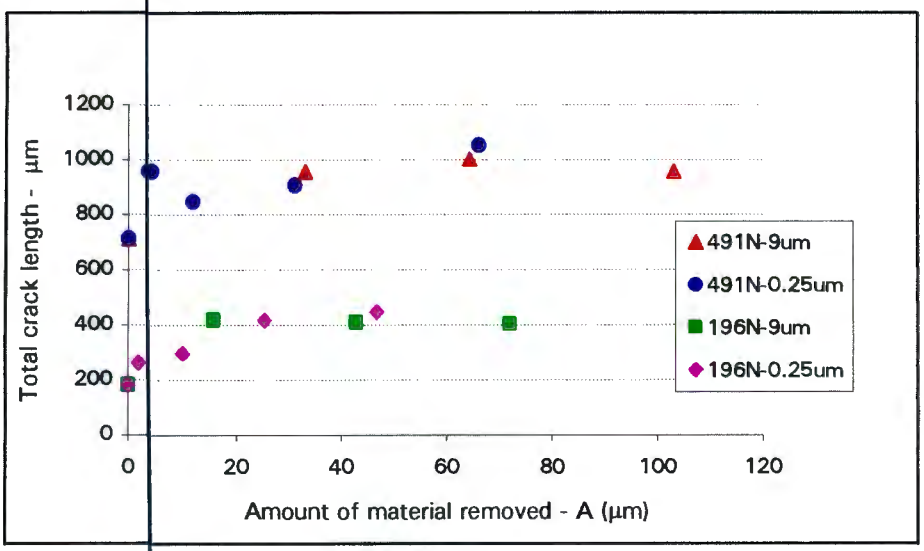

Figure 5.3 *Comparison of 0.25µm and 9µm diamond grit size on polishing procedure for the UD64 grade using indenting loads of 491N and 196N.*

It is seen that there is no great difference in the average crack lengths obtained using the different diamond grit sizes. The only noticeable difference is that after the same time intervals, more material is removed by using the 9µm grit. This is expected because the 9µm grit is coarser than the 0.25µm grit.

Various researchers have shown that annealing the specimen at a temperature of 800°C decreases the amount of polishing time required to obtain a constant crack length. Therefore it was decided to anneal two sets of unpolished hard metals at two different temperatures and then polish them using the same procedure as described previously. One set of hard metals was annealed at 800°C and the second set was annealed at 900°C. Table 5.2 lists the crack length data obtained for grade UD104 after the specimen were annealed and figure 5.4 illustrate these results.

Table 5.2 *The influence of annealing on the UD104 grade crack lengths using an indenting load of 491N.*

Condition	Time (min)	0	1	5	10	15
As received condition	A	0	5.84	17.51	44.74	81.68
	TCL	550	630	660	715	745
Annealed at 800°C	A	0	5.84	21.40	38.90	58.35
	TCL	570	650	690	695	825
Annealed at 900°C	A	0	3.89	15.56	29.18	54.46
	TCL	620	645	725	720	795

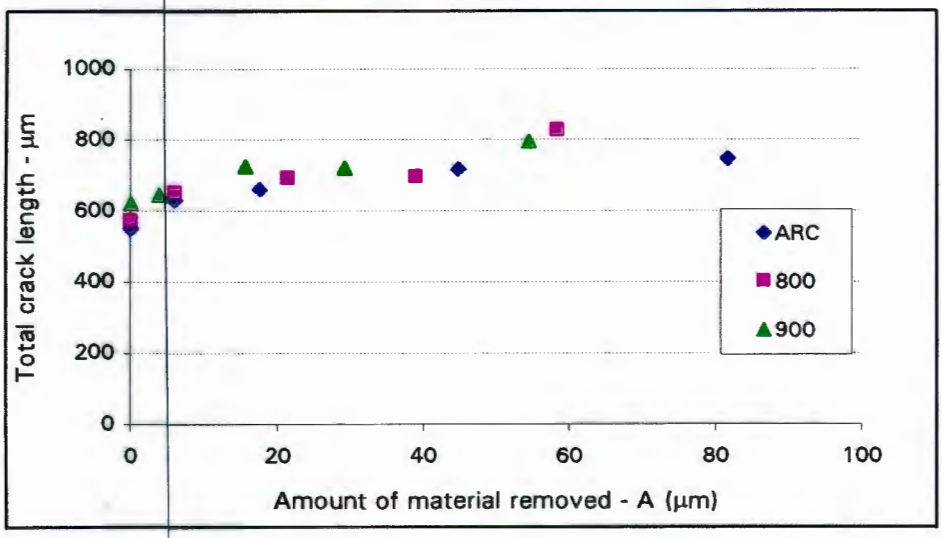

Figure 5.4 *Influence of annealing on crack lengths for grade UD104 using an indenting load of 491N.*

It appears that annealing does increase the initial crack lengths measured. After 1 minute of polishing the crack lengths produced by the 900°C anneal are 15microns longer than those specimen in the as-received condition. After 5 minutes of polishing the 900°C annealed crack lengths are 65 microns longer than the unannealed crack lengths.

Annealing at 900°C also proved to be more efficient in reducing the polishing time than the suggested 800°C temperature. However after a period of polishing time the crack lengths produced by the different conditions reach the same average crack length. All the hard metals displayed similar behaviour. This trend is clearly illustrated in figure 5.5 for the 0.4wt% vanadium carbide ultrafine UN grades which shows that spread of data from differently annealed conditions of various cobalt contents is similar.

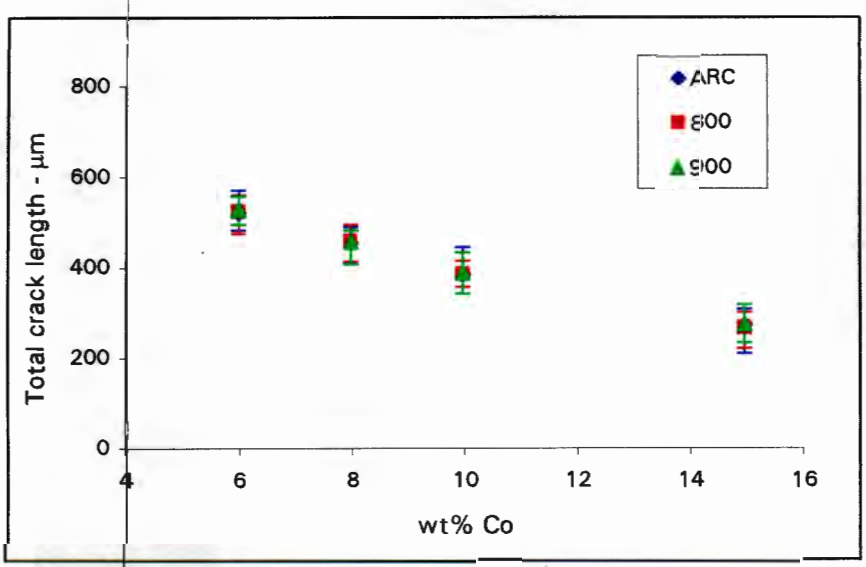

Figure 5.5 *Influence of annealing on the total crack length for all the 0.4wt% vanadium carbide UN grades using an indenting load of 294N.*

Immediately after obtaining constant crack lengths for each grade, the specimen surfaces were polished for a further 5 minutes to provide fresh surfaces on which the Palmqvist tests would be made.

5.2.2 EFFECT OF INDENTING LOAD

The average total crack lengths obtained for each hard metal grade with respect to indenting load and heat treated condition is given is Appendix C. Table 5.3 lists the data for four 6wt% cobalt grades in the as-received condition. Each grade represents a different type of carbide grain size distribution.

Table 5.3 *Influence of indenting load on crack length for the 6wt% cobalt hard metal grades with different carbide grain sizes.*

Grade	Total crack length at respective loads - µm		
	196N	*294N*	*491N*
UN68	394 ±6	592 ±13	1005 ±14
FB62	330 ±4	495 ±16	827 ±8
MB6	203 ±9	304 ±9	509 ±16
CB6	89 ±4	133 ±11	222 ±11

The finer the carbide grain size, the longer the crack lengths become. This is due to the finer grained alloys being harder than the coarser grades. Thus as the crack length decreases the toughness is expected to increase. The data from table 5.4 is graphically shown in figure 5.6.

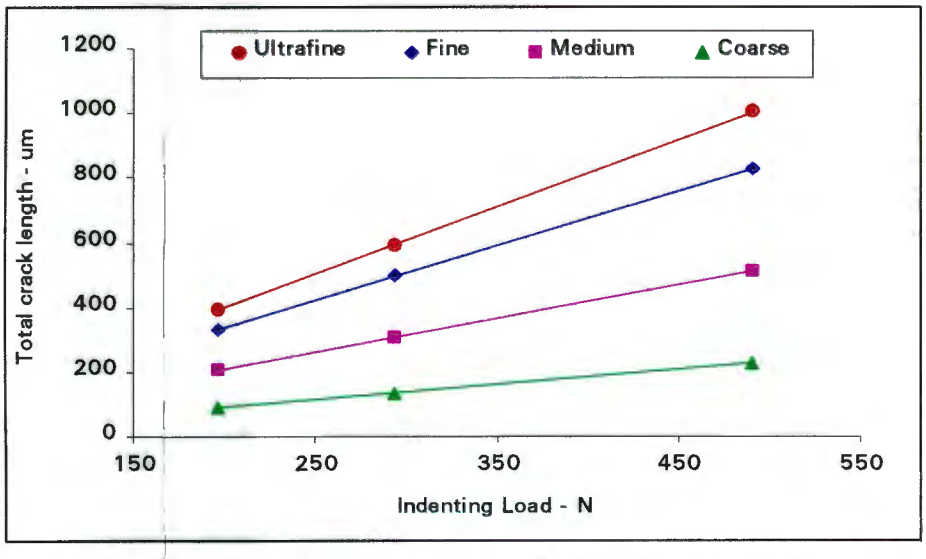

Figure 5.6 *Influence of carbide grain size distribution on the total crack length for the 6wt% cobalt alloys.*

The gradients of these plots increase as the carbide grain size decreases. This implies that as the indenting load is increased, the crack lengths in the ultrafine grades increase more rapidly than those of the coarser alloys. At an indenting load of 196N (20kg), there is a 305 micron difference between the UN8 and CB grades, while at an indenting load of 491N (50kg), the difference is 783 microns. This reflects an increase of 478 microns in the crack length with an increase of 30kg in the indenting load.

It can also be seen, from figure 5.7, that as the hardness increases, which is associated with a decrease in the cobalt content, an increase in the crack length occurs.

Furthermore, the gradients of each plot increase as the carbide grain size decreases. It should also be noted that a wide range in crack lengths is obtained along with a wide range in hardness values as the carbide grain size decreases. For example for the CB grades, an increase of 250 Vickers results in a 100micron increase in the crack lengths. For the UD grades, a 250 Vickers' increase in the hardness is associated with a 270micron increase in the crack length.

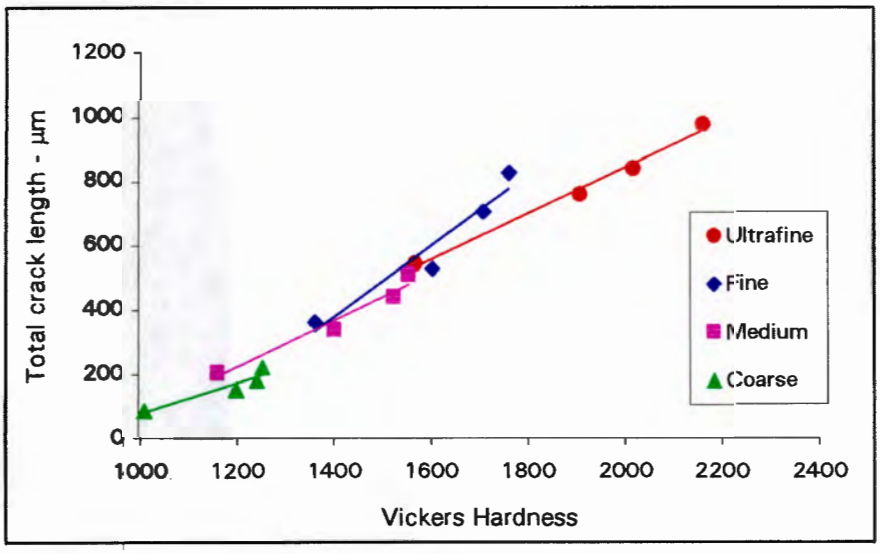

Figure 5.7 *Effect of hardness and carbide grain size on the crack lengths of various hard metal grades using an indenting load of 491N.*

The 0.8wt% vanadium carbide grades were also found to have longer crack lengths than the 0.4wt% vanadium carbide alloys at similar indenting loads. The only exception to this was the UD64 grades that sometimes displayed crack lengths that were longer than some of the UD68 alloys. This is probably due to the eta phase found in the UD64 grade. Figure 5.8 illustrates the average total crack lengths measured for the ultrafine alloys indented using a load of 196N.

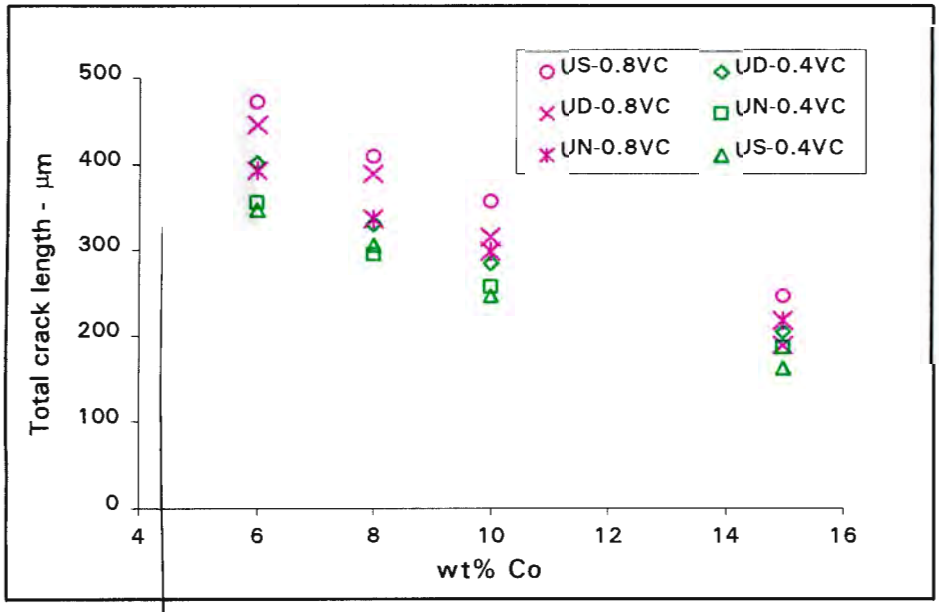

Figure 5.8 *Comparison of the ultrafine grades using an indenting load of 196N.*

In the US8 alloys the crack lengths are the longest while the US4 alloys show the shortest crack lengths. Therefore these grades are expected to show the lowest and highest fracture toughness values respectively for all the ultrafine grades investigated. This observation was also made when comparing the ultrafine grades indented with the 296N and 491N loads.

The influence of vanadium carbide on the crack lengths was different for each of the ultrafine grades produced using the three different powder manufacturing routes. These differences are illustrated in figures 5.9, 5.10 and 5.11. Each figure represents a ultrafine powder production route, namely, D, N and S. The expected trend of decreasing crack length with an increase in cobalt content is observed for all the grades. This is consistent with the fact that an increase in the cobalt content generally provides an increase in fracture toughness.

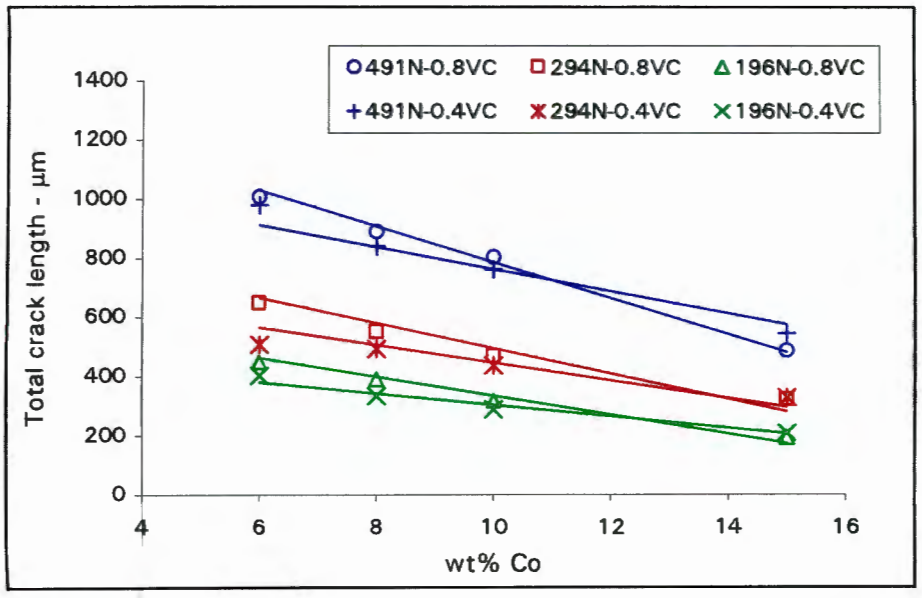

Figure 5.9 *Influence of vanadium carbide and cobalt content on the ultrafine UD grades.*

From figure 5.9 it is seen that the 0.4wt% vanadium carbide grades have shorter crack lengths than the corresponding 0.8wt% vanadium carbide grades across the cobalt range, except for 15wt% cobalt, where their crack lengths are slightly longer. This trend is the same for each indenting load used, except for the 294N load where the two values are almost equal. It is also noticeable that the slopes of the crack lengths with cobalt contents for the 0.8wt% VC grades are steeper than those of the 0.4wt% VC alloys.

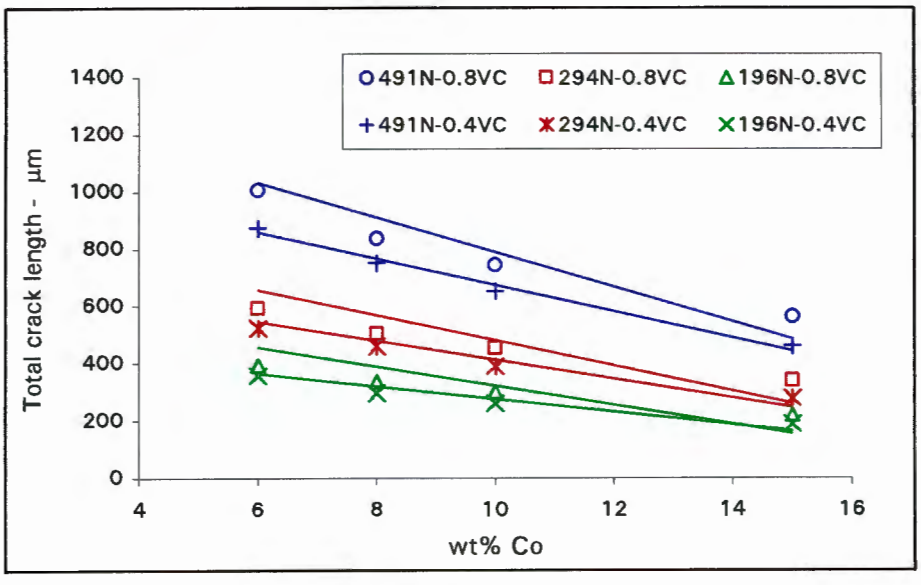

Figure 5.10 *Influence of vanadium carbide and cobalt content on the ultrafine UN grades.*

In the N grades, the 0.4wt% vanadium carbide grades have shorter crack lengths than the 0.8wt% vanadium carbide grades. For each indenting load the difference between the 0.4wt% and 0.8wt% vanadium carbide grades is largest at 6wt% cobalt. This difference becomes smaller with increasing cobalt.

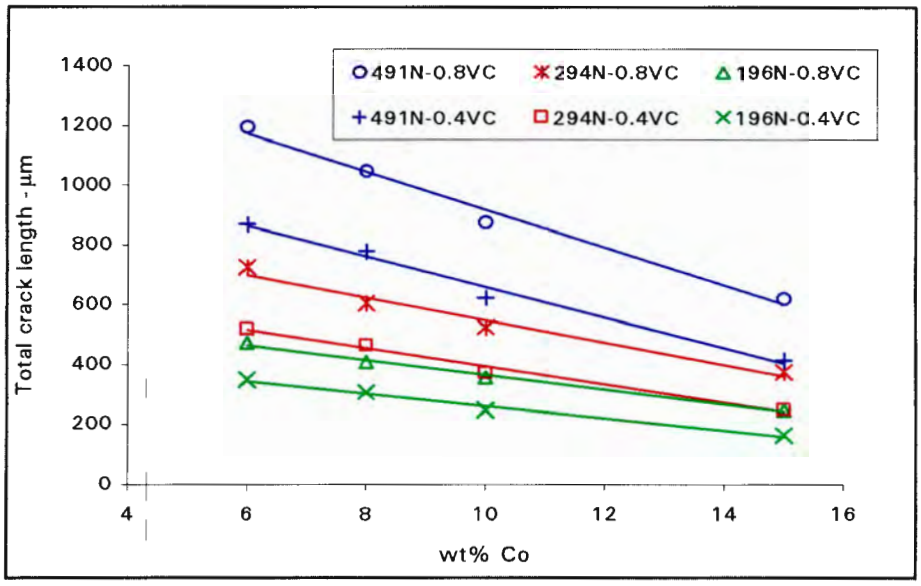

Figure 5.10 *Influence of vanadium carbide and cobalt content on the ultrafine US grades.*

The S grades show a remarkable contrast to the D and N grades. There is a substantial difference between the crack lengths of the 0.4wt% and the 0.8wt% vanadium carbide S grades. As the indenting load increases, the difference increases. At a load of 196N the difference between the 0.4wt% and the 0.8wt% VC grades is approximately 120µm, while at the load of 491N, the difference is almost 324µm. This difference is practically consistent across the cobalt range implying that the gradients for the respective slopes are the same. This contrasts with the D and N grades where the difference between the 0.4 and 0.8wt% vanadium carbide slopes becomes less with increasing cobalt. The reasons for this cannot be explained at this time. Factors such as the influence of sintering and plastic deformation within each grade need to be considered.

5.2.3 FRACTOGRAPHY

The Palmqvist cracks of the various hard metals were studied using scanning electron microscopy. It was found that the crack width remained approximately constant except close to the tip where its width decreased sharply from about 1μm down to zero microns as shown in figure 5.11.

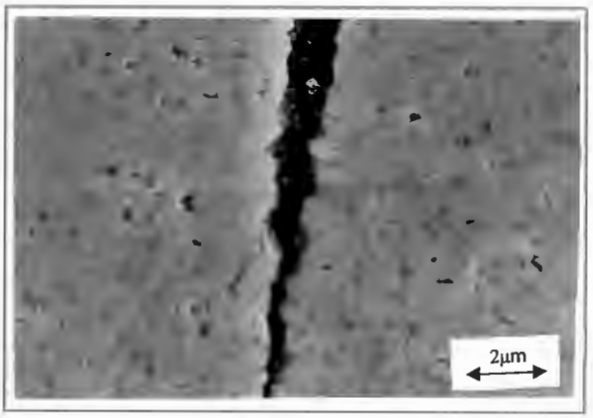

Figure 5.11 *SEM micrograph of grade UN104 showing the tapering of the Palmqvist crack beginning from the indent corner.*

The cracks were also studied to establish the choice of crack paths taken. It was found that most of the cracks proceeded along an intergranular crack path through the binder phase. It has been reported that this trend is common amongst cemented carbides. Typical crack paths are shown in figure 5.12 for grades UN68(left) and UD158(right).

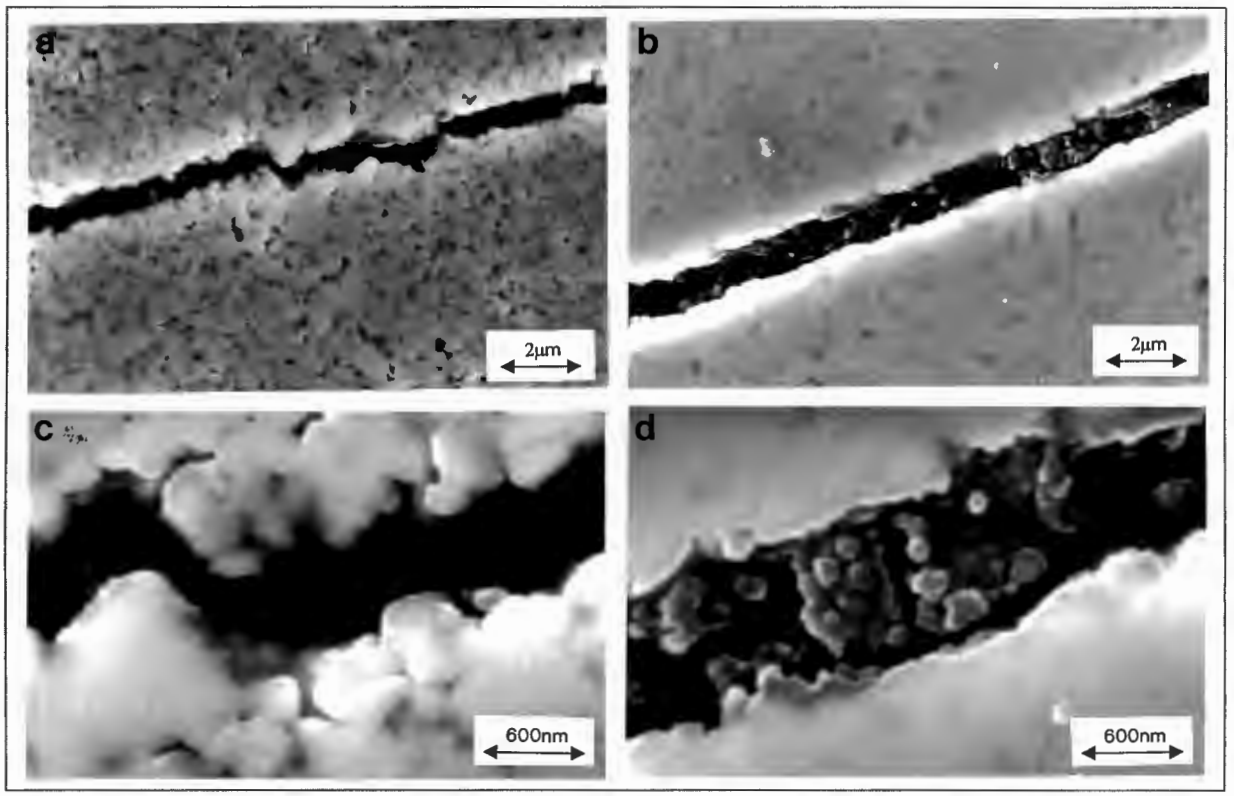

Figure 5.12 *SEM micrographs showing typical crack paths in alloys UN68(a & c) and UD158(b & d).*

Micrographs (c) and (d) shown in figure 5.12 are magnified sections of the two micrographs shown directly above them, i.e. (a) and (b). Alloy UD158 has been etched. In alloy UN68, sections of cobalt rupture can be seen along the crack path, indicating that the crack proceeded through the binder phase. This is confirmed in grade UD158, where etching has taken away some of the cobalt and it is clearly seen that the crack path goes along the carbide grains. Figure 5.13 shows crack paths found in the conventional cemented carbides. These are similar to those shown in figure 5.12.

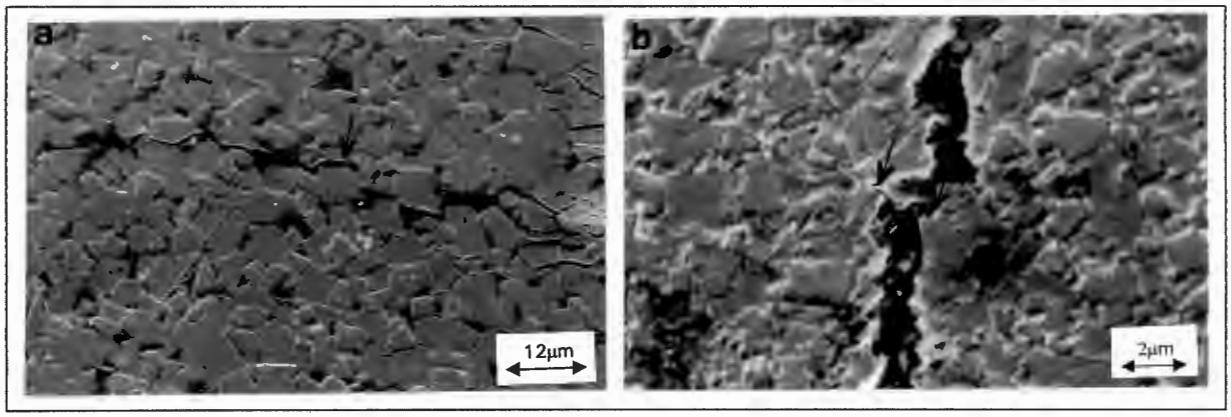

Figure 5.13 *SEM micrographs showing typical crack paths found in conventional cemented carbides.*

5.3 PALMQVIST FRACTURE TOUGHNESS (K_{Ic})

The Palmqvist fracture toughness data for all the hard metals is given in Appendix D. The appendix lists the average values for the Palmqvist toughness taken at each of the three indenting loads and in each of the two heat treated conditions. Table 5.4 lists the data for alloys with four different types of grain size distributions. Also shown is the error representing one standard deviation. The data is illustrated graphically in figure 5.14.

Table 5.4 *Palmqvist fracture toughness data for hard metals with varying carbide grain size distributions.*

Grade	Palmqvist fracture toughness – $MNm^{-3/2}$			
	6wt% Co	*8wt% Co*	*10wt% Co*	*15wt% Co*
UD8	8.7 ±0.22	9.2 ±0.18	9.7 ±0.06	10.9 ±0.29
FB	9.1 ±0.31	9.7 ±0.24	11.2 ±0.21	12.1 ±0.17
MB	10.9 ±0.16	11.6 ±0.18	12.7 ±0.27	14.9 ±0.22
CB	14.8 ±0.19	16.3 ±0.23	17.4 ±0.36	21.2 ±0.4

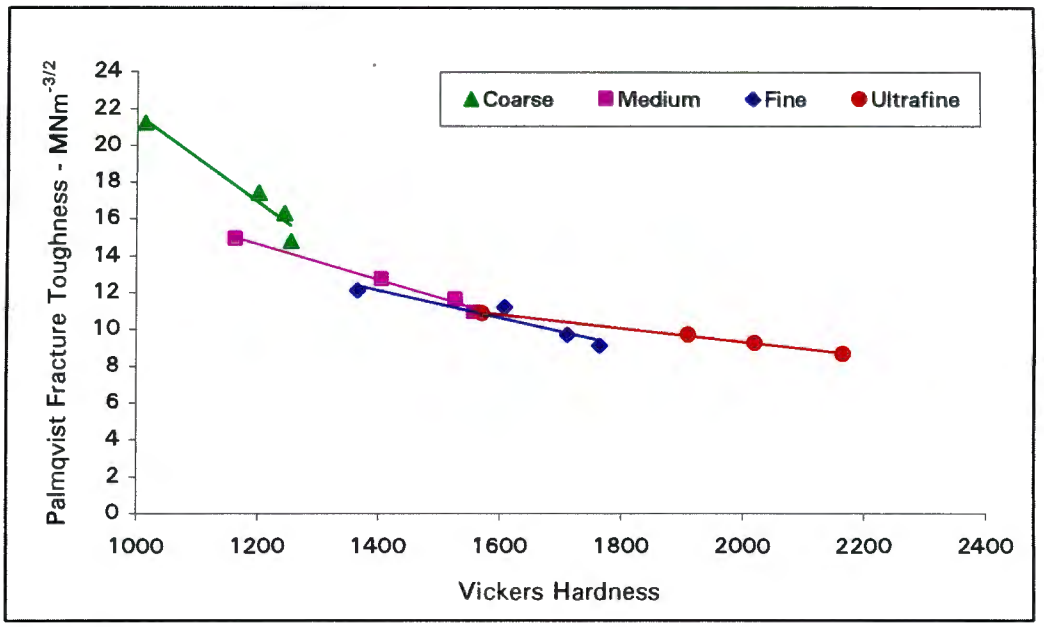

Figure 5.14 *Comparison of the Palmqvist toughness of a series of hard metals with different carbide grain size distributions.*

The Palmqvist toughness decreases as the hardness increases for each set of hard metals. As the grain size decreases from coarse to ultrafine, the slopes of the graphs become more gradual. This means that the toughness decreases more rapidly in coarser grained hard metals. For the CB grades, the toughness decreases by 6.4MNm$^{-3/2}$ with a 243 Vickers increase in hardness from 6 to 15wt% cobalt. This change is less for the finer grained metals. The UD8 grades show a decrease in toughness of only 2.2MNm$^{-3/2}$ for a hardness increase of 863 Vickers over the 6 to 15wt% cobalt range. It would appear that as the grain size and the cobalt content decreases, the toughness value is tending towards a constant value of 8MNm$^{-3/2}$.

When analysing the individual hard metals, it was noted that the UD8 and MB grades followed an almost strict linear relationship between toughness and hardness. The CB and FB grades although displaying a linear relationship, showed more scatter in their data points.

Table 5.5 shows the Palmqvist fracture toughness values for the UD grades. These results are illustrated graphically in figure 5.15. The error values given represent one standard deviation.

Table 5.5 *Palmqvist fracture toughness data for the ultrafine UD grades.*

wt% VC	Palmqvist fracture toughness – $MNm^{-3/2}$			
	6wt% Co	*8wt% Co*	*10wt% Co*	*15wt% Co*
0.4	9.04 ±0.25	9.35 ±0.1	9.62 ±0.25	10.54 ±0.3
0.8	8.66 ±0.22	9.24 ±0.18	9.70 ±0.06	10.85 ±0.29

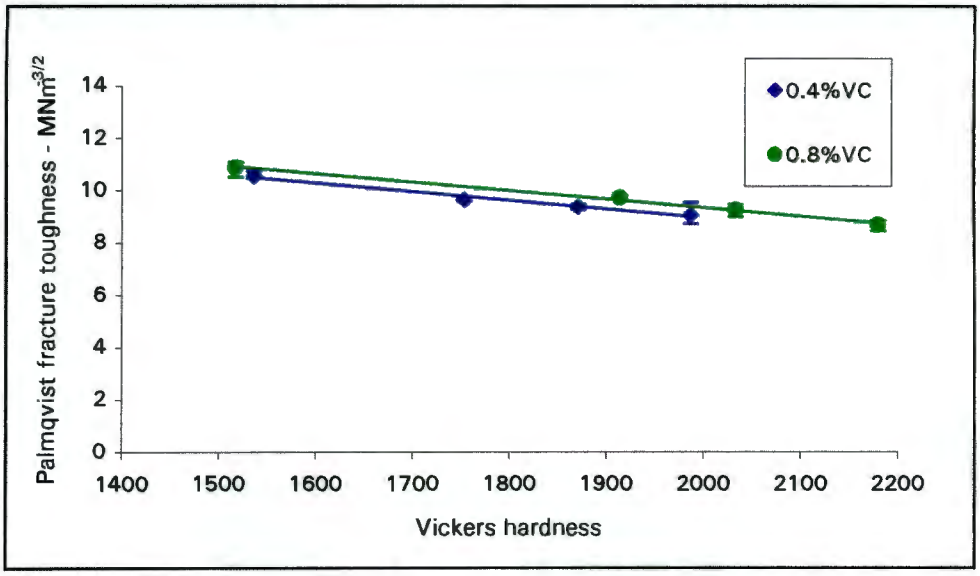

Figure 5.15 *Palmqvist fracture toughness for the ultrafine UD grades.*

In figure 5.15 both the 0.4 and the 0.8wt% vanadium carbide grades display linear relationships between toughness and hardness. The remarkable observation with these two grades is that the 0.8wt% vanadium carbide alloys have similar toughness values to the 0.4wt% vanadium carbide grades across the cobalt range tested which is an unusual trend in cemented carbides. This difference between the grades is only $0.25MNm^{-3/2}$.

Whilst the 0.8wt% vanadium carbide grades display a wider range in hardness and toughness values compared to the 0.4wt% vanadium carbide alloys, the slopes of the two graphs are similar, implying that the toughness decreases at the same rate with the addition of vanadium carbide for this particular set of alloys.

Table 5.6 gives the Palmqvist fracture toughness results for the ultrafine UN grades and these values are illustrated in figure 5.16. The error values given represent one standard deviation.

Table 5.6 *Palmqvist fracture toughness data for the ultrafine UN grades.*

wt% VC	Palmqvist fracture toughness – $MNm^{-3/2}$			
	6wt% Co	*8wt% Co*	*10wt% Co*	*15wt% Co*
0.4	9.21 ±0.05	9.75 ±0.07	10.19 ±0.03	11.32 ± 0.06
0.8	9.09 ±0.04	9.60 ±0.03	9.87 ±0.02	10.58 ±0.05

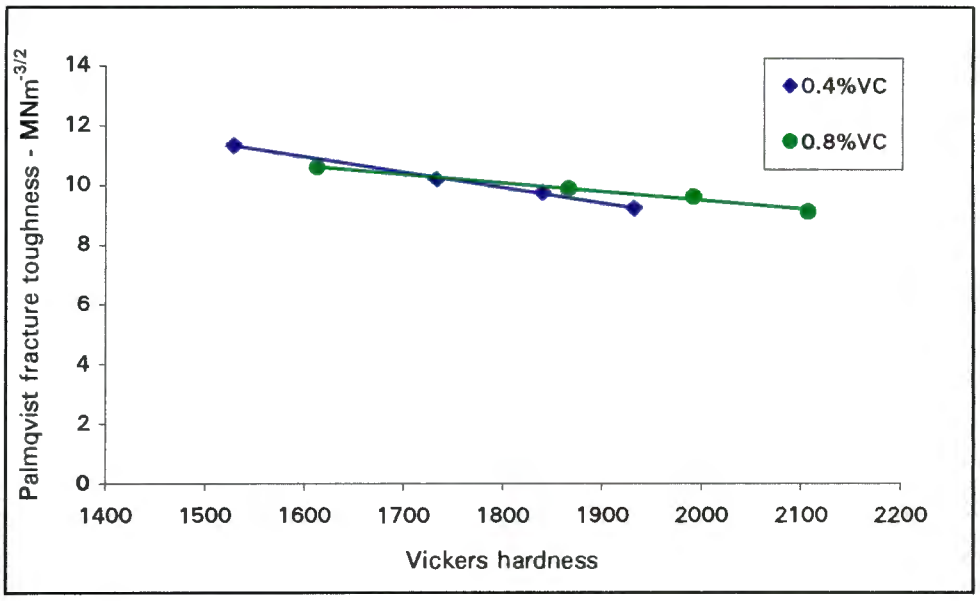

Figure 5.16 *Palmqvist fracture toughness for the ultrafine UN alloys.*

The UN grades display a different behaviour to the UD grades, in that there is a cross-over between the 0.4 and the 0.8wt% vanadium carbide alloys at a hardness of approximately 1720 Vickers. The toughness of the 0.4 and 0.8wt% vanadium carbide grades are similar.

Table 5.7 gives the results of the Palmqvist fracture toughness for the US hard metals and figure 5.17 illustrates these values. The error given in the table represents one standard deviation.

Table 5.7 *Palmqvist fracture toughness data for the ultrafine US grades.*

wt% VC	Palmqvist fracture toughness – $MNm^{-3/2}$			
	6wt% Co	*8wt% Co*	*10wt% Co*	*15wt% Co*
0.4	9.23 ±0.02	9.59 ±0.04	10.31 ±0.02	11.82 ±0.02
0.8	8.38 ±0.06	8.72 ±0.03	9.12 ±0.04	10.09 ±0.03

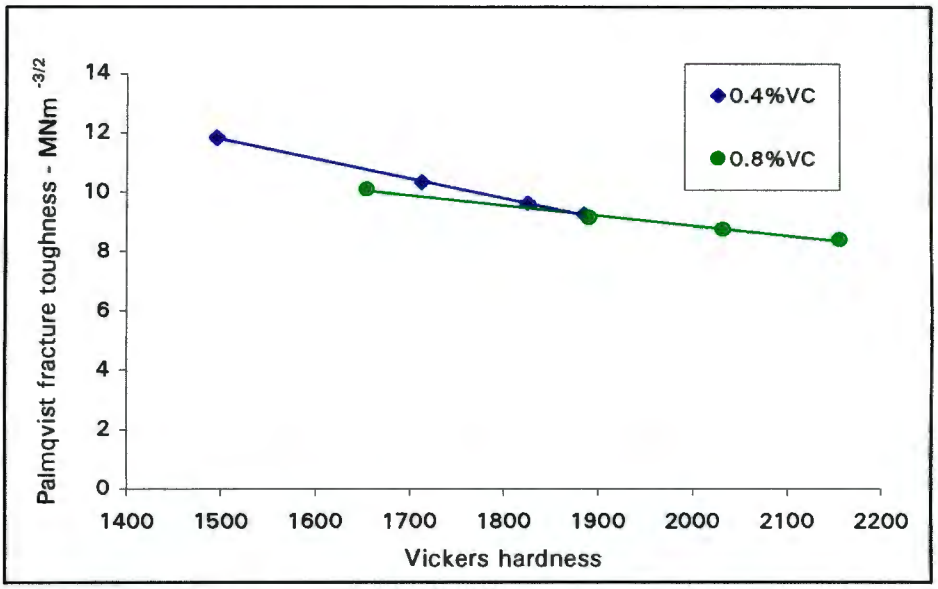

Figure 5.17 *Palmqvist fracture toughness for the ultrafine US alloys.*

The US grades show different trends to both the UD and the UN alloys. Figure 5.17 shows that the 0.4wt% VC alloys have higher toughness values than the 0.8wt% VC alloys at similar cobalt contents for all metals tested. A similarity does exist between the UN and the US alloys in that the slopes of the graphs for the 0.4wt% alloys are steeper than the slopes of the 0.8wt% VC alloys. This difference is slightly more pronounced for the US grades.

In the US alloys containing 0.4wt% vanadium carbide, there is a 2.59MNm$^{-3/2}$ decrease in toughness over a 400 Vickers hardness range. In comparison, the 0.8wt% VC-US alloys show a lower decrease of 1.71MNm$^{-3/2}$ over a 520 Vickers hardness range. Therefore, the toughness decreases quicker with a decrease in the vanadium carbide content for these hardmetals. The scatter in data for each grade is negligible, as the error bars cannot be observed on the figure.

A comparison between the ultrafine alloys made by the three different powder routes is more easily seen when grouped together. Hardmetals with similar vanadium carbide contents are shown in figures 5.18 and 5.19 which illustrate the Palmqvist fracture toughness for the 0.4 and the 0.8wt% vanadium carbide ultrafine alloys respectively.

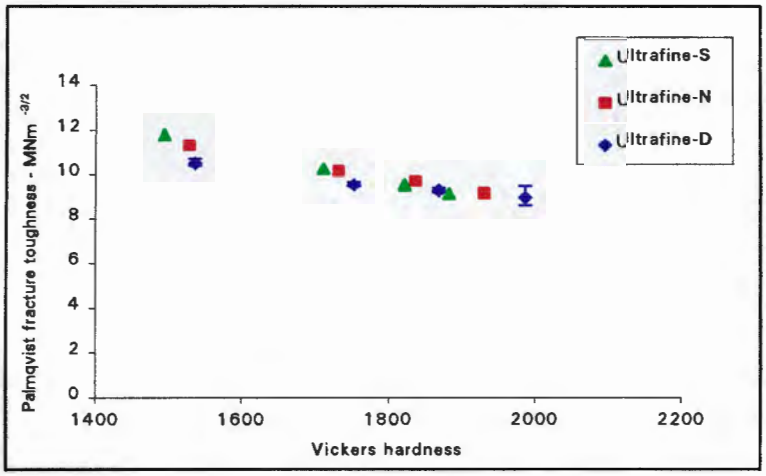

Figure 5.18 *Comparison of the Palmqvist fracture toughness for the 0.4wt% vanadium carbide ultrafine alloys.*

The Palmqvist toughness values for the 0.4wt% VC grades are similar at similar cobalt contents. This equality decreases as the cobalt content increases. At 15wt% cobalt there is approximately a 1.3MNm$^{-3/2}$ difference between grades US154 and UD154, while at 6wt% cobalt the largest difference is only about a 0.2MNm$^{-3/2}$ between grades UD64 and US64.

The slopes of fracture toughness with hardness for the different hardmetals, S, N and D are slightly different. The S-grade slope is slightly steeper than the N-grade slope which is slightly steeper than the D-grade slope which implies that the toughness of the different grades also change differently with an increase in hardness and decrease in cobalt. The behaviour of the 0.8wt% VC grades, shown in figure 5.19, is different to that of the corresponding 0.4wt%VC grades.

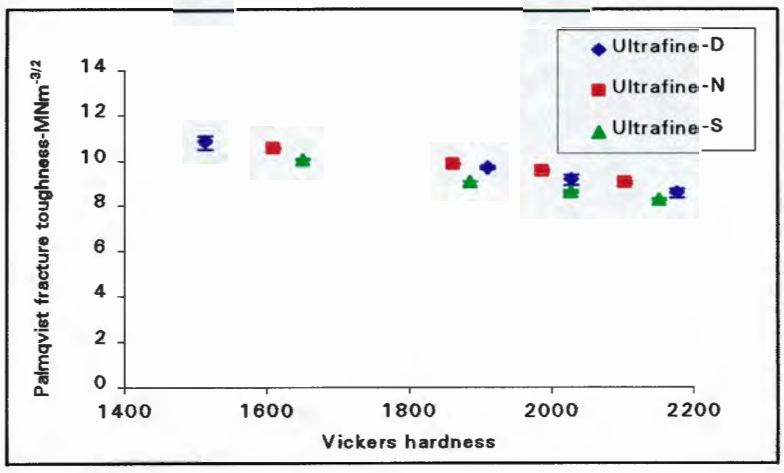

Figure 5.19 *Comparison of the Palmqvist fracture toughness for the 0.8wt% vanadium carbide ultrafine alloys.*

The change in toughness with hardness for the three different hardmetals, S, N and D appear to be the same, which implies that the toughness behaviour for these alloys is similar. At similar cobalt contents, the difference between the grades is approximately 0.75MNm$^{-3/2}$ across the range of alloys tested.

The only difference observed between the grades is that at hardness values above 1800 Vickers, the UN grades have higher toughness values than the other two grades at similar cobalt contents. Below 1800 Vickers hardness, the UN grade has a toughness value between that of the UD and US grades.

The six different sets of ultrafine alloy fracture toughness values are illustrated in figure 5.20. It is worth noting that the toughness values of the ultrafine alloys all lie within a 2 MNm$^{-3/2}$ scatter band.

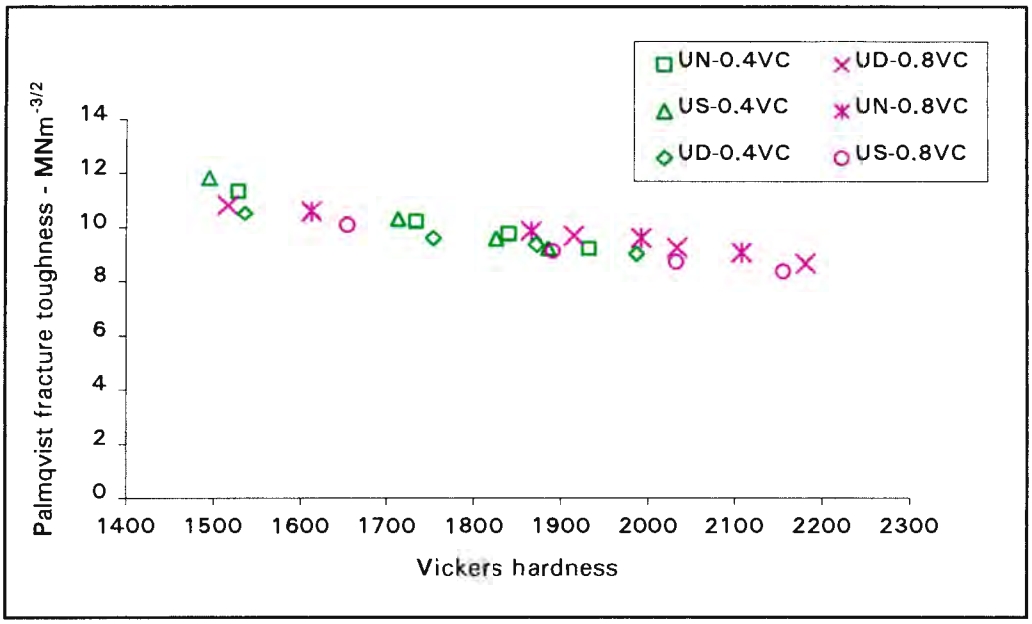

Figure 5.20 *Palmqvist fracture toughness for the ultrafine hard metals.*

Chapter 6

RESULTS:

SHORT ROD FRACTURE TOUGHNESS

6.1 INTRODUCTION

This chapter sets out the results of toughness testing conducted on the WC-Co alloys using the Short Rod fracture toughness test method. A Terra Tek Fractometer machine was used to determine the toughness values of each specimen. The test method involves the placement of the specimen over a mercury bladder and applying a force to the mercury. This initiates a crack in the specimen. As the force is increased, the crack grows until the specimen fractures. Toughness measurements are automatically determined by the Fractometer.

The influence of vanadium carbide, cobalt content and hardness on the short rod fracture toughness are also presented. The ultrafine grades made via the three different powder routes are compared and finally their results are compared to those of conventional cemented carbides.

The results in this chapter are described as follows:

1) Short Rod fracture toughness test results
2) Microscopic studies of the fracture surfaces
3) Comparisons between the Short Rod and the Palmqvist test results of the ultrafine alloys.

6.2 SHORT ROD FRACTURE TOUGHNESS TESTS

Table 6.1 lists the results of short rod fracture toughness testing carried out on hard metals with four different types of carbide grain size distributions. These results are illustrated in figure 6.1.

Table 6.1 *Short rod fracture toughness for a series of hard metals with varying carbide grain size distributions.*

Grade	wt% Cobalt			
	6	*8*	*10*	*15*
UD8	8.1 ±0.29	8.3 ±0.64	9.9 ±0.59	11.6 ±0.44
FB	10.4 ±1.01	11.3 ±1.03	11.9 ±0.71	14.1 ±1.01
MB	11.8 ±0.59	13.4 ±0.62	13.9 ±0.45	16.8 ±0.88
CB	16.9 ±0.22	17.3 ±0.33	19.4 ±0.12	23.6 ±0.32

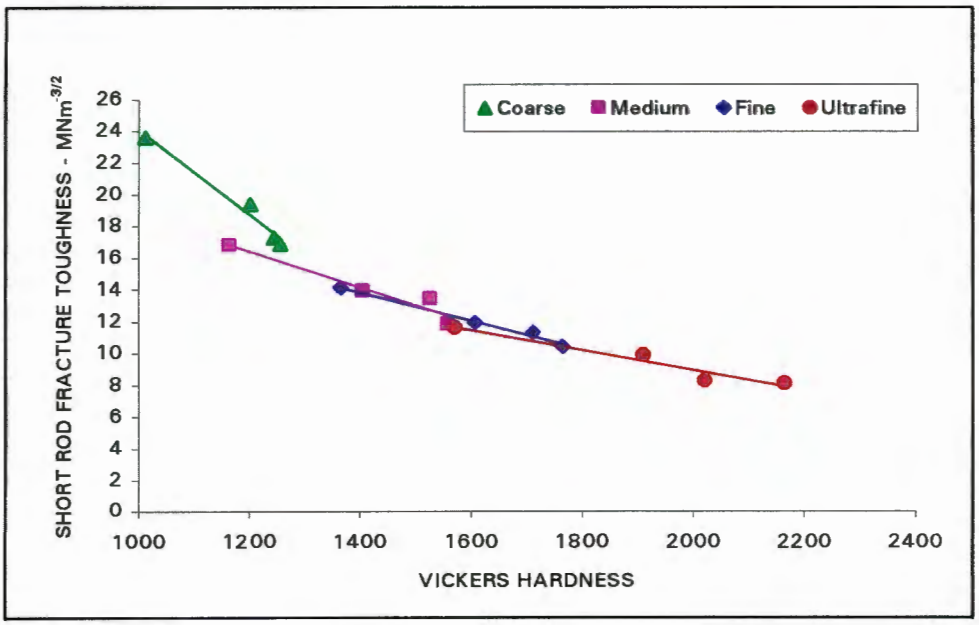

Figure 6.1 *Short Rod fracture toughness of a series of cemented carbides.*

The toughness for each grade shows a linear decrease with an increase in the hardness. Each set of hard metals show a deviation in some of the data points from the linear relationship. The coarser grained metals have the highest toughness values, while the ultrafine materials show the lowest fracture toughness data. As the carbide grain size decreases, the slope of the respective linear relationship between toughness and hardness becomes more gradual. Thus the toughness decreases more rapidly in the coarser grained hard metals. This trend was seen previously in the Palmqvist test data.

For the CB alloys, there is about a 6.5MNm$^{-3/2}$ decrease in toughness over a 240 Vickers hardness range. With the UD8 alloys there is approximately a 2.3MNm$^{3/2}$ decrease in toughness over a hardness range of 590 Vickers. Thus, the decrease in toughness for the ultrafine grades is approximately 33% that of the coarse grained metal's toughness. However, the hardness range over which this change occurs in ultrafine-grained alloys is about 250% greater than that in the coarser grained alloys.

During the Short Rod testing of the ultrafine alloys the mercury bladder of the Terra Tek machine ruptured and could not be replaced. Thus an incomplete set of results has been obtained for the Short Rod fracture toughness. These are shown in table 6.2 for the ultrafine alloys and the errors shown in the table represent one standard deviation.

Table 6.2 *Short rod fracture toughness for the ultrafine alloys.*

Grade	wt% VC	wt% Cobalt			
		6	*8*	*10*	*15*
UD	0.4	8.30 ±0.28	9.59 ±0.42	9.55 ±0.31	-
UD	0.8	8.11 ±0.29	8.25 ±0.64	9.88 ±0.59	11.60 ±0.44
UN	0.4	8.94 ±0.20	9.01 ±0.12	10.21 ±0.31	10.72 ±0.35
UN	0.8	8.74 ±0.51	8.90 ±0.71	-	9.18 ±0.94
US	0.4	-	8.88 ±0.20	9.37 ±0.28	9.67 ±0.21
US	0.8	-	9.16 ±0.73	9.44 ±0.46	10.01 ±0.81

The results shown in table 6.2 are illustrated graphically in figures 6.2 and 6.3. These two figures show the relationship between fracture toughness and hardness for the 0.4 and 0.8wt% vanadium carbide grades respectively. The grades display similar toughness results which range between 8 and 10MNm$^{-3/2}$, with a few alloys having toughness data above 10MNm$^{-3/2}$.

The standard deviations of the Short Rod test results are approximately double that obtained using the Palmqvist test. A possible reason for this difference is that only 5 to 6 Short Rod samples, per grade, were tested and only one reading per sample is obtained. In the Palmqvist test over 50 measurements were made using 5 to 6 specimen per grade.

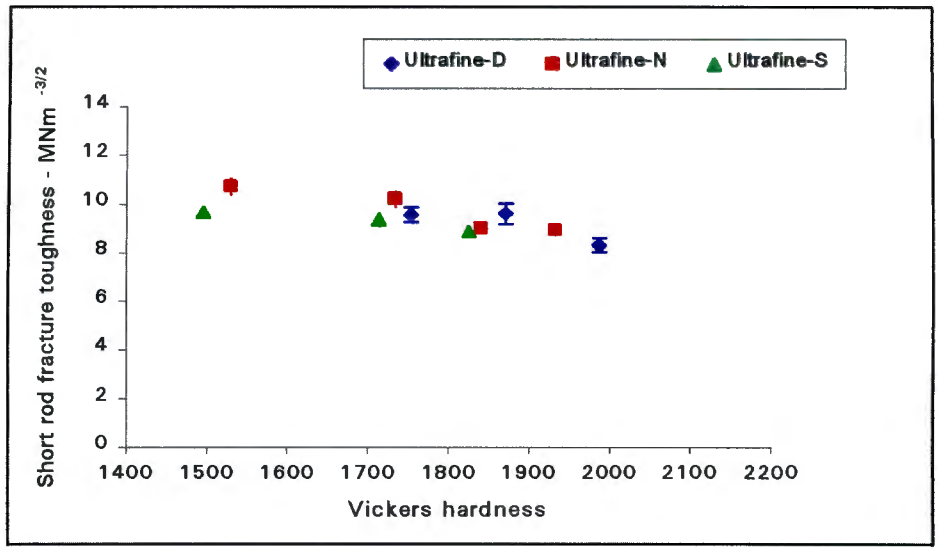

Figure 6.2 *Short Rod fracture toughness for the 0.4wt% vanadium carbide ultrafine alloys.*

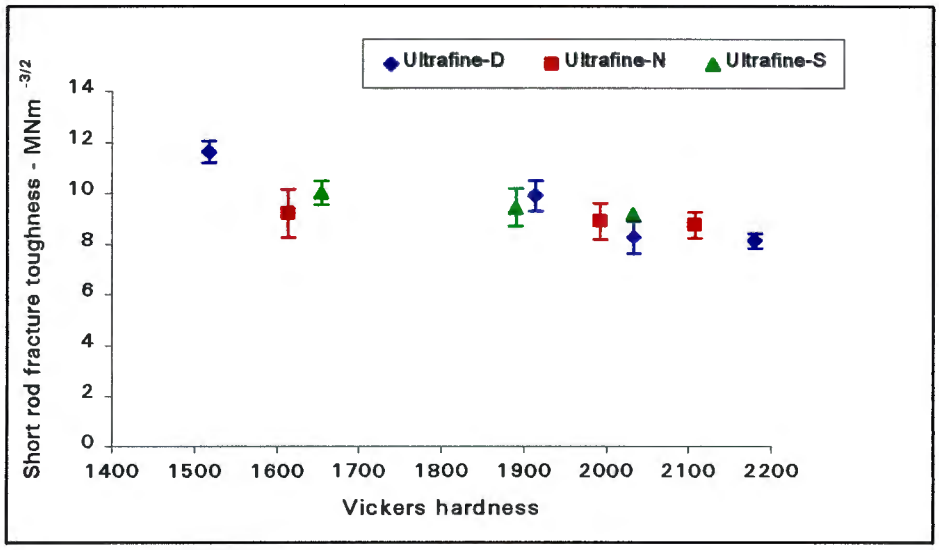

Figure 6.3 *Short Rod fracture toughness for the 0.8wt% vanadium carbide ultrafine alloys.*

From figures 6.2 and 6.3 it is difficult to predict trends for the individual grades. However by combining the results for all the ultrafine hard metals, figure 6.4 shows that all the Short Rod fracture toughness values lie within a scatter band of $2MNm^{-3/2}$. This is approximately similar to that of the Palmqvist fracture toughness scatter band shown in figure 5. 20. Comparisons between the two different fracture toughness tests will be discussed in section 6.3.

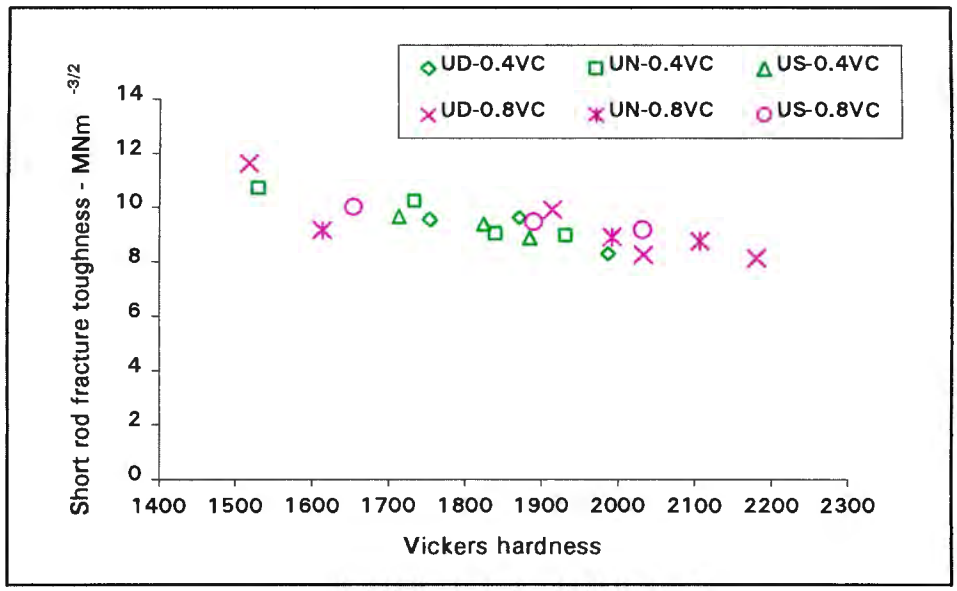

Figure 6.4 *Short Rod fracture toughness for all the ultrafine cemented carbides.*

6.2 FRACTOGRAPHY

Microscopic studies were carried out on the fracture surfaces using electron microscopy. Figure 6.4 is a schematic of a fractured specimen showing the different regions that were examined. The effects of the slotting procedure used to cut the specimen into the correct testing size is emphasized in some of the micrographs.

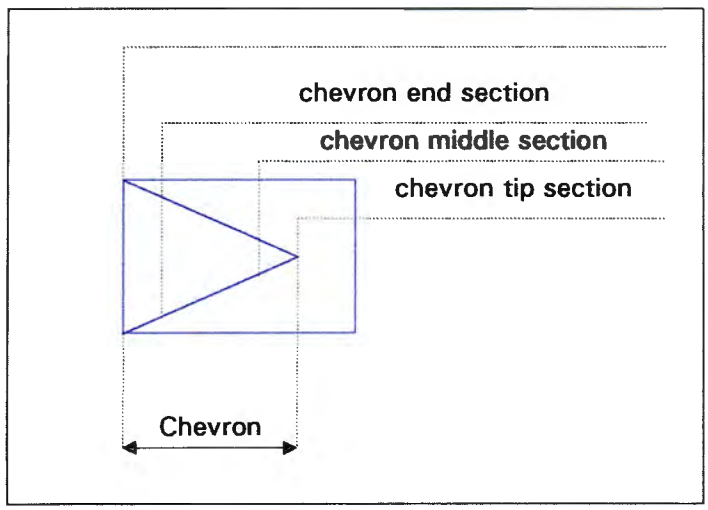

Figure 6.4 *Schematic of the fractured Short Rod specimen.*

Figure 6.5 shows the fracture appearance at the chevron tip. The surface is fairly coarse and a few holes can be seen. On either side of the chevron tip, are two strands of hardmetal that are white in color and are identified by arrows. These hardmetal strands were probably left on the surface when the specimen was cut into shape prior to fracture toughness testing. Longitudinal machine marks of the cutting tool are still visible along the side of the chevron.

Figure 6.5 *SEM micrograph showing the general appearance of the fractured chevron tip observed in some of the hard metals.*

Figure 6.6 shows a close-up view of one side of a chevron tip. Sections of hardmetal can be seen to have been extruded out of the side. These extrusions are exiting from the cutting machine lines and are probably due to the abrading/rubbing action of the cutting blade. Prior to toughness testing an attempt is made to clean out the debris in the specimen slots using filter paper soaked in machine oil. Figure 6.6 shows an unsuccessful cleaning attempt.

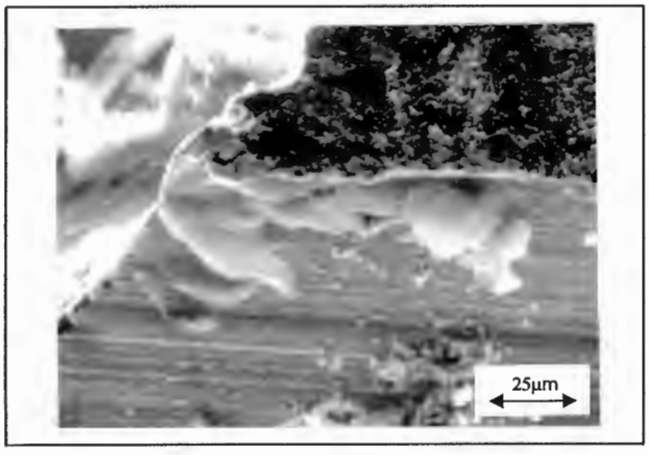

Figure 6.6 *SEM micrograph depicting cobalt extrusions from the machine marks on the side of the chevron tip.*

Figure 6.7 shows the most typical appearance of the specimen surface found in the majority of the hard metals. No cobalt extrusions are visible and very few particles of cobalt are actually visible on either side of the chevron tip. This is due to correct cleaning of the specimen slots.

The fracture surface of this specimen is very uneven and a huge hole is visible at the very end tip of the chevron. This suggests that at the beginning of the test there must have been a defect in the path of the advancing crack. Thus as the crack advanced this defect probably caused a large section of material to dislodge.

Some fine cracks were also visible on the fracture surfaces in this tip region. The overall fracture surface appearance, which is glassy, shows striations and fracture mirrors, which is indicative of brittle fracture.

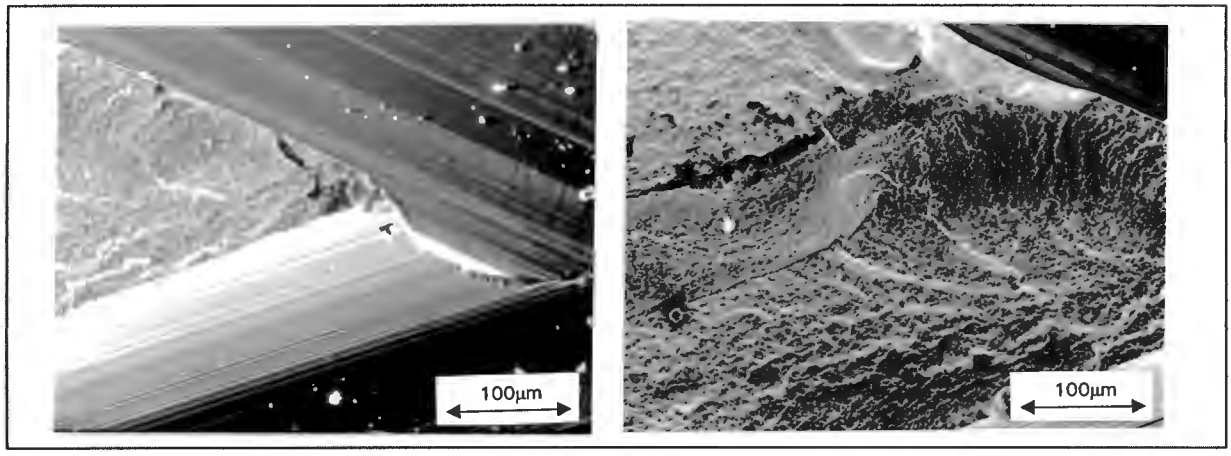

Figure 6.7 *SEM micrograph depicting the most common type of fracture surface found in the alloys.*

A few of the fracture toughness tests did not proceed perfectly and figure 6.8 illustrates two examples where problems occurred during testing. The toughness values from these tests were discarded. In the micrograph on the left, the entire front section of the chevron tip had broken away during testing. In the micrograph to the right, small sections of the tip had also been broken away, but more noticeable were ridges scattered around the tip. On the front side of these ridges, extensive smearing of the grains was noted as well as black regions of excess carbon. There are also some large holes present in the chevron sides. These are either open porosity in the specimen or the slotting machine might have "chipped" some of the material during cutting.

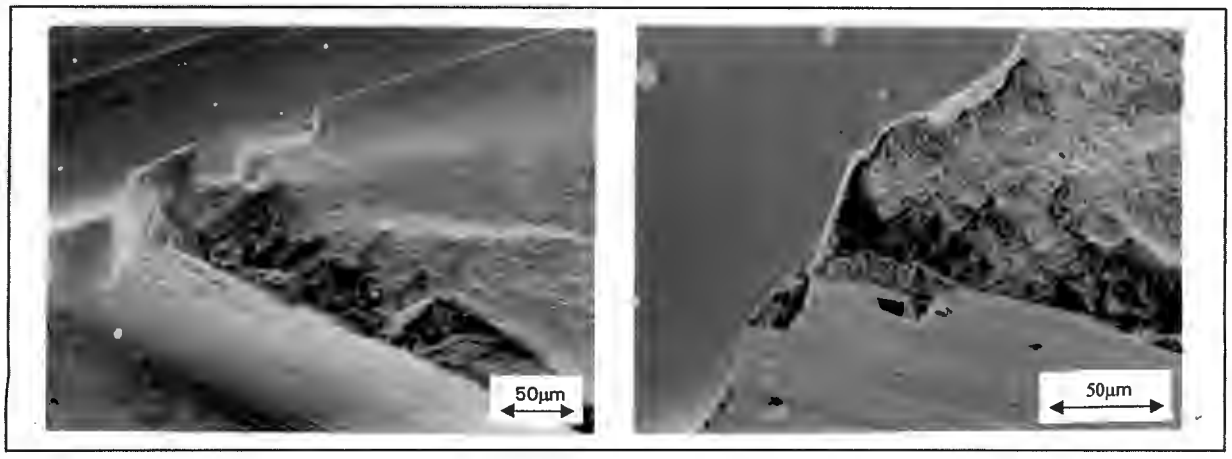

Figure 6.8 *SEM micrographs showing broken chevron tips as a result of testing problems.*

The following figures illustrate the three different regions of the chevron fracture in more detail. The three regions are *tip, middle* and *end* as shown in figure 6.4.

In figure 6.9, the fracture surfaces at the tip region are shown for two different alloys. The micrograph on the left represents a 0.8wt% vanadium carbide-15wt% cobalt UD alloy while the one on the right is a 0.8wt% vanadium carbide-6wt% cobalt UN grade. The main crack path is observed in alloy UD158. Small ridges are also visible. In alloy UN68, many small holes are found across the surface. These represent areas that were previously occupied by tungsten carbide grains, which were removed during fracture. By comparing the two micrographs, it can be seen that the surface of the 15wt% cobalt grade is smoother than that of the 6wt% cobalt alloy. Therefore the more cobalt present, the less brittle the fracture appearance.

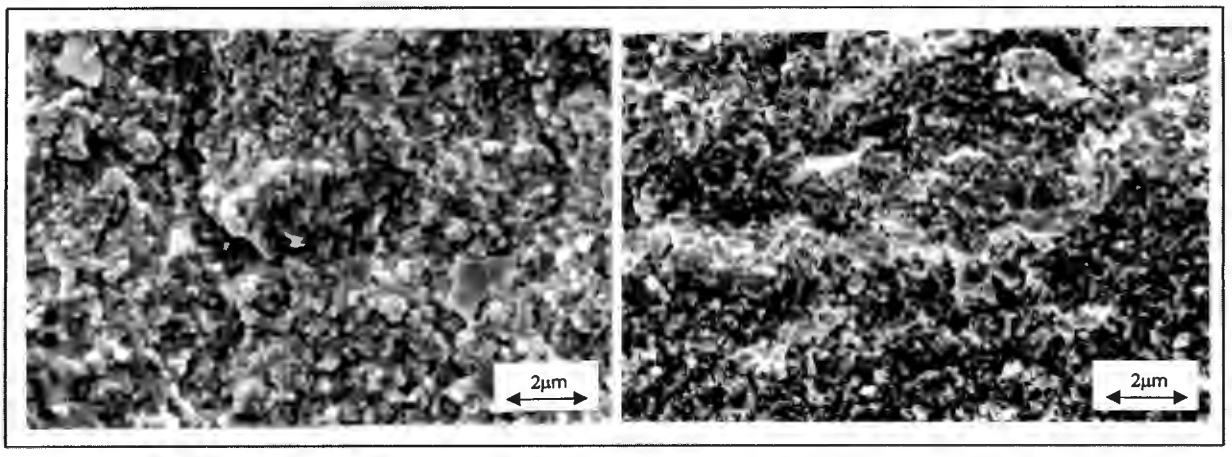

Figure 6.9 *SEM micrographs comparing the chevron tip fracture surfaces of a 15(left) and a 6wt%(right) cobalt alloy respectively.*

The micrographs in figure 6.10 show regions of smearing in the vicinity of the tip section in grade UN154. Note that the two micrographs were taken at different magnifications. Black carbon regions can also be seen in the micrograph on the right as well as a ridge on the top section of the photo.

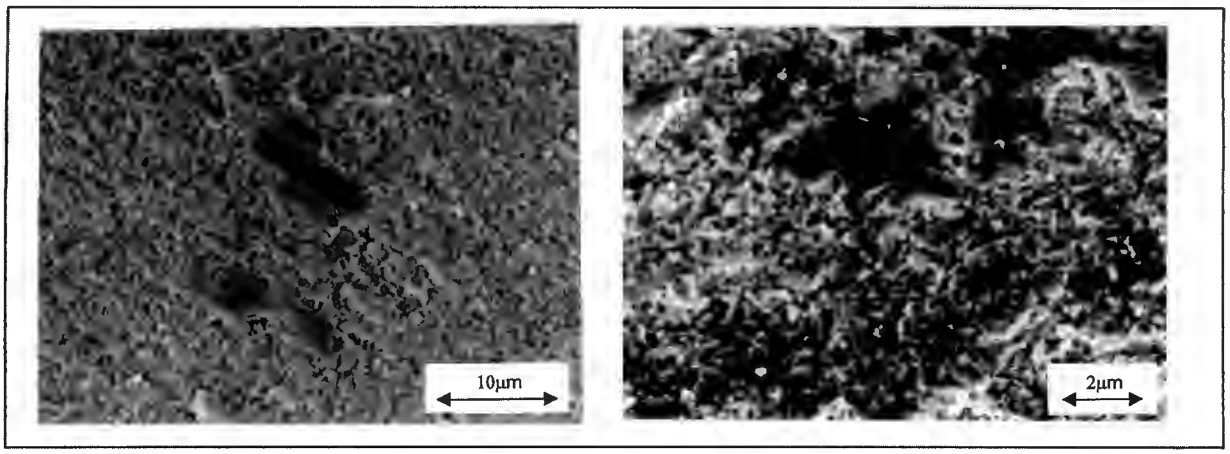

Figure 6.10 *SEM micrographs of grade UN64 showing smearing of the grains in the tip region.*

Huge depressions and loose grains were also observed in the tip region and figure 6.11 illustrates two examples in which these features were found. The micrograph on the left represents a medium grained 6wt% cobalt MB grade, and the one on the right depicts an ultrafine grained 6wt% cobalt UN grade. The depressions are deeper in the coarser grained hard metals than in the finer grained ones. There were also more loose carbide particles noted on the fracture surfaces of the coarser grained alloys than the finer grained ones. The majority of the carbide grains were unbroken which is evidence that fracture in cemented carbides proceeds preferentially through the binder phase.

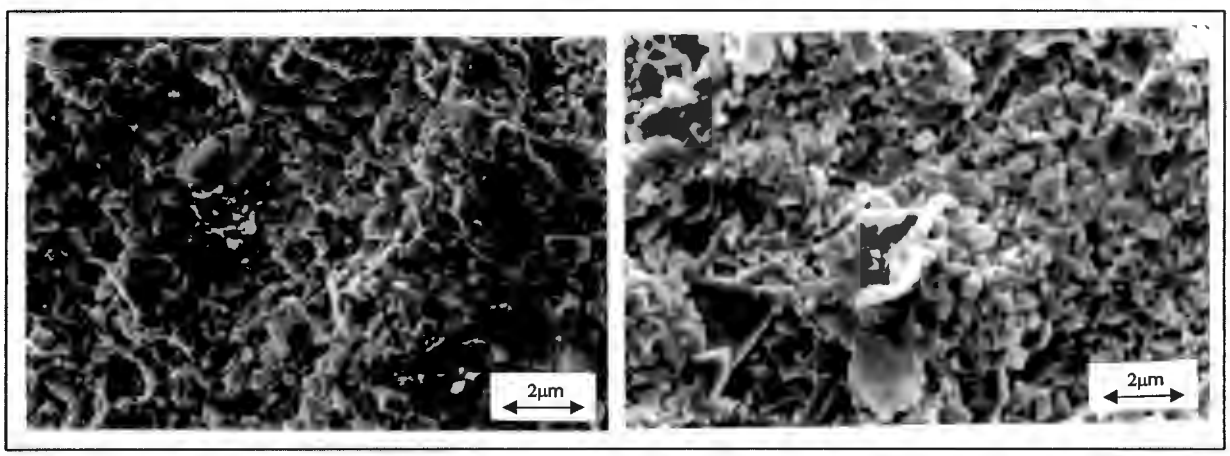

Figure 6.11 *SEM micrographs showing depressions and loose particles on the fractured tip region in a medium-grained(left) and an ultrafine-grained(right) hardmetal.*

The fracture surfaces in the coarse grained CB grades were very different compared to the other alloys. A larger proportion of the carbide grains had broken during the fracture process. Figure 6.12 shows the fracture appearances of a 6wt% cobalt CB hard metal taken at the tip region. Arrows in the figure indicate cracks in some of the carbide grains. It is clear which grains have been broken as evidenced by the "step marks" on some of them, which is also indicated by arrows in the figure.

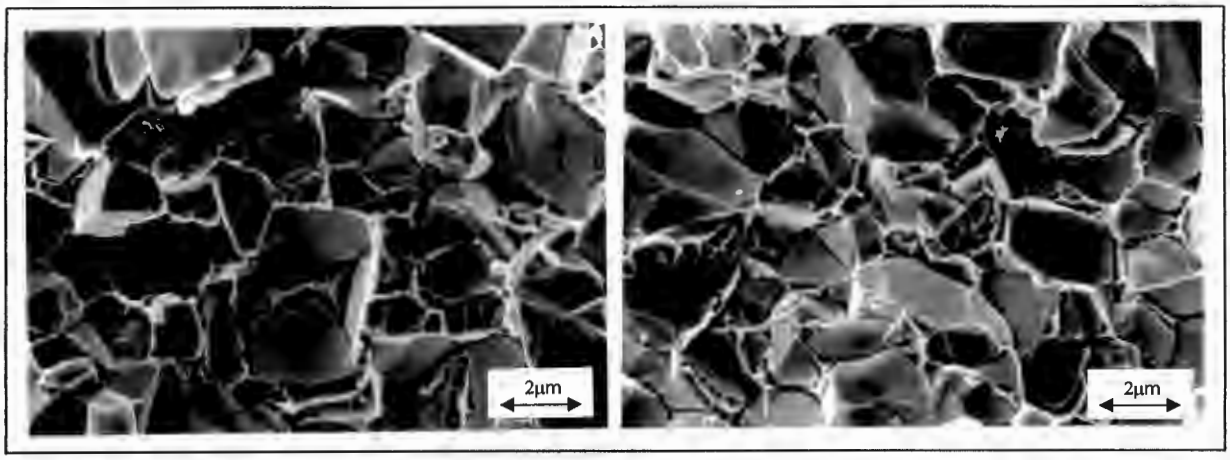

Figure 6.12 *SEM micrographs showing the fracture at the tip region in a coarse grained 6wt% cobalt CB alloy.*

The middle region of the chevron showed very flat fracture surfaces in all the grades. Thus, crack growth was fairly constant in this section of the specimen. Figure 6.13 shows this middle region for two different alloys, namely grades, (left) UD154 and (right) MB6. In alloy UD154, holes were found, showing that grains were pulled out of this section. Alloy MB6 shows a fairly even fracture surface, with no evidence of smearing, but cleavage areas were visible.

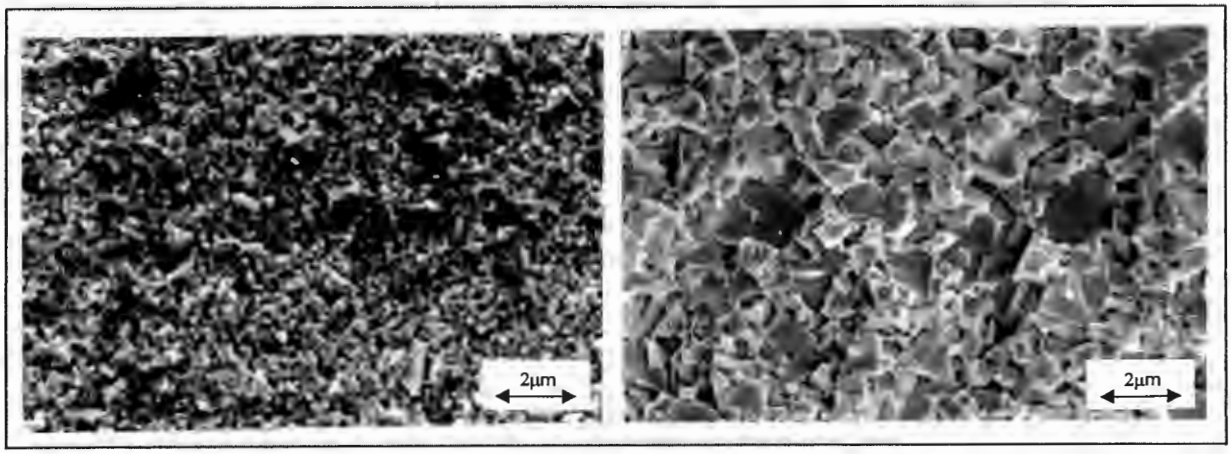

Figure 6.13 *SEM micrographs showing the fracture surfaces in the middle region of the chevron in various alloys.*

The end section of the chevron showed very brittle fracture surfaces, more so than found in the rest of the chevron. This indicates that fast fracture occurred in this region since the critical load is reached as the crack advances towards the end of the specimen. Figure 6.14 shows some of the end regions in four different alloys, namely, (a) UN68, (b) UN64, (c) US88 and (d) CB6. Alloy UN68 shows an extremely flat fracture surface which is unusual. There is also a lot of cobalt debris on the surface of this specimen and a few holes.

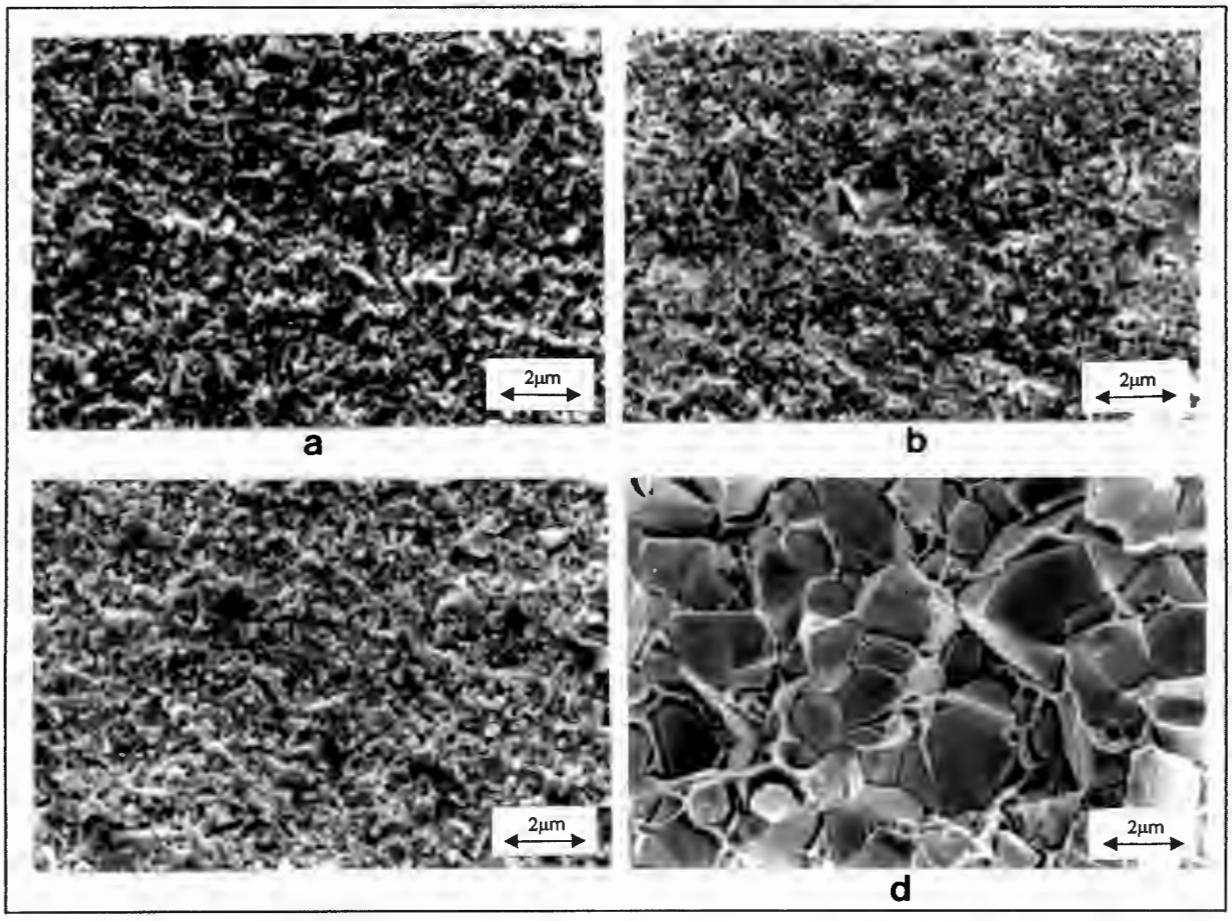

Figure 6.14 *SEM micrographs showing the fracture appearance at the end region of the chevron for four different cemented carbides.*

Grade UN64 illustrates the fracture surface found at the end region in most of the alloys which is generally very rough. However, the depressions and ridges are small and consistently spread around the section on matching fracture surfaces. The 8wt% cobalt grade US88 showed a few areas of smeared grains, but these were not a common feature on the specimen. The fracture surface in this alloy was also fairly consistent with respect to depressions and ridges. No "crack-steps" were visible in the coarse grained CB alloy as was previous observed at the tip region. The carbide grains show very smooth breaks, with very few exceptions, which confirms that fast fracture occurred in this region of the chevron.

6.3 COMPARISON OF THE SHORT ROD AND PALMQVIST FRACTURE TOUGHNESS TESTS

The fracture toughness results obtained using the Short Rod test will now be compared to the results obtained using the Palmqvist fracture toughness test. Though the Short Rod test data showed more scatter the average toughness for each grade was similar to the average toughness value measured using the Palmqvist tests. There are a few exceptions to this trend and these will be highlighted in the following sections.

By comparing the results obtained for the coarser-grained cemented carbides, namely the FB, MB and CB grades, it was found that the Short Rod toughness data is higher than that of the Palmqvist data across the range of grades tested. There is a difference of approximately 2MNm$^{-3/2}$ separating the two different test results and this is illustrated in figure 6.15.

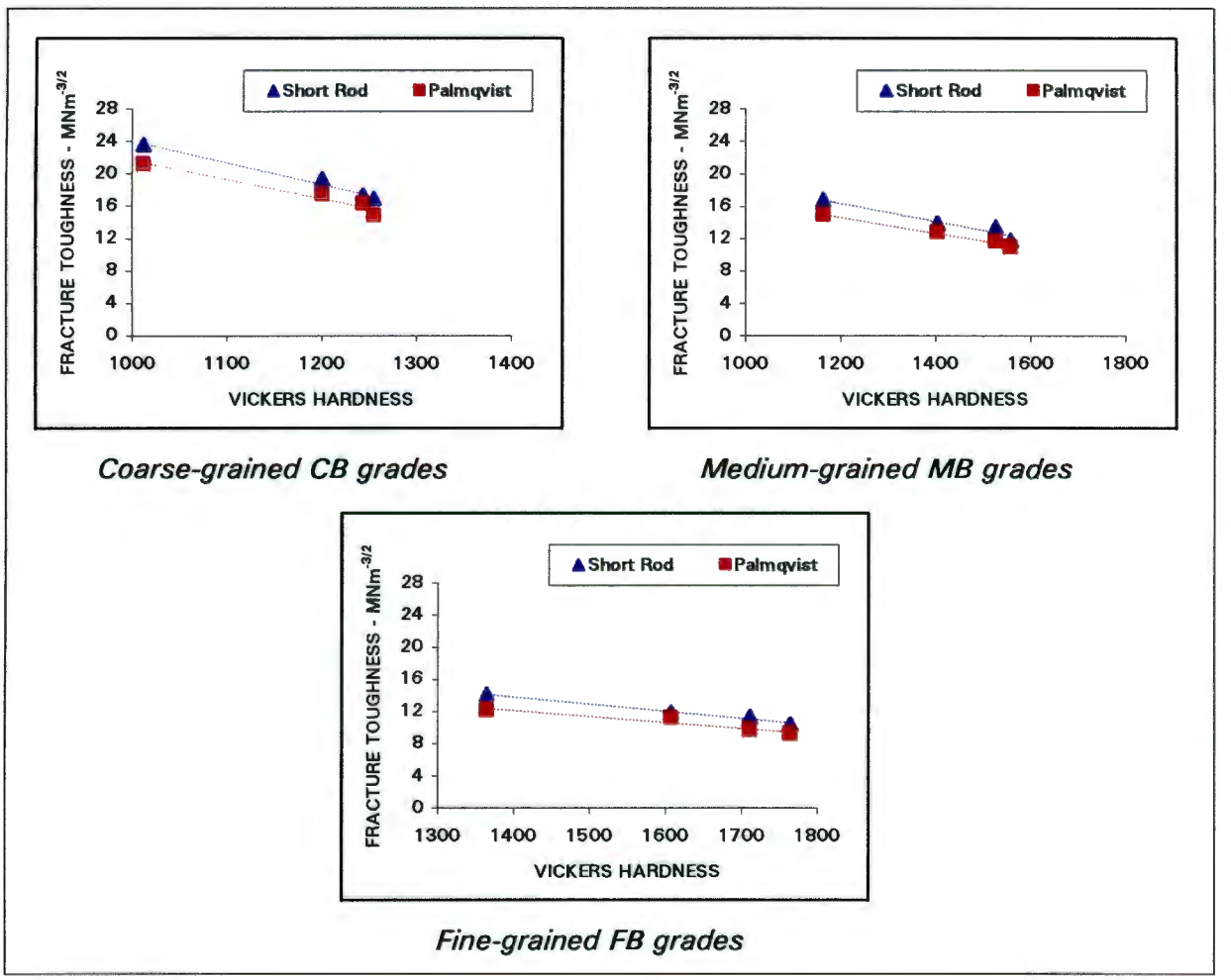

Figure 6.15 *Comparison of the Short Rod and Palmqvist fracture toughness test results for the coarser-grained cemented carbides.*

In contrast to the coarser grades, the results obtained for the ultrafine grades using the two different toughness tests are similar. In general, the data obtained with the Palmqvist test is higher than that obtained using the Short Rod test. This behavior is shown in figure 6.16 for the six ultrafine grades where the dotted lines represent the trends followed by each test.

The differences between the two toughness tests is minimal for the 0.4wt% vanadium carbide UD grades, as well as for the 0.8wt% vanadium carbide UD and US grades. A larger difference between the results, obtained using the two tests, is noticed for the 0.4wt% vanadium carbide UN and US grades and also for the 0.8wt% vanadium carbide UN alloys. The 0.4wt% vanadium carbide US grades show the largest difference in results between the Short Rod and the Palmqvist tests.

For the 0.4wt% vanadium carbide UD alloys, it is unfortunate that Short Rod test results could not be obtained for the 15% cobalt grade. These results would be useful to show whether the Short Rod trend line crosses the Palmqvist trend line at around 1700 Vickers hardness or if they both lie parallel to each other, with the Palmqvist line above the Short Rod line. In the 0.8wt% vanadium carbide UD grades, the Short Rod test results for the 15wt% cobalt grade lie above those obtained using the Palmqvist test and the two tests' trend lines cross each other at a hardness of approximately 1700 Vickers.

In the UN grades the Palmqvist results are slightly higher than the Short Rod test results. At low hardness values the difference is negligible, but as the hardness increases, it appears as though the difference between the two tests' results increases. However, due to the limited Short Rod test data obtained the above statement is merely an assumption. It also appears as though the 0.8wt% vanadium carbide UN grades show a greater difference in the two tests' results compared to the 0.4wt% vanadium carbide results.

The US grades show the reverse trends to those observed in the UN grades. There is a larger difference between the Short Rod and Palmqvist test results obtained for the 0.4wt% vanadium carbide US grades compared to those measured for the 0.8wt% vanadium carbide grades. In the 0.4wt% vanadium carbide US grades, the Palmqvist test data is higher than the Short Rod test data at all hardness levels tested. However, there is no clear distinction between the results of the two tests for the 0.8wt% vanadium carbide US grades.

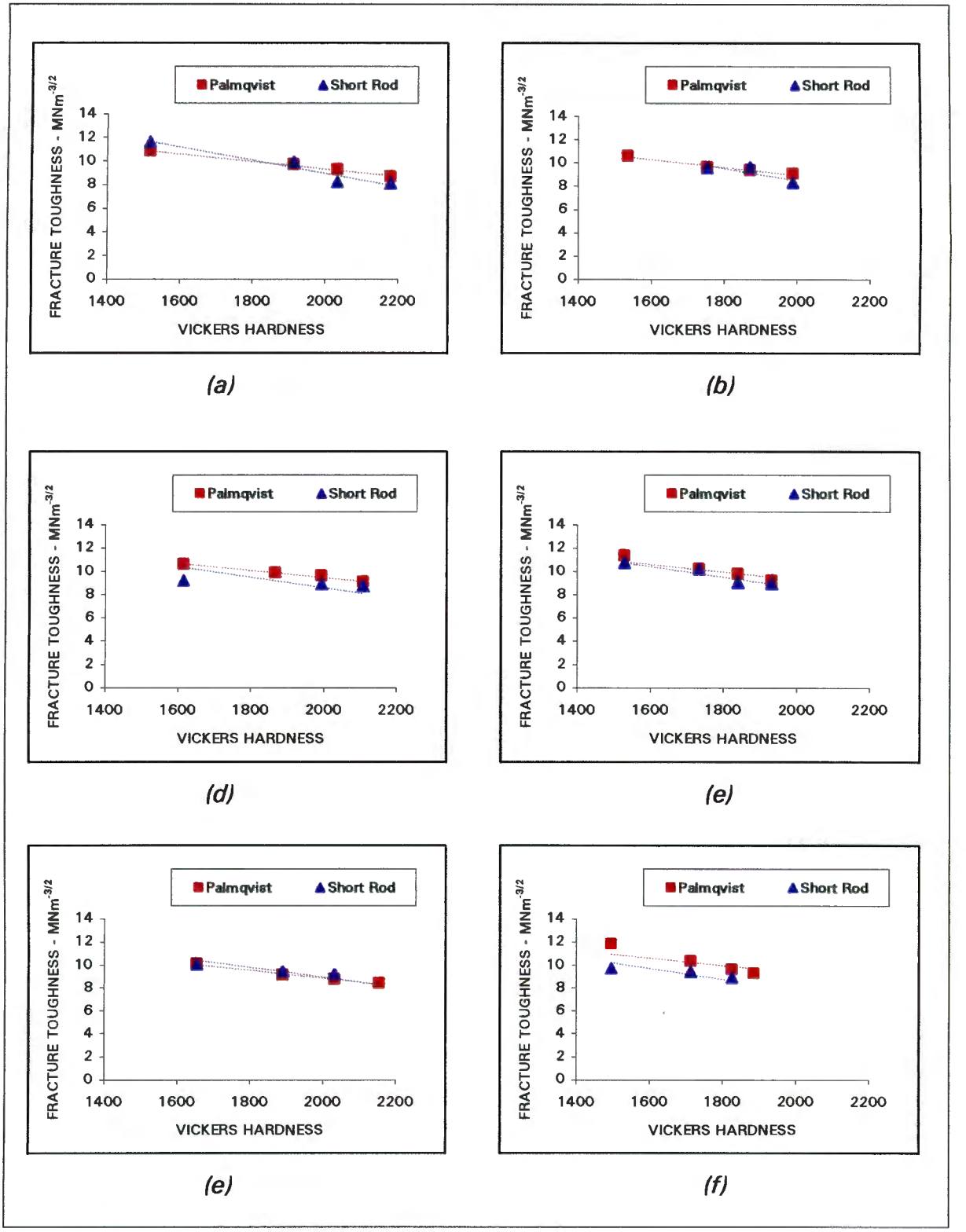

Figure 6.16 *Comparison of the Short Rod and Palmqvist fracture toughness test results for the ultrafine hard metals.*

(a) 0.8wt% vanadium carbide UD grades; (b) 0.4wt% vanadium carbide UD grades

(c) 0.8wt% vanadium carbide UN grades; (d) 0.4wt% vanadium carbide UN grades

(e) 0.8wt% vanadium carbide US grades; (f) 0.4wt% vanadium carbide US grades

Chapter 7

DISCUSSION

7.1 INTRODUCTION

The search for tool materials providing excellent wear resistance has led to the development of cemented carbides with fine carbide grain sizes produced from nanostructured powders. Hardmetals produced from these nanostructured powders have wear resistances 2-6 times greater than hardmetals made from fine-grained powders[10]. The improved mechanical properties generated by the ultrafine-grained carbide microstructures has led to an increase in tool productivity.

Although these ultrafine grades show a marked increase in hardness, their toughness is also of importance in many applications. It is generally believed that the higher the hardness of the composite, the lower the fracture toughness, and vice versa. However, this relation is not this simple since other factors play an important role in determining the resultant properties of hardmetals. Parameters such as sintering temperature, sintering time and the microstructure parameters of the respective alloys must be taken into account for obtaining optimal hardness-toughness combinations.

In this chapter, the fracture toughness of a range of cemented carbides is discussed with respect to the effect of hardness and microstructural parameters. These effects are first considered with respect to the differences in toughness behavior observed between ultrafine cemented carbides and conventional coarse-grained hard metals. Following on from this, the fracture toughness behavior of ultrafine alloys produced via three different powder routes are compared. Finally, the merits of the two fracture toughness tests used during this work are discussed.

7.2. FRACTURE TOUGHNESS OF WC-Co ALLOYS

The overall toughness of cemented carbides are controlled by the strength and deformation characteristics of the carbide as well as the binder phase. Strength characteristics are generally controlled by the mechanisms of plastic deformation in addition to crack initiation and propagation. The plastic work involved in stretching and rupturing the cobalt binder phase during fracture is responsible for a large part of the alloy's toughness. It has been found that in low cobalt alloys, fracture occurs predominantly by the rupture of the Co/WC interlayer, whilst at high values of cobalt content, tungsten carbide grain cleavage takes place, presumably via the dislocation pile-up stress generated by the plastic deformation in the binder[182,183].

The above statements can be explained by examining the crack propagation in the Palmqvist and Short Rod tests. The cobalt-based binder phase is a heavily faulted, face centred cubic structure with a high dislocation density which increases with increasing cobalt content. The dislocation density probably arises from deformation introduced during milling of the powders and this deformed structure has partly survived the sintering process. In the initiation stage of crack propagation, deformation and dislocation interactions in the cobalt phase cause microcracking in the specimen. Some of these microcracks were noted during SEM examination of the fractured specimen.

Microcrack formation is followed by macrocracking, where the cobalt phase form ligaments across the crack faces as shown in figure 7.1. Figure 5.13(b) shows a cobalt ligament bridging the crack path. As the applied stress increases the cobalt phase undergoes plastic deformation, the amount of which depends on the width of each ligament. As the ligament deforms, voids form in the ligament. Plastic deformation of the binder is severely constrained as long as the surrounding carbide skeleton remains intact. This causes the dislocations to pile up against the rigid carbide crystals along the crackline. This piling up generates a large amount of stress, which eventually causes deformation and/or cleavage to occur in the tungsten carbide grains alongside the crack path.

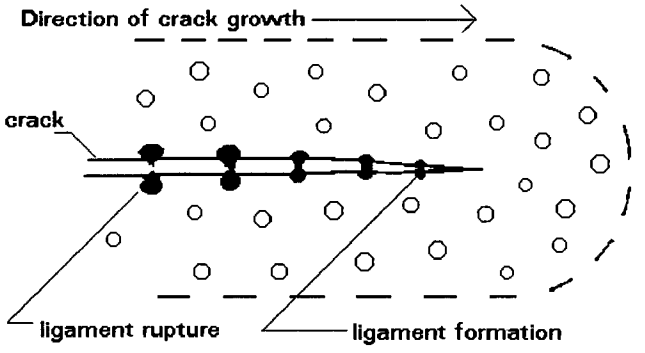

Figure 7.1 *Plastic deformation in hardmetals. (adapted from reference 78)*

Roebuck and Almond[21] showed that the ability of the tungsten carbide to sustain plastic deformation was probably due to the operation of slip systems in tungsten carbide grains. The slip planes are of the {1010} type with slip directions <1120>, <1123> and <0001>. They provide five independent systems necessary to produce the shape changes required to maintain continuity within the microstructure.

Eventually stresses caused by the dislocations generated in the cobalt phase result in cracking inside or along carbide particles. As the ligaments are stretched until fracture occurs in the chisel-edge mode, strain hardening will cause a further increase of flow stress. When a carbide grain adjacent to the binder region cracks, highly localized deformation of the binder occurs under a state of plane strain. As the crack advances a steady state zone is formed within which the ligaments bridging the crack pass through all stages of stretching up to final failure.

The crack path was seen to proceed preferentially through the binder phase of the ultrafine alloys, as shown in figures 5.11, 5.12(a) and 5.12(c). The majority of the carbide grains along the carbide grains are unbroken as the crack circumvents them. However, in the coarser-grained cemented carbides, more carbide grains were found to fracture as the crack proceeded through the carbide grains rather than through the binder phase as shown in figure 5.13(a). This observation has been found by several researchers[101-104].

The dominant influence on the toughness of the hardmetals is related to deformation and cracking in both the carbide matrix and in the cobalt ligaments. However, the limiting value of hardmetal toughness is related primarily to the shear stress of the binder phase. Thus the choice of binder composition is vital if greater toughness values are to be achieved.

7.3 COMPARISON OF THE FRACTURE TOUGHNESS BETWEEN ULTRAFINE AND CONVENTIONAL CEMENTED CARBIDES

In this study the fracture toughness of a series of cemented carbides has been determined using the Palmqvist Indentation and Short Rod methods. The cemented carbides represent four different types of tungsten carbide grain size distributions namely, ultrafine-grained (UF), fine-grained (F), medium-grained (M) and coarse-grained (C).

The primary variables controlling the fracture toughness of cemented carbides have been shown to be the thickness of the binder phase layers[91,108-113] and microstructural effects due to the carbide particle size[91,93.112].

Figure 7.2 shows the relationships between the cemented carbides with varying carbide grain size distributions with respect to the Palmqvist fracture toughness, hardness, binder mean free path and tungsten carbide grain size. The graphs on the left-hand side represent the relationship between toughness and hardness for a specific range of cobalt, with the bar graphs depicting the toughness. The graphs on the right-hand side reflect the binder mean free path and carbide grain size for the corresponding cobalt ranges, with the bar graphs representing the binder mean free path.

From these figures it is noted that a decrease in the carbide grain size from coarse to ultrafine is associated with:

- a decrease in toughness
- an increase in hardness
- a decrease in binder mean free path

By comparing the toughness of different hardmetal grades at a constant hardness level a significant difference is noticeable between the highest and the lowest obtainable toughness values at a specific hardness. In addition, by comparing these figures to figure 5.14 it appears that the hardness to fracture toughness relationship of individual alloys varies with changes in composition and/or microstructure.

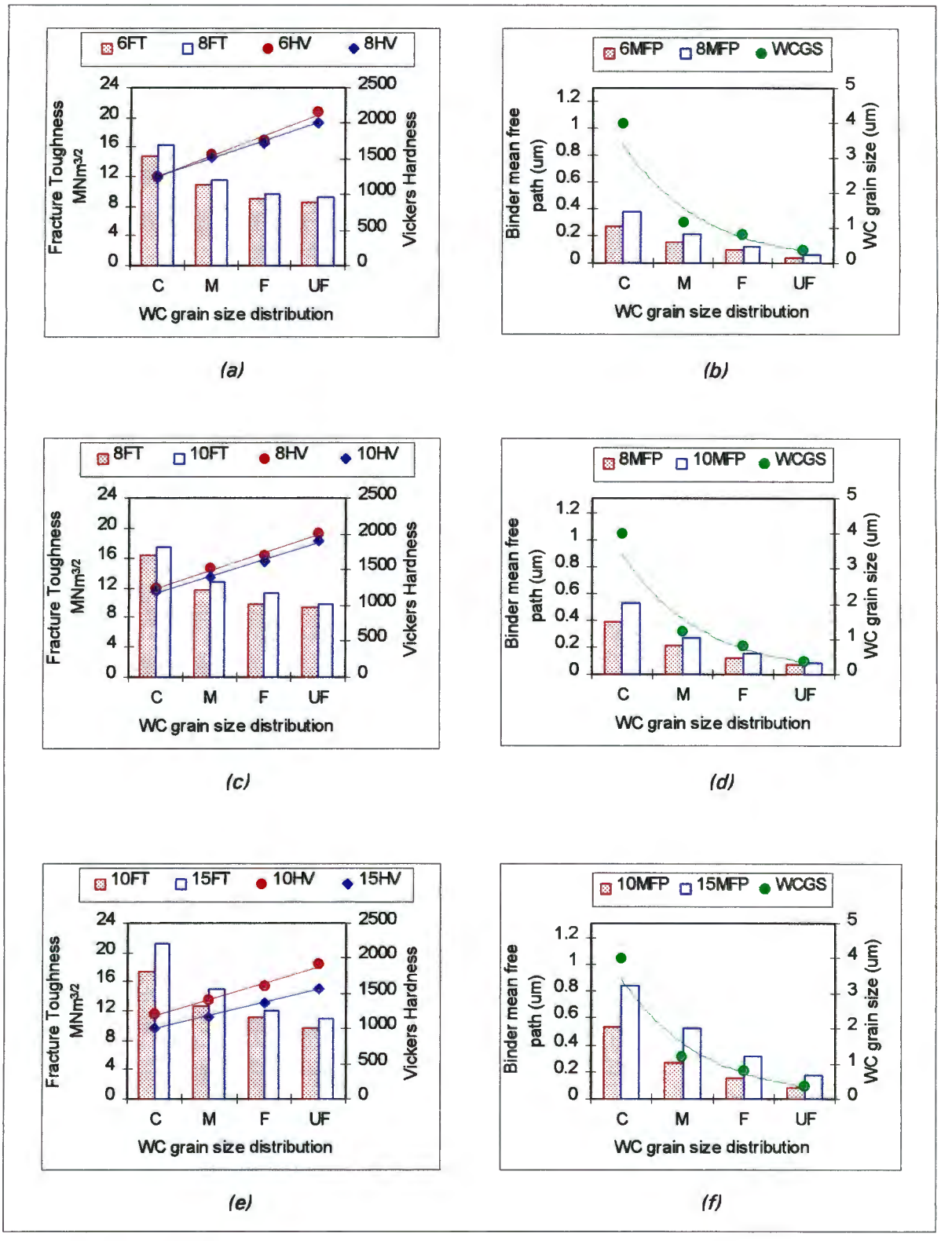

Figure 7.2 *Relationships between mechanical properties and microstructure for a series of cemented carbides.*

(a) 6 – 8 wt% cobalt range *(b) 6 – 8 wt% cobalt range*

(c) 8 – 10 wt% cobalt range *(d) 8 – 10 wt% cobalt range*

(e) 10 - 15 wt% cobalt range *(e) 10 – 15 wt% cobalt range*

A higher hardness is obtained as the tungsten carbide grain size decreases. This relationship is in agreement with Lee's[189] results which found that the hardness of hot pressed tungsten carbide decreased linearly with increases in the square root of the mean crystal size. In general, the size of the carbide particles is controlled by the size of the carbide particles in the original powder mixture, hence the ultrafine powders are expected to be harder than the conventional alloys.

As the cobalt content increases so does the binder mean free path. The binder mean free path is defined by the arithmetic mean of the distances from one carbide/binder interface to the other. It is two to four orders of magnitude smaller than the carbide grain size since one cobalt grain can incorporate many carbide crystals. Thus the mechanical behaviour of the binder, and in turn the cemented carbide, is strongly related to this mean free path. It also corresponds to the distance a dislocation can move, provided the binder regions are free of precipitates and dislocation movement occurs during fracture. At higher cobalt contents, the mean free path appears to increase more rapidly compared to that found at low cobalt contents.

The relationship between hardness and the mean free path in conventional hardmetals is different to that observed in ultrafine hardmetals. In general hardness increases with decreasing binder mean free path. However, the change in the rate of the binder mean free path with increasing hardness in ultrafine alloys is much smaller than in the conventional ones.

As the mean free path increases so does the toughness of the alloys since it is mainly the binder phase that resists fracture in cemented carbides. Prior to fracture, the cobalt will undergo plastic deformation and the extent to which it can deform is determined by the binder mean free path length. Hence, metals with high cobalt contents with high mean free paths are tougher than alloys with low cobalt contents and small mean free paths. This is shown in figure 7.2. As a result the fracture toughness shows a definite dependence on the mean free path.

The higher fracture toughness observed in the coarse material compared to the finer ones is also consistent with the toughness of the binder being dependent on the amount of tungsten in solution, which is higher in coarse material than in fine one. This is linked to the findings of Rudiger[87] who reported that the tensile strength of the binder increases with increases in its tungsten content.

In the present work an increase in toughness was observed as the mean free path increased. This increase has been attributed to the effect of the decreasing plastic constraint in the layer of the ductile phase for cemented carbides with grain sizes greater than 1μm[101]. As the plastic flow becomes easier, local stress concentrations are relieved and both crack initiation and crack propagation are impeded.

It has been shown that an increase in hardness, which is associated with a decrease in cobalt, leads to a decrease in fracture toughness. The relationship between fracture toughness and hardness is found to be linear for each carbide grain size distribution. This is in agreement with the results of Pickens[138] and O'Quigley *et al*[141], who found that this linearity was valid as long as the carbide grain size remained constant. It was found that above a carbide grain size of 1μm, fracture toughness values between 9 and 22MNm$^{-3/2}$ were obtained within a hardness range of 1000 to 1800 Vickers. Below a 1μm carbide grain size, fracture toughness between 8 to 12MNm$^{-3/2}$ was found within a hardness range of 1500 to 2200 Vickers.

Palmqvist fracture toughness values confirm that toughness decreases with increasing hardness in conventional composites, but the increase of hardness in the ultrafine alloys does not cause a significant decrease in their bulk fracture toughness. This implies that different toughening mechanisms may exist in the conventional and in the ultrafine composites. Jia *et al*[142] explained this behavior in terms of the plastic deformation concept in conventional composites whereas for the ultrafine alloys, the bridging cobalt ligament mechanisms play a significant role.

The rate of increasing toughness with decreasing hardness is found to be higher the coarser the carbide grain size distribution becomes. This is in agreement with the results by Chermant and Osterstock[140] and O'Quigley *et al*[141]. The gap between low and high toughness at a specific hardness is significantly greater at lower hardness than at higher hardness. The reverse behavior is found for the gap between low and high hardness values.

Schubert *et al*[23] found this to be true for their results. In addition, since they studied a wider range of cemented carbides, they discovered that the fracture toughness approaches a limiting value of approximately 7.7MNm$^{-3/2}$, which corresponds to the WC/WC interface toughness. This correlates well with the value of 8MNm$^{-3/2}$ which was estimated from the present work. Schubert *et al*[23]

concluded that this result indicates that above 2000 Vickers, possible improvements in toughness, due to an optimization of the carbide-to-binder variations, are only possible within a rather limited toughness range.

The ultrafine-grained alloys are seen to achieve superior hardness to toughness combinations since they contain more binder material than conventional alloys at a specific hardness. However, as previously discussed, even though they are harder than conventional alloys they are not always tougher. Several explanations have been given for this behaviour by Schubert *et al*[23]:

- in order to maintain the fineness of the carbide, increased amounts of grain growth inhibitors have to be added. These additions can lead to embrittlement through the formation of precipitates or by grain boundary segregation;
- due to strong grain growth inhibition, particle rearrangement processes become limited during sintering. In this case uneven binder distribution, which arises during the spreading process in the early stages of sintering might not be fully homogenized during isothermal sintering;
- the small mean free paths observed cause constraints of the binder when it undergoes deformation, limiting the dislocation slip lengths and results in the binder behaving increasingly brittle. Below a critical mean free path size limit, it might even lose its deformation ability. In addition minute tungsten carbide particles are also known to act as dispersoids, which increase the hardness of the binder, but lower its ductility.

7.4 COMPARISON OF THE ULTRAFINE HARD METALS

In this section ultrafine alloys produced from three different powder production routes are compared with respect to fracture toughness, hardness, mean free path of the binder, effect of cobalt content, the influence of vanadium carbide content and tungsten carbide grain size.

Figure 7.3 illustrates the mechanical and microstructural properties of these ultrafine alloys produced via the UD, UN and US powder routes. It appears that both the mechanical and microstructural properties are independent of the powder production route taken, but as the cobalt and vanadium carbide contents change, the hard metals respond differently.

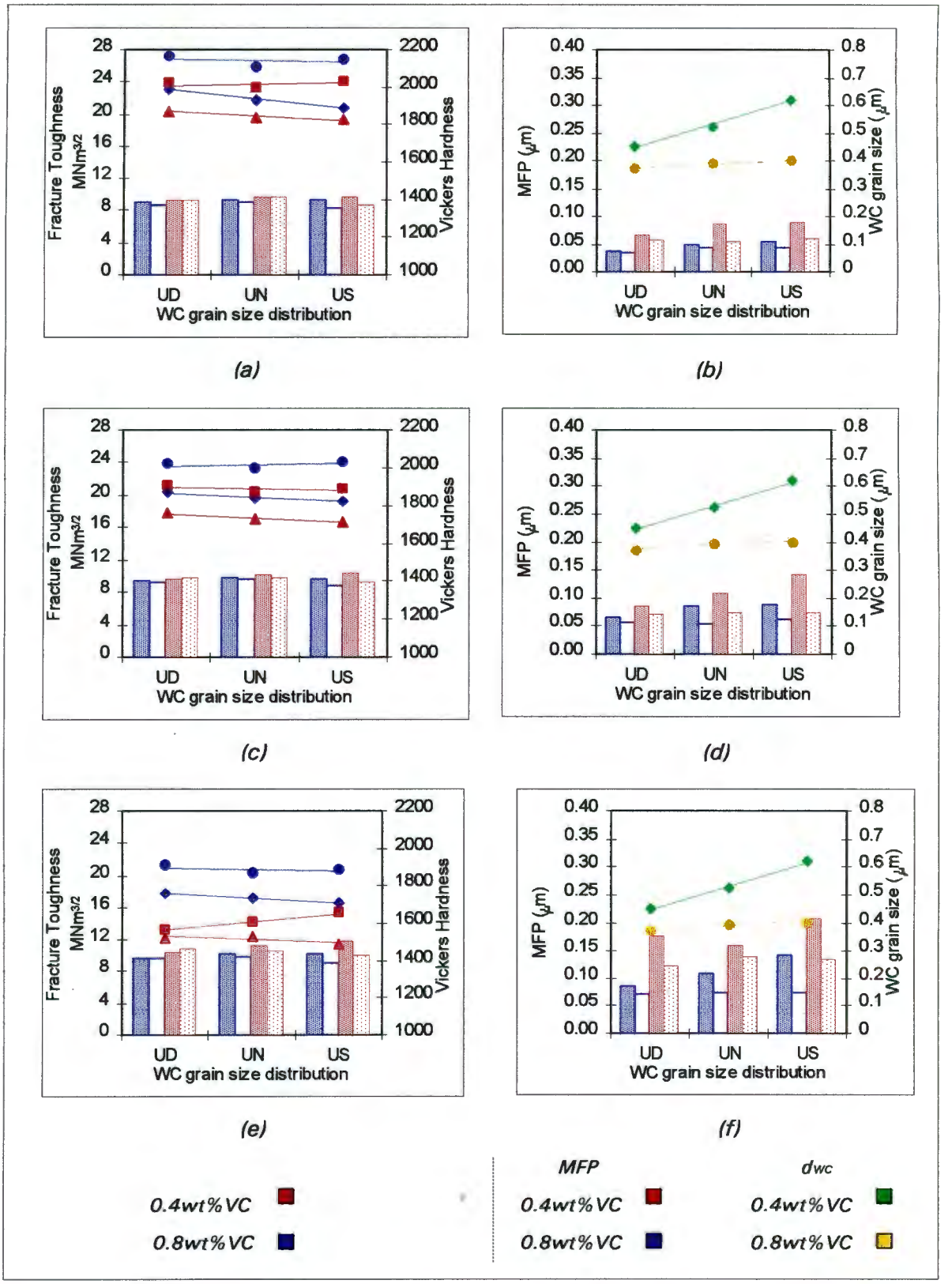

Figure 7.3 *Comparison of the mechanical and microstructure relationships of the ultrafine alloys.*

(a) 6 – 8 wt% cobalt range *(b) 6 – 8 wt% cobalt range*

(c) 8 – 10 wt% cobalt range *(d) 8 – 10 wt% cobalt range*

(e) 10 - 15 wt% cobalt range *(e) 10 – 15 wt% cobalt range*

From figure 7.3, it appears as though all the grades have similar hardness and toughness range at most levels of cobalt content. The influence of vanadium carbide on the ultrafine metals is also significant. The expected trend of increasing hardness with increasing vanadium carbide content was observed for every grade. Between 8 and 10wt% cobalt the hardness differences between the 0.4 and the 0.8wt% vanadium carbide alloys is fairly constant for each of the different powders. However, for the cobalt ranges of 6 to 8wt% and 10 to 15wt%, there is some inconsistency amongst the grades.

One of the most frequent arguments for better toughness-hardness combinations of fine-grained cemented carbides is the higher binder content which can be tolerated in these alloys for a given hardness level. It is assumed that the more ductile the binder, the more tough the material should be. While this argument sounds feasible, this was not found in the present work. Schubert *et al*[23] also found that this simple relationship does not exist when they compared alloys of the same hardness but with different binder contents. There are other microstructural parameters or compositional parameters that influence the hardness-toughness relationship. Variables such as a proper control of the carbon content or sintering conditions will co-determine the toughness behaviour.

To account for the decrease of strength of low cobalt alloys with smaller tungsten carbide grain sizes at constant composition, Gurland and Bardzil[101] stated that it is necessary to consider the observed increase of fracture incidence at the carbide grain boundaries. With smaller carbide grains, as well as less binder, there is an increasing area of carbide to carbide contact, i.e, an incomplete surrounding of carbide grains by the cobalt binder. They were not able to establish whether the grain boundaries themselves are weak or whether their failure is due to stress concentrations caused by the uneven distribution of the binder phase.

As the vanadium carbide to cobalt ratio increases the alloys become less tough. The maximum ratio at which this occurs has been found to be 0.1[23]. In this study, some of the ultrafine alloys did not appear to follow this trend and instead the 0.8wt% vanadium carbide alloys became tougher than the 0.4wt% vanadium carbide alloys. Schubert *et al*[23] also found similar results in their work. Thus additions of vanadium carbide appear not to automatically lower the toughness of a hard metal.

Osborne *et al*[190] found that the lower toughness of VC-WC-Co hard metals is due to the low toughness of the vanadium carbide grains. These grains offer an easy path to fracture propagation. It is reasonable to assume that the toughness of VC-WC-Co could be improved by reducing the vanadium carbide grains to a size below the critical crack length of the hard metal, so that even if the grains do crack, the cracks do not cause catastrophic failure.

Other inhibitors that have been used include Cr_2C, TiC, TaC and NbC. The chromium carbides provide excellent wear resistance coupled with good oxidation and corrosion resistance. However, they lack the toughness needed for cutting tools. The other three additives are used in modern cutting tools where they increase the high temperature wear resistance. But these additions also increase the brittleness and decrease the toughness of the metal.

The interesting fact that is observed with the ultrafine alloys is that some of them have similar hardness and toughness values. This implies that these grades could be used for similar applications without compromising the end user. Although certain grades can be interchanged for the same application, caution has to be exercised in assessing the toughness requirement for the product and also in considering the work environment of the hardmetal tool as well as the service requirements.

7.5 COMPARISON OF THE PALMQVIST AND SHORT ROD FRACTURE TOUGHNESS TEST METHODS

Although fracture toughness provides an excellent measure of the strength of materials, traditional test procedures are better suited to the scientific laboratory than for industrial quality control procedures. Large specimens, rigid tensile equipment and sophisticated crack opening measurements are required for K_{Ic} determinations. The specified ASTM procedure for determining fracture toughness is also relatively expensive.

These factors have caused the hard metal industry to find simpler and cheaper, but internationally acceptable methods for determining the toughness of their products. The majority of the hard metal industry uses the Palmqvist Indentation method and the Short Rod test method to a lesser extent.

The results obtained from the two methods have been found to be similar, hence it seems that values for cemented carbides from either test are interchangeable. The Short Rod test did show a greater scatter in data obtained for the same hard metal. However, when the average toughness value is calculated, it is similar to that determined using the Palmqvist test on the same sample. The error between using the two tests is negligible.

The main drawback with using the Palmqvist method is the specimen surface preparation required before testing is carried out. This requirement is based on the residual stresses which are introduced into the specimen during grinding of the surface. A proper surface preparation technique is therefore most important pre-requisite for reliable testing. If these stresses are not eliminated by annealing at temperatures above 800°C or by extended polishing times, the resulting crack lengths will be dominated by the residual grinding stresses. A certain measurement uncertainty also arises from systematic and random errors that are made during the crack length measurement.

On the other hand, for the Short Rod test, the slotting of the specimen into the required geometry prior to testing is extremely lengthy. It takes approximately two hours to slot one specimen. If faster cutting machine speeds can be employed without damaging the specimen, this test would be more desirable. Another disadvantage in the specimen cutting action is the stresses that this cutting introduces into the alloy. The release of these stresses during testing could result in improper toughness values being made. Placement of the sample in the test apparatus is important since the crack will follow the slot guides very well provided the sample is symmetrically placed about the slot plane. Improper placement destroys the specimen, a phenomenon which was noticed during testing of this work.

The crack lengths measured in the Palmqvist test are linked to a formula first developed by Palmqvist[1], but later modified by Exner[173], in determining the crack resistance of the alloy. This parameter has units of N/m and needs to be converted into units of $MNm^{-3/2}$ in order to be accepted as fracture toughness, K_{Ic} values. However, modeling of the Palmqvist cracks is difficult because of their complex crack geometry and orientation relative to the plastic zone during indentation. This difficulty is reflected in the widely different fracture mechanics analysis suggested by many investigators[180,181,185]. However, some researchers have developed equations linking the crack resistance parameter to K_{Ic}, which are widely used in industry.

The ASTM method for fracture toughness testing recognizes the possibility of rate effects in metals, Thus when following the ASTM procedure specifications, the toughness tests have to be conducted at specific stress intensity increase rates. However, Barker[170] stated that since the ASTM method is based on the onset of crack position instability, while the Short Rod test is based on crack growth instability, it is the crack speed rather than the rate of change of K that varies.

Advantages in using the Palmqvist test in industry include:

- it is a non-destructive test
- a small sample area is required for the test
- the hardness of the metal is found automatically
- used for speedy quality control and sorting
- simple to perform
- adequate information is obtained from a few samples

Advantages of using the Short Rod test include:

- simple loading devices can be employed to provide the force
- the only measured quantity during the test is the peak force required to completely fracture the sample
- method applicable to brittle and ductile materials
- no special pre-cracking technique is required

Chapter 8

CONCLUSIONS

The fracture toughness of a series of ultrafine-grained cemented carbides sintered from powders produced through three different routes has been determined using the Palmqvist Indentation test and the Short Rod test. A further twelve WC-Co alloys with varying cobalt contents and carbide grain sizes, produced through conventional processes, have also been tested in order to provide data for comparison.

The work carried out during the coarse of this thesis has led to the following conclusions:

1. The data obtained from the two different fracture toughness test methods are comparable. However, the Short Rod test values have a higher scatter in data per grade. For the Palmqvist test it is found that annealing the specimen at 900°C reduces the amount of polishing time needed to prepare the specimen surfaces for Palmqvist crack measurements. A main advantage of the Palmqvist test above the Short Rod test is that the former is non-destructive. One sample can be used to determine many toughness measurements.

2. The fracture toughness of tungsten carbide hardmetals is largely influenced by parameters such as hardness, tungsten carbide grain size, cobalt content and the mean free path of the binder. In the ultrafine-grained alloys the fracture path proceeds preferentially through the binder phase, while it proceeds preferentially through the carbide crystals in coarser-grained hard metals.

3. A decrease in tungsten carbide grain size is associated with a decrease in the fracture toughness, an increase in the hardness, and a decrease in the binder mean free path.

4. The ascending rate of binder mean free path with decreasing hardness in coarse-grained hardmetals is much higher than in ultrafine-grained hardmetals. As the mean free path increases so does the fracture toughness since it is mostly the binder phase that resists fracture. At 0wt% cobalt, the fracture toughness of all the hardmetals extrapolated to a toughness value of approximately $8MNm^{-3/2}$.

5. The relationship between fracture toughness and hardness is linear provided the carbide grain size remains constant. The gap between low and high toughness at a specific hardness is significantly greater at lower hardness than at higher hardness levels.

6. The rate of increasing hardness with decreasing toughness is found to be higher the finer the carbide grain size distribution becomes. Above a carbide grain size of 1μm fracture toughness between 9 and $22MNm^{-3/2}$ is achieved within a hardness range of 1000 to 1800 Vickers. Below a carbide grain size of 1μm fracture toughness between 8 and $12MNm^{-3/2}$ is obtained within a hardness range of 1500 to 2200 Vickers.

7. At a given hardness the ultrafine alloys contain more binder material than the conventional materials, yet they are not necessarily tougher. The moderate toughness of the ultrafine alloys has been attributed to small carbide grains, small values of binder mean free path and to the influence of vanadium carbide.

8. There is no appreciable difference in mechanical and microstructural properties for the ultrafine grades produced by the three different powder routes.

REFERENCES

1. S. Palmqvist, Jernkontorets Annalen, **141**, 300 (1957).
2. ASTM B 771-87, October 1987.
3. Shetty *et al.*, J. Mater. Sci., **20**, 1873 (1985).
4. J. Vicens *et al.*, J.Mater. Sci., **29**, 987 (1994).
5. F. V. Lenel, Powder Metallurgy: Principles and Applications, Metal Powder Industries Federation, New Jersey, 383 (1980).
6. Y. Kanemitsu *et al.*, Int. J. RM&HM, **1[2]**, 66 (1982).
7. S. Imsato, Met. Powd. Report, **47[4]**, 32 (1992).
8. P. Ettmayer, Annual Rev. Mater. Sci., **19**, 145 (1989).
9. H. Gleiter, Progress Mater. Sci., **33**, 233 (1989).
10. L. J. Prakash, Int. J. RM&HM, **13**, 257 (1995).
11. L. E. McCandlish *et al.*, US patent 5,352,269, October 4, 1994.
12. W. Schlump and H. Grewe, Conf. Proc. on New materials by mechanical alloying techniques, Calw-Hirasu, (1988).
13. A. Bock et al., Powd. Metall. Int., **24[10]**, 20 (1992).
14. H. E. Exner and J. Gurland, Powd. Metall., **13**, 13 (1970).
15. H. Pastor, Proc. Euro. Powd. Metall. Conf., European Powder Metallurgy Association, Shrewsbury, 3 (1996).
16. Karl Schroter, USA Patent 1549615, October 31, 1923.
17. H. E. Exner, Int. Mater. Review, **243[4]**, 149 (1979).
18. D. N. French, Int. J. Powd. Metall., **5**, 47 (1969).
19. B. Clark, Proc. Powd. Metall. World Congress, Les Editions de Pysique, Les Ulis, France, 179 (1994).
20. S. E. Hankey, Cavitation erosion of WC-Co, MSc Thesis, UCT, 1987.
21. B. Roebuck and E. A. Almond, Int. Mater. Rev., **33[2]**, 90 (1988).
22. C. S. Yust and E. L. Long jr., Ceramic Bulletin, **62[9]**, 1039 (1983).
23. W. D. Schubert *et al.*, Int. J. RM&HM, **14**, 285 (1995).
24. B. Aronsson and M. Lagerquist, Met. Powd. Rev., **39**, 687 (1984).
25. B. Aronsson and L.J. Aschan, Met. Powd. Rev., **40**, 785 (1985).
26. M. Rosso *et al.*, Proc. 13th Plansee Conf., Eds. H. Bildstein and R. Eck, Metallwerk Plansee Reutte, **2**, 250 (1993).
27. R. Porat *et al.*, Proc. Euro Powd. Metall. Conf., European Powder Metallurgy Association, Shrewsbury, 101 (1996).
28. A. Egami *et al.*, Proc. 13th Plansee Conf., Eds. H. Bildstein and R. Eck, Metallwerk Plansee Reutte, **3**, 639 (1993).
29. KJA Brookes, World directory and handbook of hard metals. 5th Edition, London, (1992).
30. P. Arato *et al.*, Proc. 14th Plansee Conf., Eds. G. Knerringer, P. Rödhammer and P. Wilhartitz, Plansee AG, Reutte, Austria, **2**, 658 (1997).
31. A. Aronsson and H. Pastor, Powd. Metall: An overview, The Institute of Materials, London, 312.

32. J. Gurland, Trans. AIME, J. of Met., 289 (1954).
33. V. K. Sarin, Proc. Int. Powd. Metall. Conf., 1 (1976)
34. S. Bartolucci-Luyckx, Proc. 1st Int. Conf. Sci of Hard Mater., Eds. R. K. Viswanadham, D. F. Rowcliffe and J. Gurland, Plenum Press, New York, 629 (1983).
35. D. N. French and D. A. Thomas, Fall meting of the AIME, Chicago, (1966).
36. L. E. McCandlish *et al.*, Mater. Sci. Technol., **6**, 953 (1990).
37. G. J. Rees and B. Young, SA Mech. Eng., 81 (1972).
38. R. F. Snoball and D. R. Milner, Powd. Metall., **11**, 23 (1968).
39. J. Hinnuber *et al.*, Powd. Metall., **8**, 7 (1961).
40. E. M. Trent, Powd. Metall., 9, 322 (1962).
41. B. Lehtinen and K. E. Easterling, Planseber. Pulvermet., 141 (1972).
42. D.C Gillies and D. Lewis, Powd. Metall., **11**, 400 (1968).
43. D. Lewis and J. Lindley, J. Amer. Ceram. Soc., **49**, 49 (1966).
44. D. F. Carrol. Proc. 14th Plansee Conf., Eds. G. Knerringer, P. Rödhammer and P. Wilhartitz, Plansee AG, Reutte, Austria, **2**, 168 (1997).
45. H. Suzuki and K. Tokumoto, Powd. & Powd. Metall., **32[4]**, 152 (1985).
46. M.Liederman *et al.*, Proc. Euro Powd. Metall. Conf., European Powder Metallurgy Association, Shrewsbury, 145 (1996).
47. P. Schwarzkopf and R. Kieffer, Cemeted Carbide, McMillan, New York (1960).
48. B. Uhrenius, Proc. Powd. Metall. Conf. 1443 (1994).
49. B. H. Kear and L. E. McCandlish, Nanostructured Mater., **3**, **19** (1993).
50. J. W. Lee *et al.*, Powd. Metall., **23[2]**, 57 (1980).
51. H. A. Saller *et al.*, US Patent 687 842, 1964.
52. H. D. Hanes *et al.*, "Hot Isostatic Pressure", Battelle Press, Ohio, (1969).
53. B. Bengtsson *et al.*, Planseeber. Pulvermet., **22**, 285 (1974).
54. D. G. Attwood, Conf. Proc. Recent advances in hard metal production, Loughborough, (1979).
55. J. Hong and J. Gurland, Metallography, **14**, 327 (1981).
56. L. S. Sigl *et al.*, Conf. Proc. Sci. of Hard Mater., 631 (1984).
57. E. A. Almond, Speciality steels and hard materials, Eds., N. R. Comins and J. B. Clark, Pergammon Press, Oxford, 353 (1982).
58. L. S. Sigl and H. E. Exner, Metall. Trans. A, **18A**, 1299 (1987).
59. G. Gille, Proc. Int. Conf. Pow. Met., Dresden, GDR, **1**, 9 (1977).
60. E. A. Almond, Proc. 1st Int. Conf. Sci of Hard Mater., Eds. R. K. Viswanadham, D. F. Rowcliffe and J. Gurland, Plenum Press, New York, 517 (1983).
61. R. Speigler and H. F. Fischmeister, Acta. Metall. Mater., **40[7]**, 1653 (1992).
62. R. K. Viswanadham and T. S. Sun, Scripta Met., **13**, 767 (1981).
63. A. Lea and B. Roebuck, Met. Sci., **15**, 263 (1981)
64. N. K. Sharma *et al.*, J. Amer. Ceram. Soc., **63**, 194 (1980).
65. A. F. Evans *et al.*, Proc. 4th Int. Conf. on Fract., Ed. D. M. R. Taplin, Pergammon Press, New York, 529 (1977).
66. L. S. Sigl *et al.*, Acta metall., **36**, 945 (1988).
67. L. S. Sigl and H. F. Fischmeister, Acta Metall., **36[4]**, 887 (1988).
68. S. Schmauder *et al.*, Proc. 15th Congress FEM, 213 (1986).

69. A. G. Evans and R. M. McMeeking, Acta metall, **34**, 2435 (1986).
70. S. Bertolucci-Luyckx, Proc. 4th Int. Conf. On Fract., Ed. D.M.R. Taplin, Pergammon Press, Oxford, 233 (1977).
71. R. Spiegler *et al.*, Proc. 2nd Int. Conf. FEM, Strausberg, France, Steinkopf Druck Stuttgart, Germany, 21 (1990).
72. M. Slesar *et al.*, Conf. Proc. 2nd Int. Sci. of Hard Mater., Eds. E. A. Almond, C. A. Brookes and R. Warren, Adam Hilger Ltd, Boston, 657 (1986).
73. H. Fischmeister and L. R. Olsson, "Cutting Materials", Metals Park, Ohio, 111 (1981)
74. B. Roebuck *et al.*, Proc. Euro Powd. Metall. Conf., European Powder Metallurgy Association, Shrewsbury, 229 (1996).
75. H. E. Exner, Proc. Euro Powd. Metall. Conf., European Powder Metallurgy Association, Shrewsbury, 255 (1996).
76. R. Warren and H. J. Matzke, Proc. 1st Conf. Sci. Hard Mater., Eds. R. K. Viswanadham, D. F. Rowcliffe and J. Gurland, Plenum Press, New York, 563 (1983).
77. R. Spiegler *et al.*, J. Hard Mater., **1[3]**, 147 (1990).
78. D. Marshall *et al.*, J. Amer. Ceram. Soc., **73[10]**, 2938 (1990).
79. J. Gurland, Trans. Met. Soc. A.I.M.E., **227**, 1146 (1963).
80. J. L. Chermant and F. Osterstock, Powd. Metall. Int., **11**, 106 (1979).
81. A. Nordgren and A. Melander, Powd. Metall., **31**, 189 (1988).
82. C. Colin *et al.*, Int. J. RM&HM, **12**, 145 (1994).
83. C. C. McBride *et al.*, Amer. Ceram. Soc., **35**, 28 (1952).
84. S. K. Bhaumik *et al.*, J. Mater. Sci. Lett., **11**, 1457 (1992).
85. W. Mader *et al.*, Int. J. Powd. Metall. & Powd. Technol., **13**, 41 (1977).
86. H. Suzuki and H. Kubota, Planseeber. Pulvermet., **14**, 96 (1966).
87. O. Rudiger *et al.*, Int. J. Powd. Metall., **7**, 29 (1971).
88. H. Jonsson, Planseeber. Pulvermet., **21**, 187 (1973).
89. H. Jonsson, Powd. Met., **15[29]**, 1 (1972).
90. H. Jonsson, Planseeber Pulvermet., **23**, 37 (1975).
91. J. L. Chermant and F. Osterstck, J. Mater. Sci., **11**, 1939 (1976).
92. M. J. Murray, Proc. Roy. Soc., **356A**, 483 (1977).
93. M. Namakura and J. Gurland, Met. Trans. **11A**, 141 (1980).
94. H. Fischmeister and H. Exner, Arch. Eissenhutten, **37[6]**, 499 (1966).
95. A. Mason and P. Kenny, Metallurgia, **12**, 205 (1970).
96. K. M. Friederich *et al.*, Proc. 10th Plansee Conf., Ed. H. M. Ortner, Metallwerk Plansee, Reutte, Austria, **1**, 795 (1981).
97. E. A. Almond and B. Roebuck, Proc. 10th Plansee Conf., Ed. H. M. Ortner, Metallwerk Plansee, Reutte, Austria, **1**, 659 (1981).
98. J. Gurland, Trans. AIME, **212**, 452 (1958).
99. G. S. Kreimer *et al.*, Physics Met. Metall., **17**, 85 (1964).
100. E.W. Engle, "Powder Metallurgy", Ed. J. Wulff, 436 (1942).
101. J. Gurland and P. Bardzil, Trans. Amer. Inst. Min. Met. Eng., **203**, 311 (1955).
102. C. Nishimatsu and J. Gurland, Trans. Amer. Soc. Metals, **52**, 469 (1960).
103. G. S. Kreimer and N.A. Alekseeva, Phy. Met. Metallography, **13[4]**, 117 (1962).
104. G. S. Kreimer *et al.*, Phy. Met. Metallography, **13[6]**, 91 (1962).

105. H. Suzuki, Trans. Japan Inst. Metals, 7, 112 (1966).
106. O'Quigley *et al.*, Proc. 14th Plansee Conf., Eds. G. Knerringer, P. Rödhammer and P. Wilhartitz, Plansee AG, Reutte, Austria, **2**, 477 (1997).
107. R. K. Viswanadam *et al.*, J. Mat. Sci., **16**, 1029 (1981).
108. A.Nidikom and T. J. Davis, Proc. 10th Plansee Conf., Ed. H. M. Ortner, Metallwerk Plansee, Reutte, Austria, 28 (1981).
109. J. R. Pickens and J. Gurland, Mat. Sci. Eng., **33**, 135 (1978).
110. J. L. Chermant *et al.*, Fracture mechanics, Plenum Press, New York, **1**, 346 (1974). Eds. R. C. Bradt, D. P. H. Hasselman and F. F. Lange.
111. R. C. Lueth, Fracture mechanics, Plenum Press, New York, **2**, 791 (1974). Eds. R. C. Bradt, D. P. H. Hasselman and F. F. Lange.
112. LN. Ingelstrom and H. Nordberg, Eng. Fract. Mech., **6**, 597 (1974).
113. L. Lindau, Proc. 4th Int. Conf. Fracture, Ed. D.M.R. Taplin, Pergammon Press, Oxford, **4**, 215 (1977).
114. G. S. Kreimer and M.R. Vakhovskaya, Sov. Powd. Met. Metal Ceram., 454 (1965).
115. L. D. Brownlee *et al.*, Powd. Metall. Symp., 302 (1954).
116. J. Gurland, Jern. Ann., **4**, 147 (1963).
117. H. Kubota *et al.*, Trans. Indian Inst. Metals, **17[5]**, 132 (1964).
118. D. N. French and D. A. Thomas, Int. J. Powd. Metall., **3**, 7 (1967).
119. Z. Fang and J. W. Eason, Int. J. Powd. Metall., **29[3]**, 259 (1993).
120. H. Suzuki *et al.*, Planseeber. Pulvermet., **2**, 121 (1975).
121. S. Amberg and H. Doxner, Powd. Metall., **1**, 1 (1977).
122. H. F. Fischmeister and H. E. Exner, Planseeber. Pulvermet., **13**, 178 (1965).
123. D. C. Drucker, High Strength Materials, Ed. V.F. Zackay, New York and London, John Wiley, 795 (1965).
124. N. M. Parikh, J. Amer. Ceram. Soc., **40**, 335 (1957).
125. A. Nordgren, Int. J. RM&HM, **10**, 61 (1991).
126. A. Nordgren, J. Hard Mater., **3[2]**, 195 (1992).
127. B. Roebuck *et al.*, Proc. 13th Plansee Conf., Eds. H. Bildstein and R. Eck, Metallwerk Plansee, Reutte, Austria, **2**, 273 (1993).
128. Z. Fang and J. W. Eason, Proc. 13th Plansee Conf., Eds. H. Bildstein and R. Eck, Metallwerk Plansee, Reutte, Austria, **3**, 625 (1993).
129. R. Cheney *et al.*, US Patent 4450724, 1984.
130. R. Porat and J. Malek, J. Mater. Sci. Eng., **A105/106**, 289 (1988).
131. V. Tumnov, Poroshkovaya Metallurgia, **75[3]**, 77, (1969).
132. B. Roebuck, Int. J. RM&HM, **13**, 265 (1995).
133. H. C. Lee and J. Gurland, Mater. Sci. Eng., **33**, 125 (1978).
134. J. Gurland, Trans. Metall. Soc. AIME, **236**, 642 (1966).
135. L. E. McCandlish *et al.*, Proc. Conf. Adv. Powd. Metall. & Part. Mater., 1 (1994).
136. J. Karch *et al.*, Nature, **330**, 556 (1987).
137. J. L. Henshall *et al.*, J. Hard Mater., **4**, 1 (1993).
138. J. R. Pickens, PhD Thesis, Brown University, USA, (1977).
139. R. Warren and B. Johannesson, Int. J. RM&HM., **3**, 187 (1984).
140. J.L. Chermant and F. Osterstock, J. Mater. Sci., **11**, 1939 (1976).

141. D.G.F. O'Qicgley *et al.*, Mat. Sci. Eng., **A209**, 228 (1996).
142. K. Jia and T. E. Fischer, Nanostructured Mater., **10[5]**, (1988).
143. G. R. Irwin, Handbuch der Physik, Ed. S. Flugge, Springer-Verlag, Berlin, **6**, 551.
144. G. R. Irwin, Report No. 5486, U.S., Naval Research Laboratory, Washington D.C., (1960).
145. G. R. Irwin, J. Appl. Mech., **24**, 361 (1957).
146. M. L. Williams, J. Appl. Mech., **24**, 109 (1957).
147. J. F. Knott, "Fundamentals of Fracture Mechanics", Butterworth, London, (1973),
148. D. P. Rooke and D. J. Cartwright, "Compendium of Stress Intensity Factors", H.M.S.O., London, (1976).
149. J. O. Outwater and D. J. Gerry, Interim report, University of Vermont, Burlington, Vermont (1966).
150. D. P. Williams and A. G. Evans, J. Testing and Evaluation, **1**, 264 (1973).
151. C. D. Beachem *et al.*, Mat. Res. and Standards, **11[4]**, 30 (1971).
152. E. R. Fuller JR., Proc. 11th National Symposium on Fracture Mechanics, Ed. S. W. Freiman. ASTM Philadelphia, 3 (1978).
153. A. G. Evans *et al.*, Mater. Sci. Eng., **15**, 253 (1974).
154. R. Scaller *et al.*, J. Hard Mater., **3**, 529 (1992).
155. K. G. Stjernberg, Sandvick AB Report, 365.
156. H. Iizuka and M. Tanaka, J. Mater. Sci., **I26**, 4394 (1991).
157. E. A. Almond and B. Roebuck, Met. Technol., **5**, 92 (1978).
158. ASTM Standard E399, 10
159. G. Berry, Met. Sci., **10**, 361 (1976).
160. U. Engel and H. Hubner, J. Mater. Sci., **13**, 2003 (1978).
161. A.S.T.M Special Technical Publication 463.
162. B. R. Lawn and T. R. Wilshaw, "Fracture of Brittle Solids", Cambridge Univ. Press, Cambridge, UK, 110 (1975).
163. S. Suresh and J. R. Brockkenbrough, Acta. Metall., **36**, 1455 (1988).
164. S. S. Yen, MSc Thesis, Lehigh University, (1971).
165. L. M. Barker, Eng. Fract. Mech., **9**, 361 (1977).
166. L. M. Barker, "Fracture Mechanics Applied to Brittle Materials", Ed. S. W. Frieman, ASTM, 73 (1979).
167. G. R. Erwin and J. E. Kies, Welding J., **33**, 193 (1954).
168. ASTM Standard B 771-87.
169. L. M. Barker, Proc. 5th Int. Conf. Fract., Cannes, France, (1981).
170. L. M. Barker, Terra Tek Report TR80-12, (1980).
171. R. K. Viswanadham and J. D. Venables, Metall. Trans., **8A**, 187 (1977).
172. E. A. Almond and B. Roebuck, Proc. 1st Int. Conf. Sci of Hard Mater., Eds. R. K. Viswanadham, D. F. Rowcliffe and J. Gurland, Plenum Press, New York, (1983).
173. H. E. Exner, Trans. Met. Soc. AIME, **245**, 677 (1969).
174. S. B. Luyckx, Speciality steels and hard materials, Eds., N. R. Comins and J. B. Clark, Pergammon Press, Oxford, 369 (1982).
175. P O Snell and E Parnama, Proc. Powd. Metall. Conf., 645 (1973).
176. S. Singh and P. Ramakrishnan, RM&HM, 27 (1985).
177. C. T. Peters, J. Mater. Sci., **14**, 1619 (1979).

178. S. H. Zhang and Y. X. Liu, Proc. Int. Conf. Powd. Metall., Eds. P. U. Gummeson and D. A. Gustafson, MPIF & APMI, New Jersey, 33 (1988),
179. R. K. Viswanadham and J. D. Venables, Proc. Int. Conf. Adv. Hard Mater. Tool Technol., Ed. R. Komanduri, Carnegie Press, USA, 245 (1976).
180. E. L. Exner *et al.*, Met. Trans. A., **9A**, 736 (1978).
181. C. M. Perrot, Wear, **47**, 81 (1978).
182. F. R. N, Nabarro and S. B. Luyckx, Trans. Japan Inst. Metals, **9**, 610 (1968).
183. J. L. Chermant *et al.*, Powd. Metall., **2**, 63 (1977).
184. E. L. Exner *et al.*, Proc. 5th Euro Conf. Powd. Metall., **2**, 63 (1978).
185. K. Niihara, J. Mater. Sci. Lett., **2**, 221 (1983).
186. B. Lawn and R. Wilshaw, J. Mater. Sci., **10**, 1049 (1975).
187. E. E. Underwood, 'Quantitative Metallography', Addison-Wesley, Reading, MA, (1970).
188. I. Northrop, Private Communication.
189. H. C. Lee, PhD Thesis, Brown University, Rhode Island, USA, (1977).
190. C. Osborne *et al.*, Int. J. RM&HM, **15**, 163 (1997).

APPENDIX A

VICKERS HARDNESS

This appendix lists the data tables for the Vickers hardness of each ultrafine hard metal grade with respect to indenting load and heat treated condition. The data represents the average of at least thirty hardness indentations made per load for each grade. The symbols used in the tables are defined as:

HV(load) ⇒ hardness determined using a specific load
ARC1 ⇒ as-received condition polished with 9μm diamond grit
ARC2 ⇒ as-received condition polished with 0.25μm diamond grit
800°C ⇒ 800°C annealed condition
900°C ⇒ 900°C annealed condition
Ave. HV ⇒ average hardness per condition
\+ ⇒ positive deviation from the average value
\- ⇒ negative deviation from the average value

Table A1: Vickers hardness(kg/mm^2) for the 0.4wt% vanadium carbide UD alloys.

GRADE	HV(load)	ARC1	ARC2	800°C	900°C
D64	HV20	1981	1981	1986	1986
	+	49	49	44	44
	-	24	24	29	29
	HV30	1993	1993	1979	1993
	+	46	46	60	46
	-	15	15	59	15
	HV50	1988	1986	1990	1986
	+	13	15	58	15
	-	55	31	35	31
	Ave. HV	1988	1987	1985	1988
	+	6	6	5	5
	-	6	5	6	3
D84	HV20	1888	1911	1888	1888
	+	0	46	0	0
	-	0	23	0	0
	HV30	1866	1848	1920	1920
	+	54	17	0	0
	-	54	36	0	0
	HV50	1863	1855	1801	1787
	+	48	13	26	0
	-	36	28	14	0
	Ave. HV	1872	1871	1870	1865
	+	16	40	51	55
	-	9	23	69	78
D104	HV20	1769	1760	1760	1760
	+	53	0	0	0
	-	9	0	0	0
	HV30	1748	1713	1800	1795
	+	14	0	12	17
	-	35	0	38	33
	HV50	1473	1787	1749	1749
	+	6	0	0	0
	-	32	0	0	0
	Ave. HV	1753	1753	1769	1768
	+	16	34	31	27
	-	10	40	21	19
D154	HV20	1533	1540	1540	1540
	+	7	0	0	0
	-	41	0	0	0
	HV30	1532	1537	1551	1537
	+	5	0	28	0
	-	34	0	14	0
	HV50	1537	1531	1480	1451
	+	4	10	0	0
	-	27	21	0	0
	Ave. HV	1534	1536	1524	1509
	+	3	4	27	31
	-	2	5	44	59

Table A2: Vickers hardness(kg/mm^2) for the 0.8wt% vanadium carbide UD alloys.

GRADE	HV(load)	ARC1	ARC2	800°C	900°C
D68	HV20	2189	2189	2189	2162
	+	0	0	0	0
	-	0	0	0	0
	HV30	2168	2168	2191	2168
	+	0	0	46	0
	-	0	0	23	0
	HV50	2166	2183	2098	2098
	+	35	18	0	0
	-	18	35	0	0
	Ave. HV	2174	2180	2159	2143
	+	15	9	32	25
	-	8	12	62	45
D88	HV20	2030	2030	2030	2030
	+	0	0	0	0
	-	0	0	0	0
	HV30	2030	2039	2039	2039
	+	9	0	0	0
	-	52	0	0	0
	HV50	2022	2030	1955	1955
	+	76	60	0	0
	-	67	37	0	0
	Ave. HV	2027	2033	2008	2008
	+	3	21	31	31
	-	5	3	53	53
D108	HV20	1914	1911	1911	1905
	+	43	46	0	52
	-	26	23	0	17
	HV30	1907	1920	1902	1907
	+	13	58	46	0
	-	42	16	13	0
	HV50	1911	1911	1911	1911
	+	0	0	0	0
	-	0	0	0	0
	Ave. HV	1910	1914	1908	1908
	+	3	6	3	4
	-	4	3	6	3
D158	HV20	1478	1540	1591	1644
	+	14	0	0	0
	-	33	0	0	0
	HV30	1509	1511	1651	1666
	+	28	26	15	0
	-	49	13	29	0
	HV50	1506	1500	1606	1640
	+	35	10	0	0
	-	26	20	0	0
	Ave. HV	1498	1517	1651	1650
	+	11	23	35	16
	-	20	17	25	10

Table A3: Vickers hardness(kg/mm^2) for the 0.4wt% vanadium carbide UN alloys.

GRADE	HV(load)	ARC1	ARC2	800°C	900°C
N64	HV20	1929	1934	1929	1934
	+	28	23	28	23
	-	41	46	41	46
	HV30	1930	1930	1935	1935
	+	48	48	43	43
	-	10	10	15	15
	HV50	1932	1933	1934	1934
	+	29	22	21	21
	-	64	22	66	66
	Ave. HV	1930	1932	1933	1934
	+	1	2	2	1
	-	1	2	3	1
N84	HV20	1844	1835	1839	1839
	+	44	53	49	49
	-	22	13	17	17
	HV30	1839	1844	1844	1839
	+	26	21	21	26
	-	27	32	32	27
	HV50	1841	1841	1838	1841
	+	27	27	30	27
	-	54	54	11	14
	Ave. HV	1841	1840	1840	1839
	+	3	4	4	2
	-	3	5	2	1
N104	HV20	1734	1736	1736	1730
	+	26	24	24	30
	-	28	35	35	29
	HV30	1734	1729	1719	1737
	+	28	33	33	25
	-	21	16	16	24
	HV50	1730	1734	1730	1730
	+	19	15	19	19
	-	55	23	19	19
	Ave. HV	1733	1733	1732	1732
	+	2	3	4	5
	-	3	4	3	3
N154	HV20	1528	1528	1530	1530
	+	12	12	10	10
	-	36	36	38	38
	HV30	1529	1529	1527	1527
	+	8	8	10	10
	-	31	31	29	29
	HV50	1526	1529	1531	1531
	+	15	12	10	10
	-	46	9	21	21
	Ave. HV	1527	1529	1530	1530
	+	1	1	1	1
	-	2	1	2	2

Table A4: Vickers hardness(kg/mm^2) for the 0.8wt% vanadium carbide UN alloys.

GRADE	HV(load)	ARC1	ARC2	800°C	900°C
N68	HV20	2108	2108	2108	2109
	+	0	0	40	43
	-	0	0	16	12
	HV30	2105	2105	2115	2102
	+	63	63	53	0
	-	27	27	13	0
	HV50	2108	2110	2110	2108
	+	40	38	38	40
	-	10	12	12	10
	Ave. HV	2107	2107	2111	2106
	+	1	3	4	3
	-	2	3	3	4
N88	HV20	1994	1994	1994	1994
	+	36	36	36	36
	-	37	37	37	37
	HV30	1998	1993	1998	1998
	+	41	46	41	41
	-	20	15	20	20
	HV50	1992	1990	2001	1992
	+	9	11	0	9
	-	37	35	0	37
	Ave. HV	1995	1992	1998	1995
	+	4	1	3	4
	-	3	3	4	3
N108	HV20	1866	1866	1871	1888
	+	22	22	17	0
	-	44	44	49	0
	HV30	1865	1865	1865	1865
	+	0	0	0	0
	-	0	0	0	0
	HV50	1868	1868	1868	1868
	+	0	0	0	0
	-	0	0	0	0
	Ave. HV	1866	1866	1868	1874
	+	2	2	3	14
	-	1	1	3	9
N158	HV20	1609	1612	1618	1612
	+	35	32	26	32
	-	18	21	27	21
	HV30	1613	1614	1613	1613
	+	9	8	9	9
	-	34	35	34	34
	HV50	1610	1612	1606	1614
	+	30	28	0	26
	-	4	6	0	8
	Ave. HV	1611	1613	1612	1613
	+	3	2	5	1
	-	2	1	6	1

Table A5: Vickers hardness(kg/mm^2) for the 0.4wt% vanadium carbide US alloys.

GRADE	HV(load)	ARC1	ARC2	800°C	900°C
S64	HV20	1880	1888	1888	1888
	+	8	0	0	0
	-	58	0	0	0
	HV30	1884	1887	1884	1887
	+	36	33	36	33
	-	19	22	19	22
	HV50	1883	1879	1883	1886
	+	28	32	28	25
	-	15	52	15	18
	Ave. HV	1882	1885	1885	1887
	+	1	3	3	1
	-	2	5	2	1
S84	HV20	1822	1822	1822	1823
	+	0	0	0	0
	-	0	0	0	0
	HV30	1823	1825	1825	1823
	+	42	40	40	42
	-	11	13	13	11
	HV50	1827	1827	1827	1827
	+	0	0	0	0
	-	0	0	0	0
	Ave. HV	1824	1825	1825	1824
	+	3	2	2	3
	-	2	3	3	1
S104	HV20	1710	1716	1715	1720
	+	50	44	45	40
	-	66	72	14	19
	HV30	1713	1713	1714	1713
	+	0	0	48	0
	-	0	0	48	0
	HV50	1712	1711	1711	1711
	+	37	0	0	0
	-	37	0	0	0
	Ave. HV	1711	1713	1713	1715
	+	1	3	2	6
	-	2	2	2	4
S154	HV20	1492	1492	1492	1492
	+	0	0	0	0
	-	0	0	0	0
	HV30	1493	1498	1498	1498
	+	0	0	0	0
	-	0	0	0	0
	HV50	1498	1495	1495	1490
	+	0	15	15	20
	-	0	15	15	10
	Ave. HV	1494	1495	1495	1493
	+	4	3	3	5
	-	3	3	3	3

Table A6: Vickers hardness(kg/mm²) for the 0.8wt% vanadium carbide US alloys.

GRADE	HV(load)	ARC1	ARC2	800°C	900°C
S68	HV20	2148	2148	2148	2148
	+	41	41	41	41
	-	40	40	40	40
	HV30	2135	2168	2168	2168
	+	33	0	0	0
	-	33	0	0	0
	HV50	2149	2149	2149	2149
	+	52	52	52	52
	-	51	51	51	51
	Ave. HV	2144	2155	2155	2155
	+	5	13	13	13
	-	9	7	7	7
S88	HV20	2030	2030	2030	2031
	+	0	0	0	77
	-	0	0	0	74
	HV30	2032	2029	2039	2039
	+	70	10	0	0
	-	54	51	0	0
	HV50	2037	2037	2025	2033
	+	11	61	23	15
	-	36	36	24	32
	Ave. HV	2033	2032	2031	2034
	+	4	5	7	4
	-	3	3	6	3
S108	HV20	1888	1888	1888	1888
	+	0	0	0	0
	-	0	0	0	0
	HV30	1890	1893	1887	1884
	+	30	27	33	36
	-	78	28	22	19
	HV50	1883	1890	1886	1890
	+	28	21	25	21
	-	15	22	18	22
	Ave. HV	1887	1890	1887	1887
	+	3	3	1	3
	-	4	2	1	3
S158	HV20	1652	1656	1658	1656
	+	49	45	43	45
	-	8	12	14	12
	HV30	1650	1656	1656	1655
	+	63	57	57	11
	-	28	34	34	33
	HV50	1657	1652	1652	1657
	+	18	23	23	18
	-	17	12	12	17
	Ave. HV	1653	1654	1655	1656
	+	4	1	3	1
	-	3	3	4	1

APPENDIX B

TUNGSTEN CARBIDE GRAIN SIZE in μm

This appendix lists the data table for the tungsten carbide grain size of each ultrafine hard metal grade determined using equations B1, B2, B3 and B4.

Porat & Malek(P&M)[131]:

$$d_{WC} = 0.3\left(\frac{80}{K}\right)^{0.57(1/V_{Co})^{1/3}} \quad \text{...(B1)}$$

Fang & Eason(F&E)[120]:

$$d_{WC} = 73\left(1 - 1.03\exp\left[-5V_{Co}\right]\right)\left(\frac{1-V_{Co}}{KV_{Co}}\right) \quad \text{...(B2)}$$

Roebuck[133]:

$$d_{WC} = \frac{7.93}{K - 6.71} \quad \text{for } K > 12.5\text{kAm}^{-1} \quad \text{...(B3)}$$

$$d_{WC} = \frac{10.9}{K - 1.79} \quad \text{for } K < 12.5\text{kAm}^{-1} \quad \text{...(B4)}$$

Table B1: *Tungsten carbide grain size(μm) determination using theoretical equations.*

Grade	P&M	F&E	Roebuck	*Grade*	P&M	F&E	Roebuck
D64	0.52	0.33	0.14	*D68*	0.48	0.32	0.14
D84	0.88	0.43	0.21	*D88*	0.72	0.38	0.18
D104	0.95	0.44	0.24	*D108*	0.75	0.37	0.20
D154	1.67	0.58	0.47	*D158*	1.00	0.40	0.29
N64	0.87	0.44	0.20	*N68*	0.66	0.38	0.16
N84	1.35	0.56	0.29	*N88*	0.63	0.35	0.17
N104	1.37	0.55	0.33	*N108*	0.78	0.38	0.20
N154	1.46	0.52	0.41	*N158*	1.22	0.46	0.34
S64	0.97	0.47	0.21	*S68*	0.66	0.38	0.16
S84	1.40	0.58	0.30	*S88*	0.78	0.40	0.20
S104	2.10	0.73	0.47	*S108*	0.80	0.39	0.21
S154	2.06	0.68	0.60	*S158*	1.15	0.44	0.33

APPENDIX C

PALMQVIST CRACK LENGTHS in μm

This appendix lists the data tables for the average total Palmqvist crack lengths for each ultrafine hard metal grade with respect to indenting load and heat treated condition. The total crack length is defined as the sum of the four crack lengths emanating from the four corners of a single hardness indent. The data shown in the tables represent the average of at least thirty indents made per load for each grade. The symbols used in the tables are defined as:

LOAD(N) ⇒ indenting load used
ARC1 ⇒ as-received condition polished with 9μm diamond grit
ARC2 ⇒ as-received condition polished with 0.25μm diamond grit
800°C ⇒ 800°C annealed condition
900°C ⇒ 900°C annealed condition
AVE. ⇒ average total crack length per load
\+ ⇒ positive deviation from the average value
\- ⇒ negative deviation from the average value

Table C1: Average total Palmqvist crack lengths in μm for the UD4 grades.

Grade	Load(N)	ARC1	ARC2	800°C	900°C	AVE.
D64	196	391	403	390	403	397
	+	24	28	14	23	6
	-	10	15	16	32	7
	294	576	508	600	590	569
	+	49	35	28	28	32
	-	31	25	25	52	61
	491	977	978	990	970	979
	+	23	28	16	46	11
	-	22	22	17	42	9
D84	196	334	332	321	340	332
	+	30	36	54	35	8
	-	37	33	21	30	11
	294	495	491	507	512	501
	+	23	14	18	31	11
	-	20	13	42	36	10
	491	833	839	819	800	823
	+	37	22	31	32	16
	-	32	37	30	26	23
D104	196	302	287	310	311	303
	+	24	43	40	29	9
	-	27	27	20	26	16
	294	440	436	437	430	436
	+	10	34	13	25	4
	-	30	31	21	16	6
	491	675	759	670	681	696
	+	20	25	20	39	63
	-	25	40	23	36	26
D154	196	212	207	196	195	203
	+	23	34	32	31	10
	-	12	36	32	32	8
	294	315	327	319	305	317
	+	20	28	18	42	11
	-	20	36	32	17	12
	491	541	543	525	545	539
	+	14	27	37	46	7
	-	16	52	38	38	14

Table C2: Average total Palmqvist crack lengths in μm for the UD8 grades.

Grade	Load(N)	ARC1	ARC2	800°C	900°C	AVE.
D68	196	452	447	440	459	450
	+	20	34	47	30	10
	-	31	41	39	61	10
	294	646	647	652	645	648
	+	14	30	39	46	5
	-	16	49	43	26	3
	491	944	1007	988	978	979
	+	11	41	33	38	28
	-	20	22	35	47	35
D88	196	384	390	381	384	385
	+	21	37	29	51	5
	-	14	24	26	59	4
	294	551	549	546	556	551
	+	24	36	44	44	6
	-	41	34	55	41	5
	491	792	888	840	880	850
	+	43	38	43	36	38
	-	50	30	31	37	58
D108	196	318	316	322	318	319
	+	32	20	28	50	4
	-	30	35	30	35	3
	294	473	465	475	471	471
	+	12	17	24	30	4
	-	46	28	41	28	6
	491	790	801	790	797	795
	+	36	40	29	34	7
	-	75	25	34	34	5
D158	196	200	191	196	194	195
	+	27	39	45	41	5
	-	27	36	41	39	4
	294	316	319	331	332	325
	+	44	39	36	43	8
	-	51	39	36	27	9
	491	522	484	515	555	519
	+	21	52	41	36	36
	-	26	41	28	43	35

Table C3: Average total Palmqvist crack lengths in μm for the UN4 grades.

Grade	Load(N)	ARC1	ARC2	800°C	900°C	AVE.
N64	196	349	357	340	361	352
	+	11	23	50	54	9
	-	24	47	35	57	12
	294	518	523	525	530	524
	+	37	48	37	29	6
	-	43	38	47	32	6
	491	873	872	872	876	873
	+	39	53	23	31	3
	-	48	37	37	54	1
N84	196	301	296	290	300	297
	+	56	36	56	38	4
	-	39	35	49	39	7
	294	443	458	460	460	455
	+	48	33	36	23	5
	-	37	45	43	49	-3
	491	747	749	762	765	756
	+	35	43	30	26	9
	-	49	46	39	58	9
N104	196	255	259	262	267	261
	+	42	36	48	53	6
	-	54	42	32	57	6
	294	393	388	388	390	390
	+	39	59	28	45	3
	-	46	42	28	45	2
	491	647	650	653	648	650
	+	29	35	23	38	4
	-	25	35	23	38	3
N154	196	182	188	183	181	184
	+	23	44	51	29	5
	-	42	40	58	41	3
	294	274	277	270	278	275
	+	33	35	35	43	3
	-	48	64	45	41	5
	491	458	458	466	467	462
	+	32	33	42	38	5
	-	38	43	44	48	4

Table C4: Average total Palmqvist crack lengths in μm for the UN8 grades.

Grade	Load(N)	ARC1	ARC2	800°C	900°C	AVE.
N68	196	392	394	395	403	396
	+	63	71	32	29	7
	-	72	30	28	21	4
	294	583	592	610	593	595
	+	52	41	35	34	16
	-	38	26	47	22	12
	491	989	1005	978	988	990
	+	51	40	32	40	15
	-	39	50	23	30	12
N88	196	335	338	336	333	336
	+	46	32	43	36	3
	-	43	47	36	33	3
	294	505	502	509	505	505
	+	36	559	32	57	4
	-	43	44	37	27	3
	491	830	835	852	844	840
	+	41	37	45	48	12
	-	49	46	50	52	10
N108	196	299	300	297	297	298
	+	66	45	33	23	2
	-	44	40	37	42	1
	294	451	450	448	444	448
	+	44	48	25	11	3
	-	51	43	35	29	4
	491	745	742	745	745	744
	+	25	38	17	25	1
	-	25	27	36	25	2
N158	196	226	220	225	223	224
	+	19	43	23	33	3
	-	26	25	15	26	4
	294	341	337	330	335	336
	+	49	48	15	35	5
	-	56	37	22	39	6
	491	560	563	555	545	556
	+	32	22	20	38	7
	-	30	13	36	40	11

Table C5: Average total Palmqvist crack lengths in μm for the US4 grades.

Grade	Load(N)	ARC1	ARC2	800°C	900°C	AVE.
S64	196	347	349	348	343	347
	+	13	47	37	41	2
	-	22	34	31	38	4
	294	524	520	526	520	523
	+	71	55	29	21	4
	-	59	30	38	27	3
	491	861	869	862	852	861
	+	48	26	29	29	8
	-	56	31	47	26	9
S84	196	310	308	308	308	309
	+	25	35	28	32	2
	-	13	22	17	19	1
	294	457	464	457	457	459
	+	21	21	14	21	5
	-	35	14	26	26	2
	491	779	779	779	770	777
	+	36	36	36	45	2
	-	49	49	49	40	7
S104	196	245	249	253	248	249
	+	54	11	10	16	4
	-	40	14	16	20	4
	294	373	373	380	374	375
	+	13	26	17	18	5
	-	23	12	14	16	2
	491	620	623	627	625	624
	+	20	13	24	18	3
	-	15	13	22	16	4
S154	196	166	165	168	167	167
	+	21	22	18	14	2
	-	30	29	25	30	2
	294	251	250	250	248	250
	+	20	23	27	21	1
	-	38	25	27	15	2
	491	415	415	415	418	416
	+	22	31	36	23	2
	-	17	23	29	21	1

Table C6: Average total Palmqvist crack lengths in μm for the US8 grades.

Grade	Load(N)	ARC1	ARC2	800°C	900°C	AVE.
S68	196	468	473	468	488	474
	+	42	26	48	43	14
	-	53	33	23	27	6
	294	695	725	700	740	715
	+	50	40	40	28	25
	-	30	40	27	28	20
	491	1176	1193	1155	1175	1175
	+	27	22	40	28	18
	-	45	43	40	36	20
S88	196	409	410	418	418	414
	+	41	25	17	45	4
	-	39	35	20	33	5
	294	622	605	627	613	617
	+	43	40	38	40	10
	-	32	20	47	45	12
	491	1019	1047	1032	1033	1033
	+	51	33	28	47	14
	-	44	47	32	33	14
S108	196	349	357	360	350	354
	+	26	48	35	35	6
	-	24	47	30	20	5
	294	529	525	522	528	526
	+	36	14	48	47	3
	-	24	10	17	28	4
	491	876	875	883	888	881
	+	59	24	15	18	8
	-	43	10	28	35	6
S158	196	249	248	248	253	250
	+	16	38	37	42	4
	-	29	33	38	18	2
	294	373	375	385	392	381
	+	29	10	35	18	11
	-	38	16	30	37	8
	491	633	620	623	652	632
	+	38	24	42	48	20
	-	23	19	43	48	12

APPENDIX D

PALMQVIST FRACTURE TOUGHNESS in $MNm^{-3/2}$

This appendix lists the data tables for the Palmqvist fracture toughness of each ultrafine hard metal grade with respect to indenting load and heat treated condition. The Palmqvist fracture toughness was calculated using equation D1 that was developed by Shetty *et al*[6].

$$K_{IC} = 0.0889\sqrt{\frac{H.P}{Li}} \qquad \text{...(D1)}$$

where: $H \Rightarrow$ Vickers hardness (Nm^{-2})
$P \Rightarrow$ Indent load (N)
$L_i \Rightarrow$ Total crack length (m)

The symbols used in the tables are defined as:

Load(N) ⇒ indenting load used
ARC1 ⇒ as-received condition polished with 9μm diamond grit
ARC2 ⇒ as-received condition polished with 0.25μm diamond grit
800°C ⇒ 800°C annealed condition
900°C ⇒ 900°C annealed condition
AVE1 ⇒ average toughness per load
AVE2 ⇒ average toughness per condition
\+ ⇒ positive deviation from the average value
\- ⇒ negative deviation from the average value

Table D1: Palmqvist fracture toughness in $MNm^{-3/2}$ for the UD4 grades.

GRADE	LOAD (N)	ARC1	ARC2	800°C	900°C	AVE1
D64	196	8.87	8.71	8.87	8.75	8.80
	+	0.12	0.11	0.44	0.3	0.07
	-	0.24	0.3	0.4	0.04	0.09
	294	8.96	9.53	8.75	8.81	9.01
	+	0.36	0.21	0.04	0.5	0.52
	-	0.25	0.21	0.03	0.27	0.26
	491	8.88	8.88	8.86	8.91	8.88
	+	0.14	0.38	0.2	0.27	0.03
	-	0.19	0.38	0.09	0.27	0.02
	AVE2	8.90	9.04	8.83	8.82	8.90
	+	0.06	0.49	0.04	0.09	0.14
	-	0.03	0.33	0.08	0.07	0.07
D84	196	9.35	9.44	9.54	9.27	9.40
	+	0.21	0.3	0.33	0.44	0.14
	-	0.31	0.27	0.4	0.44	0.13
	294	9.36	9.35	9.38	9.33	9.36
	+	0.19	0.27	0.42	0.4	0.03
	-	0.04	0.34	0.29	0.41	0.03
	491	9.31	9.26	9.23	9.31	9.28
	+	0.72	0.32	0.91	0.42	0.03
	-	0.2	0.25	0.3	0.37	0.05
	AVE2	9.34	9.35	9.38	9.294	9.34
	+	0.02	0.09	0.16	0.03	0.04
	-	0.03	0.09	0.15	0.03	0.04
D104	196	9.53	9.75	9.38	9.37	9.51
	+	0.69	0.47	0.32	0.41	0.24
	-	0.31	0.44	0.25	0.42	0.14
	294	9.31	9.56	9.78	9.85	9.63
	+	0.38	0.35	0.12	0.22	0.23
	-	0.21	0.36	0.5	0.23	0.32
	491	10.01	9.56	10.07	9.98	9.91
	+	0.32	0.47	0.15	0.28	0.16
	-	0.13	0.41	0.15	0.27	0.35
	AVE2	9.62	9.62	9.74	9.73	9.68
	+	0.39	0.13	0.33	0.25	0.06
	-	0.31	0.06	0.36	0.36	0.06
D154	196	10.58	10.73	11.03	11.06	10.85
	+	0.34	0.19	0.38	0.21	0.21
	-	0.5	0.2	0.22	0.19	0.27
	294	10.63	10.45	10.63	10.82	10.63
	+	0.37	0.43	0.14	0.21	0.19
	-	0.44	0.42	0.15	0.24	0.18
	491	10.5	10.45	10.46	10.16	10.39
	+	0.17	0.49	0.17	0.22	0.11
	-	0.22	0.12	0.25	0.23	0.23
	AVE2	10.57	10.54	10.71	10.68	10.63
	+	0.06	0.19	0.32	0.38	0.08
	-	0.07	0.09	0.25	0.52	0.08

Table D2: Palmqvist fracture toughness in $MNm^{-3/2}$ for the UD8 grades.

GRADE	LOAD (N)	ARC1	ARC2	800°C	900°C	AVE1
D68	196	8.66	8.71	8.78	8.54	8.67
	+	0.02	0.44	0.21	0.19	0.11
	-	0.05	0.4	0.25	0.25	0.13
	294	8.83	8.82	8.84	8.84	8.83
	+	0.11	0.22	0.17	0.44	0.01
	-	0.09	0.19	0.17	0.45	0.01
	491	9.44	8.44	9.08	9.12	9.02
	+	0.02	0.34	0.1	0.44	0.42
	-	0.02	0.4	0.2	0.43	0.58
	AVE2	8.98	8.66	8.90	8.83	8.84
	+	0.46	0.16	0.18	0.29	0.14
	-	0.32	0.22	0.12	0.29	0.19
D88	196	9.05	8.98	9.09	9.05	9.04
	+	0.17	0.2	0.32	0.29	0.05
	-	0.24	0.25	0.33	0.37	0.06
	294	9.25	9.29	9.32	9.23	9.27
	+	0.39	0.33	0.41	0.38	0.05
	-	0.44	0.33	0.35	0.4	0.04
	491	9.96	9.44	9.5	9.29	9.55
	+	0.22	0.32	0.31	0.3	0.41
	-	0.77	0.42	0.22	0.28	0.26
	AVE2	9.42	9.24	9.294	9.19	9.29
	+	0.54	0.196	0.196	0.10	0.13
	-	0.37	0.26	0.21	0.14	0.10
D108	196	9.65	9.68	9.58	9.63	9.64
	+	0.19	0.19	0.16	0.18	0.04
	-	0.38	0.32	0.27	0.11	0.05
	294	9.68	9.79	9.64	9.7	9.70
	+	0.46	0.2	0.23	0.21	0.09
	-	0.45	0.31	0.32	0.24	0.06
	491	9.69	9.62	9.69	9.64	9.66
	+	0.61	0.21	0.27	0.27	0.03
	-	0.11	0.4	0.27	0.31	0.04
	AVE2	9.67	9.70	9.64	9.66	9.67
	+	0.02	0.09	0.05	0.04	0.03
	-	0.02	0.08	0.06	0.03	0.03
D158	196	10.7	11.07	11.21	11.46	11.11
	+	0.19	0.24	0.4	0.36	0.35
	-	0.25	0.34	0.47	0.39	0.41
	294	10.54	10.5	10.76	10.79	10.65
	+	0.27	0.3	0.54	0.48	0.14
	-	0.58	0.34	0.47	0.48	0.15
	491	10.58	10.97	11	10.71	10.82
	+	0.43	0.25	0.31	0.33	0.19
	-	0.12	0.46	0.28	0.18	0.23
	AVE2	10.61	10.85	10.99	10.99	10.86
	+	0.09	0.22	0.22	0.47	0.13
	-	0.07	0.35	0.23	0.28	0.25

Table D3: Palmqvist fracture toughness in $MNm^{-3/2}$ for the UN4 grades.

GRADE	LOAD (N)	ARC1	ARC2	800°C	900°C	AVE1
N64	196	9.25	9.2	9.31	9.17	9.23
	+	0.26	0.49	0.46	0.44	0.08
	-	0.53	0.48	0.5	0.28	0.06
	294	9.3	9.19	9.28	9.18	9.24
	+	0.38	0.32	0.5	0.36	0.06
	-	0.33	0.64	0.41	0.37	0.06
	491	9.25	9.25	9.26	9.26	9.26
	+	0.75	0.28	0.27	0.27	0.01
	-	0.41	0.3	0.21	0.39	0.01
	AVE2	9.27	9.21	9.29	9.196	9.24
	+	0.04	0.04	0.03	0.06	0.05
	-	0.02	0.03	0.02	0.03	0.04
N84	196	9.73	9.77	9.86	9.7	9.77
	+	0.4	0.43	0.23	0.36	0.09
	-	0.48	0.42	0.23	0.38	0.07
	294	9.76	9.71	9.7	9.71	9.72
	+	0.63	0.6	0.35	0.18	0.04
	-	0.88	0.34	0.33	0.28	0.02
	491	9.76	9.78	9.79	9.63	9.74
	+	0.79	0.56	0.32	0.28	0.05
	-	0.59	0.42	0.42	0.41	0.11
	AVE2	9.75	9.75	9.78	9.68	9.74
	+	0.01	0.02	0.08	0.03	0.04
	-	0.02	0.04	0.09	0.05	0.06
N104	196	10.24	10.2	10.16	10.14	10.19
	+	0.47	0.47	0.45	0.47	0.06
	-	0.46	0.47	0.28	0.26	0.04
	294	10.15	10.2	10.25	10.18	10.196
	+	0.46	0.38	0.31	0.38	0.05
	-	0.3	0.34	0.41	0.34	0.04
	491	10.18	10.17	10.15	10.16	10.17
	+	0.3	0.2	0.37	0.36	0.02
	-	0.52	0.31	0.34	0.35	0.01
	AVE2	10.19	10.19	10.19	10.16	10.18
	+	0.05	0.01	0.07	0.02	0.01
	-	0.04	0.02	0.04	0.02	0.02
N154	196	11.39	11.26	11.25	11.36	11.32
	+	0.29	0.2	0.36	0.49	0.08
	-	0.47	0.25	0.27	0.3	0.06
	294	11.39	11.35	11.4	11.4	11.39
	+	0.22	0.16	0.43	0.41	0.02
	-	0.34	0.36	0.23	0.48	0.04
	491	11.36	11.37	11.29	11.31	11.33
	+	0.33	0.32	0.29	0.44	-0.04
	-	0.31	0.32	0.36	0.32	0.04
	AVE2	11.38	11.32	11.31	11.36	11.34
	+	0.01	0.04	0.09	0.04	0.04
	-	0.02	0.07	0.07	0.05	0.03

Table D4: Palmqvist fracture toughness in $MNm^{-3/2}$ for the UN8 grades.

GRADE	LOAD (N)	ARC1	ARC2	800°C	900°C	AVE1
N68	196	9.13	9.13	9.09	9.00	9.09
	+	0.48	0.35	0.24	0.32	0.04
	-	0.59	0.51	0.2	0.12	0.09
	294	9.11	9.08	9.03	9.08	9.08
	+	0.36	0.2	0.38	0.19	0.04
	-	0.49	0.29	0.33	0.21	0.04
	491	9.1	9.04	9.12	9.07	9.08
	+	0.69	0.19	0.1	0.36	0.04
	-	0.75	0.35	0.14	0.28	0.04
	AVE2	9.11	9.09	9.08	9.05	9.08
	+	0.02	0.05	0.04	0.03	0.03
	-	0.01	0.04	0.05	0.05	0.03
N88	196	9.57	9.57	9.61	9.6	9.59
	+	0.26	0.19	0.23	0.45	0.02
	-	0.29	0.2	0.25	0.46	0.02
	294	9.56	9.59	9.57	9.6	9.58
	+	0.24	0.27	0.32	0.2	0.02
	-	0.23	0.38	0.22	0.2	0.02
	491	9.61	9.65	9.55	9.62	9.61
	+	0.36	0.34	0.21	0.29	0.04
	-	0.33	0.22	0.34	0.36	0.06
	AVE2	9.58	9.60	9.58	9.60	9.59
	+	0.03	0.05	0.03	0.02	0.01
	-	0.02	0.04	0.03	0.01	0.01
N108	196	9.82	9.87	9.84	9.85	9.85
	+	0.59	0.25	0.3	0.22	0.03
	-	0.5	0.36	0.43	0.38	0.02
	294	9.81	9.84	9.87	9.84	9.84
	+	0.45	0.38	0.15	0.23	0.03
	-	0.65	0.22	0.11	0.17	0.03
	491	9.86	9.89	9.84	9.87	9.87
	+	0.43	0.18	0.15	0.16	0.03
	-	0.47	0.25	0.11	0.17	0.03
	AVE2	9.83	9.87	9.85	9.85	9.85
	+	0.03	0.02	0.02	0.02	0.02
	-	0.02	0.03	0.01	0.02	0.02
N158	196	10.51	10.59	10.55	10.61	10.57
	+	0.59	0.32	0.41	0.38	0.04
	-	0.52	0.39	0.42	0.22	0.06
	294	10.53	10.58	10.61	10.51	10.56
	+	0.52	0.3	0.33	0.32	0.05
	-	0.7	0.3	0.16	0.3	0.05
	491	10.56	10.56	10.58	10.68	10.60
	+	0.29	0.08	0.21	0.31	0.08
	-	0.11	0.13	0.17	0.57	0.04
	AVE2	10.53	10.58	10.58	10.60	10.57
	+	0.03	0.01	0.03	0.08	0.03
	-	0.02	0.02	0.03	0.09	0.04

Table D5: Palmqvist fracture toughness in $MNm^{-3/2}$ for the US4 grades.

GRADE	LOAD (N)	ARC1	ARC2	800°C	900°C	AVE1
S64	196	9.24	9.23	9.23	9.27	9.24
	+	0.55	0.25	0.48	0.52	0.03
	-	0.35	0.44	0.58	0.5	0.01
	294	9.23	9.24	9.28	9.26	9.25
	+	0.41	0.3	0.43	0.09	0.03
	-	0.57	0.43	0.45	0.08	0.02
	491	9.22	9.22	9.22	9.24	9.23
	+	0.55	0.2	0.45	0.05	0.01
	-	0.25	0.14	0.51	0.06	0.01
	AVE2	9.23	9.23	9.24	9.26	9.24
	+	0.01	0.01	0.04	0.01	0.02
	-	0.01	0.01	0.03	0.02	0.00
S84	196	9.54	9.66	9.58	9.57	9.59
	+	0.08	0.23	0.04	0.14	0.07
	-	0.07	0.19	0.04	0.12	0.05
	294	9.6	9.6	9.62	9.6	9.61
	+	0.07	0.07	0.05	0.07	0.01
	-	0.03	0.03	0.05	0.03	0.01
	491	9.55	9.52	9.55	9.58	9.55
	+	0.31	0.11	0.31	0.39	0.03
	-	0.22	0.19	0.22	0.25	0.03
	AVE2	9.56	9.59	9.58	9.58	9.58
	+	0.04	0.07	0.04	0.02	0.01
	-	0.02	0.08	0.03	0.01	0.00
S104	196	10.38	10.32	10.29	10.27	10.32
	+	0.33	0.31	0.19	0.28	0.06
	-	0.68	0.42	0.3	0.28	0.05
	294	10.33	10.28	10.31	10.29	10.294
	+	0.19	0.09	0.07	0.08	0.03
	-	0.16	0.05	0.08	0.12	0.02
	491	10.34	10.33	10.29	10.31	10.32
	+	0.02	0.1	0.02	0.04	0.02
	-	0.02	0.1	0.02	0.04	0.03
	AVE2	10.35	10.31	10.294	10.29	10.31
	+	0.03	0.02	0.01	0.02	0.04
	-	0.02	0.02	0.01	0.02	0.02
S154	196	11.8	11.85	11.79	11.84	11.82
	+	0.61	0.36	0.42	0.01	0.03
	-	0.47	0.36	0.3	0.01	0.03
	294	11.78	11.83	11.83	11.82	11.82
	+	0.11	0.09	0.09	0.1	0.02
	-	0.1	0.06	0.06	0.05	0.04
	491	11.85	11.81	11.81	11.77	11.81
	+	0.29	0.1	0.1	0.11	0.04
	-	0.36	0.12	0.12	0.08	0.04
	AVE2	11.81	11.82	11.81	11.81	11.81
	+	0.04	0.03	0.02	0.03	0.01
	-	0.03	0.01	0.02	0.04	0.00

Table D6: Palmqvist fracture toughness in $MNm^{-3/2}$ for the US8 grades.

GRADE	LOAD (N)	ARC1	ARC2	800°C	900°C	AVE1
S68	196	8.42	8.41	8.47	8.35	8.41
	+	0.63	0.3	0.29	0.41	0.06
	-	0.53	0.38	0.45	0.43	0.06
	294	8.46	8.35	8.51	8.46	8.45
	+	0.34	0.23	0.48	0.55	0.06
	-	0.47	0.24	0.44	0.42	0.10
	491	8.43	8.4	8.35	8.47	8.41
	+	0.5	0.11	0.48	0.34	0.06
	-	0.82	0.12	0.36	0.48	0.06
	AVE2	8.44	8.38	8.44	8.43	8.42
	+	0.02	0.02	0.07	0.04	0.02
	-	0.01	0.04	0.10	0.08	0.04
S88	196	8.76	8.74	8.73	8.71	8.74
	+	0.48	0.37	0.35	0.33	0.03
	-	0.26	0.44	0.23	0.38	0.02
	294	8.69	8.77	8.71	8.69	8.72
	+	0.12	0.38	0.21	0.43	0.05
	-	0.25	0.47	0.27	0.31	0.03
	491	8.82	8.65	8.73	8.74	8.74
	+	0.4	0.16	0.19	0.38	0.09
	-	0.3	0.17	0.15	0.26	0.08
	AVE2	8.76	8.72	8.72	8.71	8.73
	+	0.07	0.05	0.01	0.03	0.03
	-	0.07	0.07	0.01	0.02	0.01
S108	196	9.17	9.1	9.04	9.16	9.12
	+	0.32	0.21	0.37	0.25	0.05
	-	0.34	0.2	0.25	0.44	0.08
	294	9.11	9.12	9.17	9.11	9.13
	+	0.31	0.19	0.23	0.2	0.04
	-	0.44	0.14	0.24	0.3	0.02
	491	9.13	9.13	9.1	9.11	9.12
	+	0.36	0.13	0.45	0.41	0.01
	-	0.54	0.21	0.45	0.32	0.02
	AVE2	9.14	9.12	9.10	9.13	9.12
	+	0.03	0.01	0.07	0.03	0.02
	-	0.03	0.01	0.06	0.02	0.02
S158	196	10.09	10.07	10.13	10.14	10.11
	+	0.59	0.24	0.4	0.34	0.03
	-	0.55	0.18	0.44	0.3	0.04
	294	10.11	10.09	10.05	10.13	10.10
	+	0.58	0.07	0.25	0.28	0.04
	-	0.41	0.06	0.26	0.25	0.04
	491	10.12	10.11	10.09	10.07	10.10
	+	0.2	0.32	0.34	0.21	0.02
	-	0.27	0.36	0.34	0.25	0.03
	AVE2	10.11	10.09	10.09	10.11	10.10
	+	0.01	0.02	0.04	0.03	0.01
	-	0.01	0.02	0.04	0.04	0.01